

GAS-KINETIC METHODS FOR 3-D INVISCID AND VISCOUS FLOW  
SOLUTIONS ON UNSTRUCTURED/HYBRID GRIDS

A THESIS SUBMITTED TO  
THE GRADUATE SCHOOL OF NATURAL AND APPLIED SCIENCES  
OF  
MIDDLE EAST TECHNICAL UNIVERSITY

BY

MURAT ILGAZ

IN PARTIAL FULFILLMENT OF THE REQUIREMENTS  
FOR  
THE DEGREE OF DOCTOR OF PHILOSOPHY  
IN  
AEROSPACE ENGINEERING

FEBRUARY 2007

Approval of the Graduate School of Natural and Applied Sciences.

---

Prof. Dr. Canan Özgen  
Director

I certify that this thesis satisfies all the requirements as a thesis for the degree of Doctor of Philosophy.

---

Prof. Dr. İsmail H. Tuncer  
Head of Department

This is to certify that we have read this thesis and that in our opinion it is fully adequate, in scope and quality, as a thesis for the degree of Doctor of Philosophy.

---

Prof. Dr. İsmail H. Tuncer  
Supervisor

Examining Committee Members

Prof. Dr. M. Cevdet Çelenligil (METU-AEE) \_\_\_\_\_

Prof. Dr. İsmail H. Tuncer (METU-AEE) \_\_\_\_\_

Prof. Dr. Yusuf Özyörük (METU-AEE) \_\_\_\_\_

Prof. Dr. Zafer Dursunkaya (METU-ME) \_\_\_\_\_

Dr. Mehmet Ali Ak (TÜBİTAK-SAGE) \_\_\_\_\_

**I hereby declare that all information in this document has been obtained and presented in accordance with academic rules and ethical conduct. I also declare that, as required by these rules and conduct, I have fully cited and referenced all material and results that are not original to this work.**

Name, Last Name : Murat Ilgaz

Signature :

# ABSTRACT

GAS-KINETIC METHODS FOR 3-D INVISCID AND VISCOUS FLOW  
SOLUTIONS ON UNSTRUCTURED/HYBRID GRIDS

Ilgaz, Murat

Ph.D., Department of Aerospace Engineering

Supervisor: Prof. Dr. İsmail H. Tuncer

February 2007, 149 pages

In this thesis, gas-kinetic methods for inviscid and viscous flow simulations are developed. Initially, the finite volume gas-kinetic methods are investigated for 1-D flows as a preliminary study and are discussed in detail from theoretical and numerical points of view. The preliminary results show that the gas-kinetic methods do not produce any unphysical flow phenomena. Especially the Gas-Kinetic BGK method, which takes into account the particle collisions, predicts compressible flows accurately. The Gas-Kinetic BGK method is then extended for the solution of 2-D and 3-D inviscid and viscous flows on unstructured/hybrid grids. The computations are performed in parallel. Various

inviscid and viscous test cases are considered and it is shown that the Gas-Kinetic BGK method predicts both inviscid and viscous flow fields accurately. The implementation of hybrid grids for viscous flows reduces the overall number of grid cells while enabling the resolution of boundary layers. The parallel computations significantly improve the computation time of the Gas-Kinetic BGK method which, in turn, enable the method for the computation of practical aerodynamic flow problems.

Keywords: Gas-kinetic methods, Gas-Kinetic BGK method, hybrid grids, parallel computing, inviscid and viscous flows.

# ÖZ

## DÜZENSİZ/HİBRİD ÇÖZÜM AĞLARI ÜZERİNDE 3-BOYUTLU VİSKOZİTESİZ VE VİSKOZ AKIŞ ÇÖZÜMLEMELERİ İÇİN GAZ-KİNETİK YÖNTEMLER

Ilgaz, Murat

Doktora, Havacılık ve Uzay Mühendisliği Bölümü

Tez Yöneticisi: Prof. Dr. İsmail H. Tuncer

Şubat 2007, 149 sayfa

Bu tezde, viskozitesiz ve viskoz akış benzetimleri için gaz-kinetik yöntemler geliştirilmiştir. Başlangıç olarak, 1-boyutlu akışlar için sonlu hacim gaz-kinetik yöntemler araştırılmış ve teorik ve nümerik açıdan detaylı tartışmalar yapılmıştır. Elde edilen ilk sonuçlar, gaz-kinetik yöntemlerin fiziksel olmayan hiçbir olay ortaya çıkarmadığını göstermiştir. Özellikle, parçacık çarpışmalarını göz önüne alan Gaz-Kinetik BGK yöntemi sıkıştırılabilir akışları doğru bir şekilde hesaplamıştır. Gaz-Kinetik BGK yöntemi daha sonra düzensiz/hibrid çözüm ağları üzerinde 2- ve 3-boyutlu viskozitesiz ve viskoz akış çözümleri için geli-

tirilmiştir. Çözümlenmeler paralel ortamda yapılmıştır. Çeşitli viskozitesiz ve viskoz test problemleri göz önüne alınmış ve Gaz-Kinetik BGK yönteminin hem viskozitesiz hem de viskoz akışları doğru bir şekilde hesapladığı gösterilmiştir. Viskoz akışlar için hibrid çözüm ağı kullanımı, toplam çözüm ağı sayısını düşürmekle birlikte sınır tabakanın çözümlenmesine olanak sağlamıştır. Paralel hesaplamalar ise Gaz-Kinetik BGK yönteminin çözümleme süresini önemli ölçüde geliştirmiş ve yöntemin pratik aerodinamik akış problemlerinin çözümünde kullanılabilmesine olanak sağlamıştır.

Anahtar Kelimeler: Gaz-kinetik yöntemler, Gaz-Kinetik BGK yöntemi, hibrid çözüm ağları, paralel hesaplama, viskozitesiz ve viskoz akışlar.

to

*my love Nebahat, newborn son Murathan*

and

*my family*



## ACKNOWLEDGMENTS

I would like to thank my supervisor Prof. Dr. İsmail H. TUNCER for his support and guidance throughout this study. This has been greatly appreciated. In addition, many people have been of great assistance in professional and personal sense throughout my education and profession. At the risk of offending some people, I will attempt to name some of them.

First of all, I want to thank my professors in the Department of Aerospace Engineering for their contribution throughout my education. My work environment in TÜBİTAK-SAGE has always been a source of inspiration, and special thanks goes to Levent YALÇIN, Osman BAŞOĞLU, Dr. Hediye ATİK, Emel MAHMUTYAZICIOĞLU, Koray DAYANÇ and Dr. Gökmen MAHMUTYAZICIOĞLU with whom the discussions I made have been very profitable. Many of my colleagues and friends have been of great help in particular Bekir NARİN, Dr. L. Oktay GÖNÇ, Dr. Mehmet Ali AK and Mustafa KAYA during several steps of the thesis study.

Finally, I am immensely indebted to my family for their endless support and encouragement. I should admit that considerable parts of this thesis would

not be able to complete without the emotional support, understanding and sacrifice of my wife, Nebahat. I hope this thesis would be a small reward for that.

This study is supported in part by TÜBİTAK-SAGE through project *SAM*.

# TABLE OF CONTENTS

ABSTRACT . . . . .	iv
ÖZ . . . . .	vi
DEDICATION . . . . .	viii
ACKNOWLEDGMENTS . . . . .	ix
TABLE OF CONTENTS . . . . .	xi
LIST OF TABLES . . . . .	xiv
LIST OF FIGURES . . . . .	xv
CHAPTER	
1 INTRODUCTION . . . . .	1
1.1 Overview of Numerical Methods . . . . .	2
1.1.1 Methods Based on Continuum Approach . . . . .	2
1.1.1.1 Spatial Discretization and Flux Evaluations . . . . .	4
1.1.2 Methods Based on Gas-Kinetic Theory . . . . .	7
1.1.3 Parallel Computing . . . . .	10
1.1.4 Hybrid Grids . . . . .	10
1.2 Objective of the Thesis . . . . .	12
2 GOVERNING EQUATIONS OF FLUID FLOW AND GAS-KINETIC THEORY . . . . .	13
2.1 Continuum Fluid Flow and Governing Equations . . . . .	14
2.1.1 The Conservation of Mass . . . . .	15
2.1.2 The Conservation of Momentum . . . . .	15
2.1.3 The Conservation of Energy . . . . .	16

	2.1.4	The Equation of State . . . . .	17
	2.1.5	Summary . . . . .	18
2.2		Gas-Kinetic Theory . . . . .	19
	2.2.1	The Gas Distribution Function and Its Moments	20
	2.2.2	The Boltzmann Equation . . . . .	21
2.3		Connection Between Two Descriptions of Fluid Flow . .	24
3		NUMERICAL METHOD . . . . .	29
3.1		Preliminary Study on Gas-Kinetic Methods in 1-D . . .	30
	3.1.1	The Finite Volume Gas-Kinetic Methods . . . . .	30
	3.1.2	Roe's Flux Difference Splitting Scheme in 1-D .	32
		3.1.2.1 The First Order Formulation . . . . .	32
		3.1.2.2 Physical and Numerical Analysis .	33
	3.1.3	The Kinetic Flux Vector Splitting Scheme in 1-D	34
		3.1.3.1 The First Order Formulation . . . . .	35
		3.1.3.2 The Second Order Formulation . .	37
		3.1.3.3 Physical and Numerical Analysis .	39
	3.1.4	The Gas-Kinetic BGK Scheme in 1-D . . . . .	41
		3.1.4.1 The First Order Formulation . . . . .	42
		3.1.4.2 The Second Order Formulation . .	45
		3.1.4.3 Physical and Numerical Analysis .	48
3.2		Numerical Methodology in 2-D and 3-D . . . . .	50
	3.2.1	Spatial Discretization . . . . .	51
		3.2.1.1 The Gas-Kinetic BGK Scheme in 2-D	53
		3.2.1.2 The Gas-Kinetic BGK Scheme in 3-D	60
		3.2.1.3 Inviscid and Viscous Solutions From the Gas-Kinetic BGK Scheme . . . . .	67
	3.2.2	Temporal Discretization . . . . .	70
		3.2.2.1 Explicit Three-Stage Runge-Kutta Time- Stepping Scheme . . . . .	70
3.3		Boundary Conditions . . . . .	71
	3.3.1	Wall Boundary Condition . . . . .	71
	3.3.2	Farfield Boundary Condition . . . . .	72
	3.3.3	Symmetry Boundary Condition . . . . .	73

3.4	Parallel Processing Methodology . . . . .	73
4	RESULTS AND DISCUSSION . . . . .	75
4.1	1-D Shock-Tube Problems . . . . .	75
4.1.1	Case 1: Sod Shock-Tube Problem . . . . .	76
4.1.2	Case 2: Arora-Roe Shock-Tube Problem . . . . .	80
4.1.3	Case 3: Woodward-Colella Shock-Tube Problem . . . . .	84
4.1.4	Summary . . . . .	88
4.2	2-D Flows . . . . .	89
4.2.1	Case 1: Inviscid Flow Over a Transonic Airfoil . . . . .	89
4.2.2	Case 2: Inviscid Supersonic Flow Over a Wedge . . . . .	99
4.2.3	Case 3: Inviscid High-Speed Flow Over a Blunt Body . . . . .	101
4.2.4	Case 4: Laminar Flow Over a Flat Plate . . . . .	104
4.2.5	Case 5: Laminar Flow Over a Transonic Airfoil . . . . .	107
4.2.6	Summary . . . . .	111
4.3	3-D Flows . . . . .	112
4.3.1	Case 1: Inviscid Subsonic Flow Over a Missile . . . . .	112
4.3.2	Case 2: Inviscid Transonic Flow Over a Wing . . . . .	115
4.3.3	Case 3: Inviscid Supersonic Flow Over a Missile . . . . .	120
4.3.4	Case 4: Laminar Flow Over a Flat Plate . . . . .	124
4.3.5	Summary . . . . .	131
5	CONCLUDING REMARKS . . . . .	132
	REFERENCES . . . . .	136
	APPENDICES . . . . .	144
	A MOMENTS OF THE GAS DISTRIBUTION FUNCTION . . . . .	144
	VITA . . . . .	147

## LIST OF TABLES

### TABLES

Table 4.1	Initial conditions for Case 1. . . . .	76
Table 4.2	Initial conditions for Case 2. . . . .	80
Table 4.3	Initial conditions for Case 3. . . . .	84
Table 4.4	Freestream conditions for Case 1. . . . .	89
Table 4.5	Parallel efficiency of computations. . . . .	97
Table 4.6	Freestream conditions for Case 2. . . . .	99
Table 4.7	Freestream conditions for Case 3. . . . .	102
Table 4.8	Freestream conditions for Case 4. . . . .	104
Table 4.9	Freestream conditions for Case 5. . . . .	107
Table 4.10	Freestream conditions for Case 1. . . . .	112
Table 4.11	Freestream conditions for Case 2. . . . .	115
Table 4.12	Freestream conditions for Case 3. . . . .	120
Table 4.13	Freestream conditions for Case 4. . . . .	124

## LIST OF FIGURES

### FIGURES

Figure 3.1 Constant initial gas distribution function for the first order KFVS scheme. . . . .	36
Figure 3.2 Linearly varying initial gas distribution function for the second order KFVS scheme. . . . .	38
Figure 3.3 Constant initial gas distribution function and the equilibrium state for the first order Gas-Kinetic BGK scheme. . . . .	43
Figure 3.4 Linearly varying initial gas distribution function and the equilibrium state for the second order Gas-Kinetic BGK scheme. . .	46
Figure 3.5 Elements of unstructured grids in 2-D and 3-D. . . . .	51
Figure 3.6 Elements of hybrid grids in 2-D and 3-D. . . . .	52
Figure 3.7 Sample triangular control volumes, cell interface and coordinate systems. . . . .	54
Figure 3.8 Reconstruction procedure in an arbitrary triangular cell. . .	56
Figure 3.9 Sample tetrahedron control volumes, cell interface and coordinate systems. . . . .	61
Figure 3.10 Sample hybrid grid in 2-D and the corresponding graph. . .	73
Figure 4.1 Density distribution for Case 1 (First order results). . . . .	76
Figure 4.2 Mach number distribution for Case 1 (First order results). . .	77
Figure 4.3 Pressure distribution for Case 1 (First order results). . . . .	77
Figure 4.4 Density distribution for Case 1 (Second order results). . . . .	78
Figure 4.5 Mach number distribution for Case 1 (Second order results). . .	79
Figure 4.6 Pressure distribution for Case 1 (Second order results). . . .	79
Figure 4.7 Density distribution for Case 2 (First order results). . . . .	81
Figure 4.8 Mach number distribution for Case 2 (First order results). . .	81
Figure 4.9 Pressure distribution for Case 2 (First order results). . . . .	82
Figure 4.10 Density distribution for Case 2 (Second order results). . . . .	83
Figure 4.11 Mach number distribution for Case 2 (Second order results). .	83

Figure 4.12	Pressure distribution for Case 2 (Second order results).	84
Figure 4.13	Density distribution for Case 3 (First order results).	85
Figure 4.14	Mach number distribution for Case 3 (First order results).	85
Figure 4.15	Pressure distribution for Case 3 (First order results).	86
Figure 4.16	Density distribution for Case 3 (Second order results).	87
Figure 4.17	Mach number distribution for Case 3 (Second order results).	87
Figure 4.18	Pressure distribution for Case 3 (Second order results).	88
Figure 4.19	Computational mesh with partitions for Case 1 (Zoomed view).	90
Figure 4.20	Mach number contours for Case 1 (Kinetic FVS scheme).	91
Figure 4.21	Mach number contours for Case 1 (Gas-Kinetic BGK scheme).	91
Figure 4.22	Mach number contours for Case 1 (Roe's FDS scheme).	92
Figure 4.23	Entropy contours for Case 1 (Kinetic FVS scheme).	92
Figure 4.24	Entropy contours for Case 1 (Gas-Kinetic BGK scheme).	93
Figure 4.25	Entropy contours for Case 1 (Roe's FDS scheme).	93
Figure 4.26	Pressure distribution on the airfoil surface for Case 1 (Kinetic FVS scheme, every other three data point is displayed).	94
Figure 4.27	Pressure distribution on the airfoil surface for Case 1 (Gas-Kinetic BGK scheme, every other three data point is displayed).	95
Figure 4.28	Pressure distribution on the airfoil surface for Case 1 (Roe's FDS scheme, every other three data point is displayed).	95
Figure 4.29	Entropy contours over RAE 2822 airfoil at $M = 0.3$ .	96
Figure 4.30	Computational speed-up for Case 1.	97
Figure 4.31	Convergence history for Case 1.	98
Figure 4.32	Computational mesh with partitions for Case 2.	99
Figure 4.33	Mach number contours for Case 2.	100
Figure 4.34	Pressure contours for Case 2.	100
Figure 4.35	Pressure contours taken from [64].	100
Figure 4.36	Nondimensional pressure distribution along the lower wall of the channel for Case 2.	101
Figure 4.37	Computational mesh with partitions for Case 3.	102
Figure 4.38	Density contours for Case 3 (Gas-Kinetic BGK scheme, zoomed view).	103
Figure 4.39	Density contours for Case 3 (Roe's FDS scheme, zoomed view).	103
Figure 4.40	Computational mesh with partitions for Case 4 (Zoomed view).	105
Figure 4.41	Mach number contours and velocity vectors for Case 4 (Zoomed view).	105
Figure 4.42	u-velocity profile in the boundary layer for Case 4.	106



Figure 4.43	v-velocity profile in the boundary layer for Case 4. . . . .	106
Figure 4.44	Computational mesh with partitions for Case 5 (Zoomed view). . . . .	108
Figure 4.45	Mach number contours for Case 5. . . . .	108
Figure 4.46	Streamlines and the separation on the suction side for Case 5.	109
Figure 4.47	Streamlines and the separation on the suction side taken from [66]. . . . .	109
Figure 4.48	Nondimensional pressure distribution on the airfoil surface for Case 5. . . . .	110
Figure 4.49	Convergence history for Case 5. . . . .	110
Figure 4.50	Surface mesh for Case 1. . . . .	113
Figure 4.51	Pressure contours on the vertical plane of symmetry at 8° angle of attack for Case 1. . . . .	113
Figure 4.52	Axial force coefficient for Case 1. . . . .	114
Figure 4.53	Normal force coefficient for Case 1. . . . .	114
Figure 4.54	Pitching moment coefficient for Case 1. . . . .	115
Figure 4.55	Surface mesh with partitions for Case 2. . . . .	116
Figure 4.56	Mach number contours for Case 2. . . . .	116
Figure 4.57	Surface pressure coefficient at $y/b=0.2$ for Case 2. . . . .	117
Figure 4.58	Surface pressure coefficient at $y/b=0.44$ for Case 2. . . . .	118
Figure 4.59	Surface pressure coefficient at $y/b=0.65$ for Case 2. . . . .	118
Figure 4.60	Surface pressure coefficient at $y/b=0.8$ for Case 2. . . . .	119
Figure 4.61	Surface pressure coefficient at $y/b=0.95$ for Case 2. . . . .	119
Figure 4.62	Convergence history for Case 2. . . . .	120
Figure 4.63	Surface mesh for Case 3. . . . .	121
Figure 4.64	Pressure contours on the vertical plane of symmetry at 10° angle of attack for Case 3. . . . .	121
Figure 4.65	Axial force coefficient for Case 3. . . . .	122
Figure 4.66	Normal force coefficient for Case 3. . . . .	122
Figure 4.67	Pitching moment coefficient for Case 3. . . . .	123
Figure 4.68	Coarse mesh for Case 4. . . . .	124
Figure 4.69	Medium mesh for Case 4. . . . .	125
Figure 4.70	Fine mesh for Case 4. . . . .	125
Figure 4.71	Comparison of u-velocity profile in the boundary layer at $x=0.44$ for different meshes. . . . .	127
Figure 4.72	Comparison of v-velocity profile in the boundary layer at $x=0.44$ for different meshes. . . . .	127
Figure 4.73	Mach number contours and velocity vectors at $y=0$ plane for Case 4 (Medium mesh, zoomed view). . . . .	128

Figure 4.74 u-velocity profile in the boundary layer at $x=0.44$ for Case 4 (Medium mesh). . . . .	128
Figure 4.75 u-velocity profile in the boundary layer at $x=0.66$ for Case 4 (Medium mesh). . . . .	129
Figure 4.76 v-velocity profile in the boundary layer at $x=0.44$ for Case 4 (Medium mesh). . . . .	129
Figure 4.77 v-velocity profile in the boundary layer at $x=0.66$ for Case 4 (Medium mesh). . . . .	130
Figure 4.78 Convergence history for Case 4 (Medium mesh). . . . .	130

# LIST OF SYMBOLS

## ROMAN SYMBOLS

$a$	Spatial slope of the initial distribution function
$\bar{a}$	Spatial slope of the equilibrium distribution function
$A$	Time slope of the distribution function
$C_A$	Axial force coefficient
$C_m$	Pitching moment coefficient
$C_N$	Normal force coefficient
$C_p$	Heat capacity at constant pressure, Pressure coefficient
$C_v$	Heat capacity at constant volume
$e$	Internal energy
$E$	Total energy
$f$	Mass density distribution function (gas distribution function)
$f_e$	Equilibrium distribution function
$f_0$	Initial nonequilibrium distribution function
$F$	Particle distribution function
$\mathbf{f}_e$	External body force vector
$\mathbf{F}$	Flux vector
$\mathbf{F}_x^C$	Convective flux vector in x-direction
$\mathbf{F}_y^C$	Convective flux vector in y-direction
$\mathbf{F}_z^C$	Convective flux vector in z-direction
$\mathbf{F}_x^V$	Viscous flux vector in x-direction

$\mathbf{F}_y^V$	Viscous flux vector in y-direction
$\mathbf{F}_z^V$	Viscous flux vector in z-direction
$g$	Equilibrium distribution function (equilibrium state)
$g_0$	Equilibrium distribution function at the cell interface
$H$	Total enthalpy
$H(t)$	Boltzmann function
$k$	Boltzmann constant
$m$	Mass of a molecule
$M$	Mach number
$N$	Number of molecules
$\mathbf{n}$	Normal vector
$p$	Pressure
$Pr$	Prandtl number
$\dot{q}_h$	Rate of heat transfer by radiation or chemical reactions
$\mathbf{q}$	Conductive heat flux
$\mathbf{Q}$	Vector of conservative variables
$R$	Gas constant
$\mathbf{R}_e$	Residual vector
$t$	Time
$T$	Temperature
$u$	Microscopic velocity component in x-direction
$U$	Macroscopic velocity component in x-direction
$v$	Microscopic velocity component in y-direction
$V$	Macroscopic velocity component in y-direction
$\mathbf{v}$	Microscopic velocity vector
$\mathbf{V}$	Macroscopic velocity vector
$w$	Microscopic velocity component in z-direction
$W$	Macroscopic velocity component in z-direction

$x$	Local coordinate direction
$y$	Local coordinate direction
$z$	Local coordinate direction
$X$	Global coordinate direction
$Y$	Global coordinate direction
$Z$	Global coordinate direction

### GREEK SYMBOLS

$\gamma$	Specific heat ratio
$\zeta$	Bulk viscosity
$\kappa$	Thermal conductivity coefficient
$\mu$	Dynamic viscosity
$\xi$	Microscopic velocities due to internal motion
$\rho$	Density
$\tau$	Collision time
$\bar{\bar{\tau}}$	Stress tensor
$\varphi$	Summational invariant
$\psi$	Moments vector for the distribution function
$\Omega$	Control volume
$\mathfrak{S}$	Collision operator

### SUBSCRIPTS

$ci$	Cell interface
$L$	Left state
$R$	Right state

### SUPERSCRIPTS

$L$	Left state
$n$	Time step
$R$	Right state

# CHAPTER 1

## INTRODUCTION

There are, in general, two ways to describe fluid motion. The first one is the *continuum approach* which is based on macroscopic quantities such as mass, momentum and energy densities, as well as the physical laws governing the evolution of these quantities such as Euler and Navier-Stokes equations. The other description comes from microscopic considerations, i.e., *gas-kinetic theory*. The fundamental quantity in this description is the gas distribution function which gives the number density of the molecules in a six-dimensional phase space (physical and velocity space). The evolution equation for the gas distribution function is the Boltzmann equation. Physically, the gas-kinetic equation provides more information about the gas flow and has larger applicability than the macroscopic one.

Over the past years, there has been tremendous amount of effort to develop numerical methods for the solution of fluid flow equations especially in the

continuum approach. In the following section, the numerical methods developed so far have been reviewed in both continuum and gas-kinetic points of view.

## 1.1 Overview of Numerical Methods

### 1.1.1 Methods Based on Continuum Approach

In the continuum approach, an overwhelming number of numerical methods for the solution of the governing equations has been developed over the years and the development still continues. Most of these methods employ a separate discretization in space and in time. Generally, a computational grid is used first either to construct control volumes and to evaluate the flux integrals, or to approximate the spatial derivatives of the flow quantities. The resulting time-dependent equations are then advanced in time, starting from a known initial solution. The spatial discretization schemes can be investigated in three main categories, namely *finite difference*, *finite volume*, and *finite element* methods while the temporal discretization is performed using either *explicit* or *implicit* time integration schemes.

The finite difference method was the first method applied to the numerical solution of differential equations. It is directly applied to the differential form of the governing equations. The principle is to employ a Taylor series expansion for the discretization of the derivatives of the flow variables on structured grids. An important advantage of the finite difference methodology is its simplicity. Another advantage is the easy calculation of high-order approxima-

tions, and hence to achieve high-order accuracy. On the other hand, because the method requires a structured grid, its application for complex geometries is limited. Furthermore, the application of finite difference method on curvilinear grids requires coordinate transformation, which complicates its formulation.

The finite volume method utilizes the integral formulation of the fluid flow equations. It discretizes the governing equations by first dividing the physical domain into a number of discrete control volumes. The physical flux is then approximated by the sum of the fluxes crossing the individual faces of the control volume. There are basically two approaches in finite volume method for the solution strategy in control volumes: *cell-centered scheme* and *cell-vertex scheme*. In cell-centered scheme, the flow quantities are calculated at the centroids of the grid cells. Thus, the control volumes are identical to the grid cells. In cell-vertex scheme, the flow variables are calculated at the grid points. The control volume is generally constructed such that it is centered around the grid point. The main advantage of the finite volume method is that the spatial discretization is carried out directly in the physical space. Thus, there are no additional difficulties due to the coordinate transformation as in the case of the finite difference method. One further advantage over the finite difference method is that it is very flexible in terms of grid types used. It can be easily implemented on structured as well as on unstructured grids. Since the unstructured grids are suitable for the discretization of complex geometries, the finite volume method is widely used on unstructured grids.



The finite element method was originally employed for structural analysis only. However, at the beginning of the 1990's, the finite element method has gained popularity in the solution of the Euler and the Navier-Stokes equations. The finite element method starts with a subdivision of the physical domain into triangular (in 2-D) or into tetrahedral (in 3-D) elements. Thus, an unstructured grid has to be generated. Furthermore, the shape functions have to be defined, which represent the variation of the solution inside an element, and it is necessary to transform the governing equations from the differential form into an equivalent integral form. The finite element method is attractive because of its integral formulation and the use of unstructured grids, which are both preferable for flows in or around complex geometries. Moreover, it has been used as a basis for the development of finite volume methods. However, the finite element method has a very rigorous mathematical foundation and the numerical effort is much higher in most cases.

#### **1.1.1.1 Spatial Discretization and Flux Evaluations**

The finite difference, finite volume and finite element methods are the basic choices for the spatial discretization. Within each method, various numerical schemes exist to perform the spatial discretization of both convective and viscous fluxes. Only the schemes used for the discretization of convective fluxes, namely *central schemes* and *upwind schemes*, are considered here.

The first category of schemes, which is based on the usage of central finite difference, is known as central schemes. In these schemes, the physical properties

of the Euler equations, such as the characteristics, are not considered. The numerical stability of the central schemes can only be established by adding *artificial dissipation*, which is based on a blend of 2nd- and 4th-order differences of the flow variables. It should be noted that on unstructured/hybrid grids, the explicit Runge-Kutta time-stepping scheme can become unstable, when combined with a conventional central scheme. The main advantage of the central schemes is that they are easily implemented and computationally efficient in comparison to the upwind schemes.

The upwind schemes originate from the physical properties of the Euler equations. They distinguish between upstream and downstream wave propagation directions and are able to capture discontinuities much more accurately than central schemes. The major drawback of the upwind schemes is their inherent numerical diffusion. For second or higher order spatial accuracy, the upwind schemes may generate spurious oscillations near strong discontinuities and may need *limiters* in flux computations in order to prevent the numerical instability. The upwind schemes may be considered in two groups: *flux difference splitting schemes* (approximate Riemann solvers) and *flux vector splitting schemes*.

The flux difference splitting schemes are based on the solution of the Riemann problem for discontinuous states at an interface. The values of the flow variables on either side of the interface are generally termed as the *left* and *right state* values. The idea to solve a Riemann problem at the interface between two control volumes was first introduced by Godunov [1]. In the view of Go-

dunov's approach, several approximate Riemann solvers were introduced to enhance the efficiency of the exact Riemann solver, namely by Roe [2], Osher and Solomon [3] and Hartan, Lax and Van Leer [4]. In these methods, the numerical fluxes at a cell interface are computed by solving the Riemann problem approximately. In approximate solutions, the Riemann problem is either locally linearized or integrated along a simple path defined by the state variables.

The flux vector splitting schemes decompose the vector of convective fluxes into two parts according to the sign of certain characteristic variables. The first flux vector splitting schemes of this type were developed at the beginning of 1980's by Steger and Warming [5] and by Van Leer [6], respectively. A second class of flux vector splitting schemes decomposes the flux vector into a convective and a pressure (an acoustic) part. This idea is utilized by schemes like AUSM (Advection Upstream Splitting Method) scheme of Liou and Steffen [7], CUSP (Convective Upwind Split Pressure) scheme of Jameson [8, 9], LDFS (Low-Diffusion Flux-Splitting) scheme of Edwards [10] and MAPS (Mach number-based Advection Pressure Splitting) scheme of Rossow [10] with different physical and numerical interpretations. Although these schemes have been found more efficient and robust than the approximate Riemann solvers for many problems, they are not so accurate as approximate Riemann solvers.

The flux difference splitting schemes, especially Roe's approximate Riemann solver, have gained much popularity because of their excellent resolution of

boundary layers and shock-capturing property as well as easy implementation on structured and unstructured grids. However, widespread applications and intensive investigations have shown that approximate Riemann solvers still need to be improved to prevent unphysical solutions such as *expansion shocks*, *carbuncle phenomena*, *odd-even decoupling*, *kinked Mach stem* or failure of a local linearization leading to *negative density* and/or *pressure* [12-17].

### 1.1.2 Methods Based on Gas-Kinetic Theory

In order to overcome the drawbacks of approximate Riemann solvers and flux vector splitting schemes, researchers have adopted the kinetic formulations for continuum applications in the last two decades. One group of these kinetic approaches is the Lattice Gas Cellular Automata (LGCA) and Lattice Boltzmann Methods (LBM). LGCA and LBM are the methods for the simulation of fluid flows which are quite different from Molecular Dynamics and methods based on the spatial discretization of fluid flow equations (finite difference, finite volume and finite element methods). They are mainly based on discrete velocity models. The idea is to construct a lattice (empty or occupied by at most one particle) so that velocity or momentum can be assigned to particles by a vector connecting each node. The probability of particles in the lattice is given by the particle distribution function, which is governed by the Boltzmann equation. The microscopic interactions are local at the nodes and after collisions, the mass and momentum of the particles are updated and the particles are allowed to move to linked neighboring node accordingly. The introduction of LGCA and LBM and their history can be found in Refs. [18, 19, 20], and ref-

erences therein. Although there are numerous studies related to LGCA and LBM in the literature ranging from incompressible, turbulent flows and flows for non-ideal gases to high speed thermal flows [21-26], the general idea about LGCA and LBM is that they are most effective for and should be limited to the low-Mach number (nearly incompressible) flow simulations due to the sampling of the particle velocities around zero [27].

The other group of the kinetic approaches is based on the finite volume formulation and flux evaluation using the gas-kinetic theory. In contrast to wave motion that plays a key role in the Riemann solvers, the fundamental idea in this approach is the particle motion and its trajectory, which are described in a statistical fashion by a gas distribution function. The governing equation is the Boltzmann equation which describes the evolution of the gas distribution function in phase space under some assumptions. Due to the intrinsic non-linear nature of the collision mechanism reflected in the Boltzmann equation, simplified forms are usually used in deriving numerical fluxes. The central issue in this class of schemes is how to model the gas distribution function (or equivalently, particle motions) at a cell interface, from which numerical fluxes are obtained by calculation of moments. Most Boltzmann-type schemes adopt the collisionless Boltzmann equation, arguing that it can recover the Euler equations if the gas distribution is Maxwellian. After the development of the Beam scheme by Sanders and Prendergast [28], several versions of collisionless Boltzmann solver were developed by Reitz [29], Pullin (EFM, Equilibrium Flux Method) [30], Mandal and Deshpande (KFVS, Kinetic Flux Vector

Splitting) [31] and Perthame [32], which employ, in one way or another, up-winding at the particle level. The physics of particle motions behind this class of schemes, however, is that the left and right moving particles generated in each side from the equilibrium state are allowed to penetrate the other side through a cell boundary without collisions. Due to the absence of collision mechanism, these schemes always produce a large numerical viscosity and heat conductivity, which reduce their accuracy. In order to reduce and control artificial viscosity without losing the robustness of these methods, a numerical procedure which takes into account of particle collisions was introduced by Prendergast and Xu [33]. In this method, the collision effects were taken into account by employing the BGK model [34] as an approximation of the Boltzmann equation. In the following studies, the BGK based gas-kinetic methods have been well-established and extended to solve a wide range of applications [35-45]. The integral solution of the Gas-Kinetic BGK solvers has some advantages over the approximate Riemann solvers in terms of the flexibility of preparing initial data, the satisfaction of the entropy and positivity condition, a multidimensional gas evolution character and high level of robustness [35, 37, 46]. This indicates that the Gas-Kinetic BGK solver is a promising alternative to the approximate Riemann solvers for the spatial discretization of fluid flow equations. Despite its certain advantages over the classical schemes, the Gas-Kinetic BGK scheme has the major drawback of high computation time.

### 1.1.3 Parallel Computing

With the advent of computer technology in the last two decades, the use of parallel processing in Computational Fluid Dynamics (CFD) problems has attracted much attention especially when the problem consists of large systems of equations to be solved in large domains. With parallel processing, the computation time to solve a problem is significantly reduced by having several operations, each being a part of the original computation, performed at the same time. Today, parallel processing is a must for an efficient CFD algorithm/code which aims the solution of complex 3-D real configurations.

### 1.1.4 Hybrid Grids

The type of the grid utilized in the solution of fluid flow equations is an other important topic. Although numerical methods developed for the solution of Euler and Navier-Stokes equations initiated in structured grid context, the use of unstructured grids has become popular after 1990's. In structured grids, each grid point (vertex or node) is uniquely identified by the indices  $i, j, k$  and the corresponding cartesian coordinates  $x_{i,j,k}$ ,  $y_{i,j,k}$  and  $z_{i,j,k}$ . The grid cells are quadrilaterals in 2-D and hexahedra in 3-D. On the other hand, in unstructured grids, the grid cells as well as grid points have no particular ordering, i.e., neighboring cells or grid points cannot be directly identified by their indices. The grid cells are triangles in 2-D and tetrahedra in 3-D.

Both grid types have their own advantages and disadvantages. The main advantage of structured grids follows from the property that the indices  $i, j, k$

represent a computational space, since it directly corresponds to how the flow variables are stored in the computer memory. This property allows it to access the neighbors of a grid point very quickly and easily, just by adding or subtracting an integer value to or from the corresponding index. The evaluation of gradients, fluxes, and also the treatment of boundary conditions is greatly simplified by this feature. The major drawback is the generation of structured grids for complex geometries. Although this can be overcome by *multiblock* approach, the complexity of the flow solver is then increased. On the other hand, unstructured grids offer the largest flexibility in the treatment of complex geometries. The main advantage of the unstructured grids is based on the fact that triangular (2-D) or tetrahedral (3-D) grids can be generated automatically, independent of the complexity of the domain. Another advantage is that solution dependent grid refinement and coarsening can be handled in relatively native and easy manner. The disadvantages of unstructured grids are the necessity of employing sophisticated data structures inside the flow solver and the higher memory requirements.

Today, *hybrid grid* concept has become more feasible since it carries favorable features of both structured and unstructured grids. The hybrid grids usually consist of a mix of quadrilaterals and triangles in 2-D and of hexahedra, tetrahedra, prisms and pyramids in 3-D and they are mainly used in viscous flow simulations. Quadrilateral elements in 2-D and prismatic or hexahedral elements in 3-D are employed near the solid walls while the rest of the domain consists of triangles in 2-D and tetrahedra or pyramids in 3-D. The major ben-



enefit of such a hybrid grid is that the viscous boundary layers are well-resolved while the total number of grid cells, edges, faces and possibly of grid points is reduced. Although the generation of hybrid grids is non-trivial for geometrically demanding cases, the time required to construct a hybrid grid for a complex configuration is still significantly lower than the one required for a multiblock structured grid.

## **1.2 Objective of the Thesis**

The present thesis aims to accomplish the following tasks:

- Investigation of gas-kinetic theory based numerical methods in 1-D, intensive theoretical and numerical discussions and comparisons with classical methods through a wide range of application in order to show the accuracy and robustness of Gas-Kinetic BGK method.
- Design and analysis of finite volume Gas-Kinetic BGK method for 2-D and 3-D inviscid and viscous flows on unstructured/hybrid grids which is not done before.
- Implementation of Gas-Kinetic BGK method to obtain solutions on distributed computers to enhance the computation time.

## CHAPTER 2

# GOVERNING EQUATIONS OF FLUID FLOW AND GAS-KINETIC THEORY

There are two fundamental ways of describing fluid motion: *continuum approach* and *gas-kinetic theory*. In continuum approach, individual molecules are ignored and the fluid is viewed as a continuous matter. At each point of this continuous fluid, unique values of the density, velocity, pressure and temperature field are assumed to exist. The fact that this continuous fluid must obey the conservation laws of mass, momentum and energy gives rise to a set of partial differential equations (Euler or Navier-Stokes equations) in differential or integral form. These governing equations are closed by specifying equations of state and constitutive relations. Alternatively, the gas-kinetic theory treats the fluid as consisting of molecules whose motion is governed by the laws of dynamics. Actually, it attempts to derive the macroscopic behavior of the fluid by a statistical or probabilistic approach. The fundamental quantity is the gas

distribution function and the governing equation is the Boltzmann equation. The same set of partial differential equations in continuum approach can be obtained from the gas-kinetic theory provided that the fluid is in near equilibrium.

The validity of the two methods lies in two different domains. The continuum approach is appropriate only if the microscopic scale, *the mean free path* of molecules [47], is negligible compared to the smallest physical length scale of the flow field. On the other hand, the gas-kinetic theory is mainly used when the concept of continuum is no longer valid although it spans all the flow regimes in molecular level.

In this chapter, the basics of the continuum fluid flow and the gas-kinetic theory are reviewed. First, the governing equations are given in continuum point of view. Then, basic concepts of gas-kinetic theory is introduced. Finally, the relations between the two approaches are presented and the Euler and Navier-Stokes equations are derived from gas-kinetic point of view.

## **2.1 Continuum Fluid Flow and Governing Equations**

Fluid Dynamics is the investigation of interactive motion of a large number of individual particles. It is supposed that the density of the fluid is high enough so that it can be approximated as *continuum*. Continuum approach implies that even an infinitesimally small element of fluid still contains a sufficient number of particles for which mean velocity and mean kinetic energy

can be specified. In this way, one can be able to define velocity, pressure, temperature, density and other important quantities at each point of the fluid.

The derivation of the principal equations of fluid dynamics is based on the fact that the dynamical behavior of a fluid is determined by the following *conservation laws*, namely:

- the conservation of mass,
- the conservation of momentum,
- the conservation of energy.

In addition to the conservation laws, constitutive relations as well as the equation of state are necessary to close the system.

### 2.1.1 The Conservation of Mass

The conservation of mass states that the time rate of change of the total mass inside any fixed volume  $\Omega$  is equal to the net mass flow through some surface  $S$  on  $\Omega$ . In integral form, the conservation of mass is simply

$$\frac{\partial}{\partial t} \int_{\Omega} \rho \, d\Omega + \oint_{\partial\Omega} \rho (\mathbf{V} \cdot \mathbf{n}) \, dS = 0. \quad (2.1)$$

Using the divergence theorem, the differential form becomes

$$\frac{\partial \rho}{\partial t} + \frac{\partial(\rho u_i)}{\partial x_i} = 0. \quad (2.2)$$

### 2.1.2 The Conservation of Momentum

The conservation of momentum is derived from the *Newton's 2nd Law* which states that the time variation of momentum is caused by the net force acting

on a mass element

$$\frac{\partial}{\partial t} \int_{\Omega} \rho \mathbf{V} d\Omega + \oint_{\partial\Omega} \rho \mathbf{V} (\mathbf{V} \cdot \mathbf{n}) dS = \int_{\Omega} \mathbf{f}_e d\Omega - \oint_{\partial\Omega} p \mathbf{n} dS + \oint_{\partial\Omega} (\bar{\boldsymbol{\tau}} \cdot \mathbf{n}) dS \quad (2.3)$$

where  $\mathbf{f}_e$  are the *external body forces* (gravitational, magnetic, etc.) which act directly on the mass of the volume,  $p$  is the isotropic pressure component and  $\bar{\boldsymbol{\tau}}$  is the viscous stress tensor both of which act directly on the surface of the control volume and are called as *surface forces*. For Newtonian fluids, the constitutive relation between the stress tensor and flow variables is given by

$$\tau_{ij} = \mu \left[ \left( \frac{\partial u_i}{\partial x_j} + \frac{\partial u_j}{\partial x_i} \right) - \frac{2}{3} \delta_{ij} \frac{\partial u_k}{\partial x_k} \right] + \zeta \delta_{ij} \frac{\partial u_k}{\partial x_k}. \quad (2.4)$$

Here  $\mu$  is the dynamic viscosity,  $\zeta$  is the bulk viscosity and  $\delta_{ij}$  is the Kroneckers delta. The corresponding differential form of the momentum equation is

$$\frac{\partial(\rho u_i)}{\partial t} + \frac{\partial(\rho u_i u_j)}{\partial x_j} = f_i - \frac{\partial p}{\partial x_i} + \frac{\partial \tau_{ij}}{\partial x_j}. \quad (2.5)$$

### 2.1.3 The Conservation of Energy

The underlying principle behind the conservation of energy is the *1st Law of Thermodynamics*. For the control volume  $\Omega$ , any changes in time of total energy inside the volume are caused by the rate of work of forces acting on the volume and by the net heat flux into it. That is,

$$\begin{aligned} \frac{\partial}{\partial t} \int_{\Omega} \rho E d\Omega + \oint_{\partial\Omega} \rho E (\mathbf{V} \cdot \mathbf{n}) dS &= \oint_{\partial\Omega} (\mathbf{q} \cdot \mathbf{n}) dS \\ &+ \int_{\Omega} (\rho \mathbf{f}_e \cdot \mathbf{V} + \dot{q}_h) d\Omega - \oint_{\partial\Omega} p (\mathbf{V} \cdot \mathbf{n}) dS + \oint_{\partial\Omega} (\bar{\boldsymbol{\tau}} \cdot \mathbf{V}) \cdot \mathbf{n} dS \end{aligned} \quad (2.6)$$

where  $\mathbf{q}$  stands for the conductive heat flux, and  $\dot{q}_h$  the rate of heat transfer by radiation or chemical reactions. The constitutive relation is defined by the

Fourier's law of heat conduction

$$q_i = \kappa \frac{\partial T}{\partial x_i}. \quad (2.7)$$

Here  $\kappa$  is the thermal conductivity coefficient, and  $T$  is the absolute temperature. By divergence theorem, the differential form of the energy equation can be obtained:

$$\frac{\partial(\rho E)}{\partial t} + \frac{\partial(\rho E u_i)}{\partial x_i} = \frac{\partial}{\partial x_i} \left( \kappa \frac{\partial T}{\partial x_i} \right) + (\rho f_i u_i + \dot{q}_h) - p \frac{\partial u_i}{\partial x_i} + \frac{\partial(\tau_{ij} u_i)}{\partial x_j}. \quad (2.8)$$

#### 2.1.4 The Equation of State

In order to solve the set of conservation laws above with the constitutive relations, the equation of state which provides the relation between the thermodynamic variables must be specified. In aerodynamics, it is generally reasonable to assume that the fluid behaves like a perfect gas, for which the equation of state takes the form

$$p = \rho R T \quad (2.9)$$

where  $R$  denotes the specific gas constant. It is convenient to express the pressure in terms of conservative variables. Using the definitions

$$R = C_p - C_v, \quad \gamma = \frac{C_p}{C_v}$$

pressure is found to be

$$p = (\gamma - 1) \rho \left[ E - \frac{U^2 + V^2 + W^2}{2} \right]. \quad (2.10)$$

Finally, for air, the dynamic viscosity and the thermal conductivity coefficient can be specified as

$$\mu = \frac{1.45 \cdot 10^{-6} T^{3/2}}{T + 110},$$

$$\kappa = C_p \frac{\mu}{Pr}$$

where the Prandtl number,  $Pr$ , is commonly assumed to be constant at 0.72.

### 2.1.5 Summary

The conservation laws along with the constitutive relations and the equation of state give full description of a real fluid in continuum approach and this set of governing equations is called as the *Navier-Stokes equations*. In differential conservative form, the Navier-Stokes equations are summarized:

$$\frac{\partial \mathbf{Q}}{\partial t} + \frac{\partial \mathbf{F}_x^C}{\partial x} + \frac{\partial \mathbf{F}_y^C}{\partial y} + \frac{\partial \mathbf{F}_z^C}{\partial z} = \frac{\partial \mathbf{F}_x^V}{\partial x} + \frac{\partial \mathbf{F}_y^V}{\partial y} + \frac{\partial \mathbf{F}_z^V}{\partial z} + \mathbf{\Omega} \quad (2.11)$$

where

$$\mathbf{Q} = \begin{pmatrix} \rho \\ \rho U \\ \rho V \\ \rho W \\ \rho E \end{pmatrix},$$

$$\mathbf{F}_x^C = \begin{pmatrix} \rho U \\ \rho U^2 + p \\ \rho UV \\ \rho UW \\ \rho UH \end{pmatrix}, \quad \mathbf{F}_y^C = \begin{pmatrix} \rho V \\ \rho UV \\ \rho V^2 + p \\ \rho VW \\ \rho VH \end{pmatrix}, \quad \mathbf{F}_z^C = \begin{pmatrix} \rho W \\ \rho UW \\ \rho VW \\ \rho W^2 + p \\ \rho WH \end{pmatrix},$$

$$\mathbf{F}_x^V = \begin{pmatrix} 0 \\ \tau_{xx} \\ \tau_{yx} \\ \tau_{zx} \\ \Theta_x \end{pmatrix}, \quad \mathbf{F}_y^V = \begin{pmatrix} 0 \\ \tau_{xy} \\ \tau_{yy} \\ \tau_{zy} \\ \Theta_y \end{pmatrix}, \quad \mathbf{F}_z^V = \begin{pmatrix} 0 \\ \tau_{xz} \\ \tau_{yz} \\ \tau_{zz} \\ \Theta_z \end{pmatrix},$$

$$\mathbf{\Omega} = \begin{pmatrix} 0 \\ \rho f_x \\ \rho f_y \\ \rho f_z \\ \rho U f_x + \rho V f_y + \rho W f_z + \dot{q}_h \end{pmatrix},$$

with

$$H = E + \frac{p}{\rho},$$

$$\Theta_x = U\tau_{xx} + V\tau_{xy} + W\tau_{xz} + \kappa \frac{\partial T}{\partial x},$$

$$\Theta_y = U\tau_{yx} + V\tau_{yy} + W\tau_{yz} + \kappa \frac{\partial T}{\partial y},$$

$$\Theta_z = U\tau_{zx} + V\tau_{zy} + W\tau_{zz} + \kappa \frac{\partial T}{\partial z}.$$

When the effects of viscosity and heat conductivity are negligibly small, the real fluid can be approximated as an ideal fluid, the governing equations of which is called as the *Euler equations*. The Euler equations are obtained by taking the viscous fluxes,  $\mathbf{F}^V$ , and the source term,  $\mathbf{\Omega}$ , in Eq. (2.11) equal to 0.

## 2.2 Gas-Kinetic Theory

In contrast to the continuum approach, the gas-kinetic theory assumes that gases are comprised of large number of molecular constituents, whose motion



obey the laws of Newtonian mechanics. Directly solving the system with a large number of degrees of freedom, which is on the order of approximately  $10^{20}$ , is impossibly difficult nor actually necessary. Rather, the collective behavior of such systems are important. Therefore, a statistical description of the system becomes inevitable. The fundamental assumption in gas-kinetic theory is that complete information of the gas at, or near thermal equilibrium is included in a particle distribution function for the complete system

$$F(\mathbf{x}, \mathbf{v}, t) \tag{2.12}$$

where  $\mathbf{x}$  defines the space,  $\mathbf{v}$  the microscopic velocities, and  $t$  the time.

It is important to formulate and solve the transport equation for the particle distribution function with different collision processes dictated by the nature of the interactions between the molecules. The solution of the transport equation leads to the macroscopic properties and transport coefficient of the gas by taking the moments of the distribution function.

In this section, the gas distribution function and its moments are first presented. The full Boltzmann equation and the Boltzmann's H-theorem are discussed. Finally, the simplified form of the Boltzmann equation, namely the Boltzmann BGK equation and its solution are given.

### 2.2.1 The Gas Distribution Function and Its Moments

In gas-kinetic theory, the mass density is defined as

$$f(\mathbf{x}, \mathbf{v}, t) = m N F(\mathbf{x}, \mathbf{v}, t) \tag{2.13}$$

where  $m$  is the mass of a molecule,  $N$  is the number of molecules, and  $f$  is the mass density distribution function (hereafter  $f$  will be called as gas distribution function).

The macroscopic quantities, namely, the density, the velocity and the internal energy are found by taking the moments of the gas distribution function:

$$\rho(\mathbf{x}, t) = \int_{-\infty}^{+\infty} f(\mathbf{x}, \mathbf{v}, t) d\mathbf{v}, \quad (2.14)$$

$$\rho \mathbf{V}(\mathbf{x}, t) = \int_{-\infty}^{+\infty} \mathbf{v} f(\mathbf{x}, \mathbf{v}, t) d\mathbf{v}, \quad (2.15)$$

$$\rho e(\mathbf{x}, t) = \frac{1}{2} \int_{-\infty}^{+\infty} (\mathbf{v} - \mathbf{V})^2 f(\mathbf{x}, \mathbf{v}, t) d\mathbf{v}. \quad (2.16)$$

## 2.2.2 The Boltzmann Equation

The Boltzmann equation is the most widely accepted transport equation for the gas distribution function in gas-kinetic theory. It is a nonlinear integro-differential equation which is expressed as

$$\frac{\partial f}{\partial t} + \mathbf{v} \cdot \frac{\partial f}{\partial \mathbf{x}} = \mathfrak{S}(f, f) \quad (2.17)$$

where the external forces are ignored and the collision operator,  $\mathfrak{S}(f, f)$ , is given by

$$\mathfrak{S}(f, f) = \frac{1}{m} \int_S \int_{-\infty}^{+\infty} \|\mathbf{v}_1 - \mathbf{v}\| (f' f'_1 - f f_1) d\mathbf{v}_1 dS. \quad (2.18)$$

In the above equation,  $\mathbf{v}$  and  $\mathbf{v}_1$  are the velocities after a binary collision, and  $dS$  is the collision cross-section (see Refs. [47, 48] for the details of the Boltzmann equation and collision process). It can be shown that conservation constraint for the collision operator,  $\mathfrak{S}(f, f)$ , yields [48]

$$\int_{-\infty}^{+\infty} \mathfrak{S}(f, f) \varphi d\mathbf{v} = 0 \quad (2.19)$$

where  $\varphi$  is a summational invariant, which can be mass, momentum or energy.

In equilibrium,  $f$  is independent of time, and if there is no external force, it is independent of position. Then, the collision operator vanishes if and only if

$$f' f'_1 - f f_1 = 0.$$

The solution which satisfies the above condition is the *Maxwell-Boltzmann* (also called as Maxwellian or equilibrium) distribution function defined as

$$f_e = g = \rho \left( \frac{m}{2\pi k T} \right)^{\frac{D}{2}} \exp \left[ - \left( \frac{m}{2kT} \right) (\mathbf{v} - \mathbf{V})^2 \right] \quad (2.20)$$

where  $k$  is the Boltzmann constant and  $D$  is the dimension of the flow.

Defining the Boltzmann function as

$$H(t) = \int_{-\infty}^{+\infty} f \ln f \, d\mathbf{v}$$

the *Boltzmann's H-theorem* states that

$$\frac{dH(t)}{dt} \leq 0 \quad (2.21)$$

where the equality holds if and only if  $f = f_e = g$ . The above theorem indicates that the Boltzmann function,  $H(t)$ , is a non-increasing function of time. It can also be shown that

$$H(t) \geq H_e(t) \quad (2.22)$$

where  $H_e(t)$  is the Boltzmann function at equilibrium. These two results verify that  $H(t)$  is a monotonic function and is bounded from the below. Thus, the particle collisions cause the distribution function to approach the equilibrium state, which is given in Eq. (2.20). Moreover, Boltzmann's H-theorem

(Eq. (2.21)) is consistent with the *2nd Law of Thermodynamics*, which states that the entropy of an isolated system can not decrease.

Due to the nonlinear nature of the collision operator, it is very difficult to solve the Boltzmann equation directly. A more simplified version of the Boltzmann equation, called the *Boltzmann BGK equation*, was suggested by the Bhatnagar, Gross and Krook [34],

$$\frac{\partial f}{\partial t} + \mathbf{v} \cdot \frac{\partial f}{\partial \mathbf{x}} = \frac{g - f}{\tau} \quad (2.23)$$

where the external forces are ignored and  $\tau$  is the collision time. This model keeps the essential features of the collision mechanism. As shown above, the Boltzmann's H-theorem states that the collision mechanism drives the distribution function towards the equilibrium in an irreversible way, which is the main idea in the BGK model. The equilibrium distribution function for the Boltzmann BGK equation is defined as

$$g = \rho \left( \frac{m}{2\pi k T} \right)^{\frac{K+D}{2}} \exp \left\{ - \left( \frac{m}{2k T} \right) [(\mathbf{v} - \mathbf{V})^2 + \xi^2] \right\}. \quad (2.24)$$

where  $\xi = (\xi_1, \xi_2, \dots, \xi_K)$  is the  $K$ -dimensional vector of velocities due to internal energy and  $K$  is given by

$$K = \frac{2}{\gamma - 1} - D. \quad (2.25)$$

The only difference between Eq. (2.24) and Eq. (2.20) is the inclusion of  $\xi$ . For molecules with internal energy such as rotational and vibrational energy, the internal motion is taken into account with  $\xi$ . Since the equilibrium distribution function,  $g$ , is determined from the macroscopic variables, the mass, momentum and energy densities can be found by taking the moments of  $g$

$$\begin{pmatrix} \rho \\ \rho \mathbf{V} \\ \rho E \end{pmatrix} = \int_{-\infty}^{+\infty} \int_{-\infty}^{+\infty} g \begin{pmatrix} 1 \\ \mathbf{v} \\ \frac{1}{2}(\mathbf{v}^2 + \xi^2) \end{pmatrix} d\mathbf{v}d\xi. \quad (2.26)$$

The integral solution of the Boltzmann BGK equation [49] is

$$\begin{aligned} f(\mathbf{x}, \mathbf{v}, \xi, t) = & \frac{1}{\tau} \int_{t_0}^t g(\mathbf{x}', \mathbf{v}, \xi, t') \exp[-(t-t')/\tau] dt' \\ & + \exp[-(t-t_0)/\tau] f_0(\mathbf{x} - \mathbf{v}(t-t_0)) \end{aligned} \quad (2.27)$$

where  $\mathbf{x}' = \mathbf{x} - \mathbf{v}(t-t')$  is the trajectory of a particle,  $f_0$  is the initial nonequilibrium distribution function at  $t = t_0$ , and  $g$  is the equilibrium state approached by  $f$ .

### 2.3 Connection Between Two Descriptions of Fluid Flow

In this section, connection between the two descriptions of the fluid flow, namely the continuum approach and gas-kinetic theory, is revealed and the derivation of the Euler and Navier-Stokes equations from the Boltzmann BGK equation is presented. For a more detailed derivation, see for example, Refs. [47-50].

Starting with the nondimensionalized form of the Boltzmann BGK equation

$$\hat{\epsilon} \left( \frac{\partial \hat{f}}{\partial \hat{t}} + \hat{\mathbf{v}} \cdot \frac{\partial \hat{f}}{\partial \hat{\mathbf{x}}} \right) = \frac{\hat{g} - \hat{f}}{\hat{\tau}} \quad (2.28)$$

where  $\hat{\epsilon}$  is a small parameter, the *Chapman-Enskog expansion* is given as [49]

$$\hat{f} = \hat{g}_0 + \hat{\epsilon} \hat{g}_1 + \hat{\epsilon}^2 \hat{g}_2 + \dots = \sum_{n=0}^{+\infty} \hat{\epsilon}^n \hat{g}_n. \quad (2.29)$$

The recurrence relation here is

$$\hat{g}_n = -\left(\frac{\partial \hat{g}_{n-1}}{\partial \hat{t}} + \hat{\mathbf{v}} \cdot \frac{\partial \hat{g}_{n-1}}{\partial \hat{\mathbf{x}}}\right)$$

for  $n \geq 1$  and  $\hat{g}_0 = \hat{g}$ . To the zeroth order of  $\tau$ , similar approach yields  $f = g$ .

Substituting this result into Eq. (2.23) and taking the moments (see Appendix A for the calculation of these integrals)

$$\int_{-\infty}^{+\infty} \int_{-\infty}^{+\infty} \left(\frac{\partial g}{\partial t} + \mathbf{v} \cdot \frac{\partial g}{\partial \mathbf{x}}\right) \begin{pmatrix} 1 \\ \mathbf{v} \\ \frac{1}{2}(\mathbf{v}^2 + \xi^2) \end{pmatrix} d\mathbf{v}d\xi = 0, \quad (2.30)$$

the Euler equations are obtained:

$$\frac{\partial \mathbf{Q}}{\partial t} + \frac{\partial \mathbf{F}_x^C}{\partial x} + \frac{\partial \mathbf{F}_y^C}{\partial y} + \frac{\partial \mathbf{F}_z^C}{\partial z} = 0 \quad (2.31)$$

where

$$\mathbf{Q} = \begin{pmatrix} \rho \\ \rho U \\ \rho V \\ \rho W \\ \rho E \end{pmatrix}, \quad \mathbf{F}_x^C = \begin{pmatrix} \rho U \\ \rho U^2 + \frac{\rho}{2\lambda} \\ \rho UV \\ \rho UW \\ \frac{1}{2}\rho U(U^2 + V^2 + W^2 + \frac{K+5}{2\lambda}) \end{pmatrix},$$

$$\mathbf{F}_y^C = \begin{pmatrix} \rho V \\ \rho UV \\ \rho V^2 + \frac{\rho}{2\lambda} \\ \rho UW \\ \frac{1}{2}\rho V(U^2 + V^2 + W^2 + \frac{K+5}{2\lambda}) \end{pmatrix}, \quad \mathbf{F}_z^C = \begin{pmatrix} \rho W \\ \rho UW \\ \rho VW \\ \rho W^2 + \frac{\rho}{2\lambda} \\ \frac{1}{2}\rho W(U^2 + V^2 + W^2 + \frac{K+5}{2\lambda}) \end{pmatrix},$$

with  $\lambda = \frac{m}{2kT}$ , the pressure,  $p = \frac{\rho}{2\lambda}$ , and the total enthalpy,  $H = \frac{1}{2}(U^2 + V^2 + W^2 + \frac{K+5}{2\lambda})$ .

To the first order of  $\tau$ , the recurrence relation (Eq. (2.29)) says that the departure of  $f$  from the equilibrium state takes the form

$$f = g - \tau \left( \frac{\partial g}{\partial t} + \mathbf{v} \cdot \frac{\partial g}{\partial \mathbf{x}} \right).$$

Inserting this result into Eq. (2.23) and taking the moments of the both sides

$$\begin{aligned} & \int_{-\infty}^{+\infty} \int_{-\infty}^{+\infty} \left( \frac{\partial g}{\partial t} + \mathbf{v} \cdot \frac{\partial g}{\partial \mathbf{x}} \right) \begin{pmatrix} 1 \\ \mathbf{v} \\ \frac{1}{2}(\mathbf{v}^2 + \xi^2) \end{pmatrix} d\mathbf{v}d\xi \\ &= \tau \int_{-\infty}^{+\infty} \int_{-\infty}^{+\infty} \left[ \frac{\partial^2 g}{\partial t^2} + 2\mathbf{v} \cdot \frac{\partial}{\partial \mathbf{x}} \left( \frac{\partial g}{\partial t} \right) + \mathbf{v} \cdot \frac{\partial}{\partial \mathbf{x}} \left( \mathbf{v} \cdot \frac{\partial g}{\partial \mathbf{x}} \right) \right] \begin{pmatrix} 1 \\ \mathbf{v} \\ \frac{1}{2}(\mathbf{v}^2 + \xi^2) \end{pmatrix} d\mathbf{v}d\xi \quad (2.32) \end{aligned}$$

the Navier-Stokes equations are obtained:

$$\frac{\partial \mathbf{Q}}{\partial t} + \frac{\partial \mathbf{F}_x^C}{\partial x} + \frac{\partial \mathbf{F}_y^C}{\partial y} + \frac{\partial \mathbf{F}_z^C}{\partial z} = \frac{\partial \mathbf{F}_x^V}{\partial x} + \frac{\partial \mathbf{F}_y^V}{\partial y} + \frac{\partial \mathbf{F}_z^V}{\partial z} \quad (2.33)$$

where

$$\mathbf{Q} = \begin{pmatrix} \rho \\ \rho U \\ \rho V \\ \rho W \\ \rho E \end{pmatrix}, \quad \mathbf{F}_x^C = \begin{pmatrix} \rho U \\ \rho U^2 + \frac{\rho}{2\lambda} \\ \rho UV \\ \rho UW \\ \frac{1}{2}\rho U(U^2 + V^2 + W^2 + \frac{K+5}{2\lambda}) \end{pmatrix},$$

$$\mathbf{F}_y^C = \begin{pmatrix} \rho V \\ \rho UV \\ \rho V^2 + \frac{\rho}{2\lambda} \\ \rho UW \\ \frac{1}{2}\rho V(U^2 + V^2 + W^2 + \frac{K+5}{2\lambda}) \end{pmatrix}, \quad \mathbf{F}_z^C = \begin{pmatrix} \rho W \\ \rho UW \\ \rho VW \\ \rho W^2 + \frac{\rho}{2\lambda} \\ \frac{1}{2}\rho W(U^2 + V^2 + W^2 + \frac{K+5}{2\lambda}) \end{pmatrix},$$

$$\mathbf{F}_x^V = \begin{pmatrix} 0 \\ \tau_{xx}^* \\ \tau_{yx}^* \\ \tau_{zx}^* \\ \Theta_x^* \end{pmatrix}, \quad \mathbf{F}_y^V = \begin{pmatrix} 0 \\ \tau_{xy}^* \\ \tau_{yy}^* \\ \tau_{zy}^* \\ \Theta_y^* \end{pmatrix}, \quad \mathbf{F}_z^V = \begin{pmatrix} 0 \\ \tau_{xz}^* \\ \tau_{yz}^* \\ \tau_{zz}^* \\ \Theta_z^* \end{pmatrix},$$

with

$$\tau_{xx}^* = \tau p \left[ \left( \frac{4}{3} \frac{\partial U}{\partial x} \right) + \frac{2K}{3(K+3)} \left( \frac{\partial U}{\partial x} + \frac{\partial V}{\partial y} + \frac{\partial W}{\partial z} \right) \right],$$

$$\tau_{yy}^* = \tau p \left[ \left( \frac{4}{3} \frac{\partial V}{\partial y} \right) + \frac{2K}{3(K+3)} \left( \frac{\partial U}{\partial x} + \frac{\partial V}{\partial y} + \frac{\partial W}{\partial z} \right) \right],$$

$$\tau_{zz}^* = \tau p \left[ \left( \frac{4}{3} \frac{\partial W}{\partial z} \right) + \frac{2K}{3(K+3)} \left( \frac{\partial U}{\partial x} + \frac{\partial V}{\partial y} + \frac{\partial W}{\partial z} \right) \right],$$

$$\tau_{xy}^* = \tau_{yx}^* = \tau p \left( \frac{\partial U}{\partial y} + \frac{\partial V}{\partial x} \right),$$

$$\tau_{xz}^* = \tau_{zx}^* = \tau p \left( \frac{\partial U}{\partial z} + \frac{\partial W}{\partial x} \right),$$

$$\tau_{yz}^* = \tau_{zy}^* = \tau p \left( \frac{\partial V}{\partial z} + \frac{\partial W}{\partial y} \right),$$

$$\Theta_x^* = U\tau_{xx}^* + V\tau_{xy}^* + W\tau_{xz}^* + \tau p \left[ \frac{k(K+5)}{2m} \frac{\partial T}{\partial x} \right],$$

$$\Theta_y^* = U\tau_{yx}^* + V\tau_{yy}^* + W\tau_{yz}^* + \tau p \left[ \frac{k(K+5)}{2m} \frac{\partial T}{\partial y} \right],$$

$$\Theta_z^* = U\tau_{zx}^* + V\tau_{zy}^* + W\tau_{zz}^* + \tau p \left[ \frac{k(K+5)}{2m} \frac{\partial T}{\partial z} \right].$$



Here, the pressure and the total enthalpy are again  $p = \frac{\rho}{2\lambda}$ , and  $H = \frac{1}{2}(U^2 + V^2 + W^2 + \frac{K+5}{2\lambda})$ , respectively, the dynamic viscosity is  $\mu = \tau p$ , the bulk viscosity is  $\zeta = \mu \frac{2K}{3(K+3)}$  and the heat conductivity coefficient is  $\kappa = \mu \frac{k(K+5)}{2m}$ .

It should be noted that the above derivation of the Navier-Stokes equations from the Boltzmann BGK equation corresponds to a Prandtl number of 1. That is, the Boltzmann BGK equation for the Navier-Stokes solution gives only one parameter correct, namely, the dynamic viscosity or the heat conductivity coefficient and a model should be used to obtain both coefficients correctly.

## CHAPTER 3

### NUMERICAL METHOD

The gas-kinetic methods for the fluid flow solutions use the Boltzmann equation as the governing equation. The fundamental task in the construction of a finite volume gas-kinetic method is to evaluate the time-dependent gas distribution function at a cell interface, from which the numerical fluxes can be computed. That is, in a finite volume gas-kinetic method, the local solution of the Boltzmann equation is utilized to find the flux at the cell interface.

In this chapter, the gas-kinetic numerical method utilized for the solution of Euler and Navier-Stokes equations is presented in 2-D and 3-D, respectively. As a preliminary study, the gas-kinetic theory based methods are investigated in 1-D and intensive physical and numerical discussions are presented. The structure of the numerical methodology is then explained in 2-D and 3-D, respectively, in terms of spatial and temporal discretization. Finally, the boundary conditions and the parallel processing methodology employed are sum-

marized.

### 3.1 Preliminary Study on Gas-Kinetic Methods in 1-D

In this section, the finite volume gas-kinetic methods are presented in 1-D. Roe's flux difference splitting scheme is first reviewed and the discretized forms of the Kinetic Flux Vector Splitting and the Gas-Kinetic BGK schemes are then given. The physical and numerical aspect of these methods are discussed in detail.

#### 3.1.1 The Finite Volume Gas-Kinetic Methods

The finite volume gas-kinetic methods use the Boltzmann equation as the governing equation. The Boltzmann equation in 1-D can be written as

$$\frac{\partial f}{\partial t} + u \frac{\partial f}{\partial x} = \mathfrak{S}(f, f). \quad (3.1)$$

The connection between the gas distribution function and the macroscopic flow variables is

$$\mathbf{Q} = \begin{pmatrix} \rho \\ \rho U \\ \rho E \end{pmatrix} = \int_{-\infty}^{+\infty} \int_{-\infty}^{+\infty} f \begin{pmatrix} 1 \\ u \\ \frac{1}{2}(u^2 + \xi^2) \end{pmatrix} du d\xi, \quad (3.2)$$

and the corresponding numerical fluxes are

$$\mathbf{F}(\mathbf{Q}) = \begin{pmatrix} F_\rho \\ F_{\rho U} \\ F_{\rho E} \end{pmatrix} = \frac{1}{\Delta t} \int_0^{\Delta t} \int_{-\infty}^{+\infty} \int_{-\infty}^{+\infty} u f \begin{pmatrix} 1 \\ u \\ \frac{1}{2}(u^2 + \xi^2) \end{pmatrix} du d\xi dt. \quad (3.3)$$

Taking the moments of the Boltzmann equation and integrating with respect to  $du d\xi$  in phase space,  $dx$  in a numerical cell  $[x_{j-1/2}, x_{j+1/2}]$  and  $dt$  in a time step  $[t^n, t^{n+1}]$  (i.e., forward Euler temporal discretization), a finite volume gas-kinetic method can be constructed,

$$\begin{aligned} & \int_{t^n}^{t^{n+1}} \int_{x_{j-1/2}}^{x_{j+1/2}} \int_{-\infty}^{+\infty} \int_{-\infty}^{+\infty} \left( \frac{\partial f}{\partial t} + u \frac{\partial f}{\partial x} \right) \begin{pmatrix} 1 \\ u \\ \frac{1}{2} (u^2 + \xi^2) \end{pmatrix} du d\xi dx dt \\ &= \int_{t^n}^{t^{n+1}} \int_{x_{j-1/2}}^{x_{j+1/2}} \int_{-\infty}^{+\infty} \int_{-\infty}^{+\infty} \mathfrak{S}(f, f) \begin{pmatrix} 1 \\ u \\ \frac{1}{2} (u^2 + \xi^2) \end{pmatrix} du d\xi dx dt, \end{aligned} \quad (3.4)$$

from which one can get

$$\begin{aligned} \mathbf{Q}_j^{n+1} - \mathbf{Q}_j^n &= -\frac{\Delta t}{\Delta x} (\mathbf{F}_{j+1/2} - \mathbf{F}_{j-1/2}) \\ &+ \Delta t \int_{t^n}^{t^{n+1}} \int_{x_{j-1/2}}^{x_{j+1/2}} \int_{-\infty}^{+\infty} \int_{-\infty}^{+\infty} \mathfrak{S}(f, f) \begin{pmatrix} 1 \\ u \\ \frac{1}{2} (u^2 + \xi^2) \end{pmatrix} du d\xi dx dt. \end{aligned} \quad (3.5)$$

Here the last term (i.e., collision term) is already zero for the collisionless Boltzmann equation. For the Boltzmann BGK equation, this term also vanishes due to the conservation constraint given in Eq. (2.19). Thus, Eq. (3.5) becomes

$$\mathbf{Q}_j^{n+1} - \mathbf{Q}_j^n = -\frac{\Delta t}{\Delta x} (\mathbf{F}_{j+1/2} - \mathbf{F}_{j-1/2}). \quad (3.6)$$

where  $\mathbf{F}_{j+1/2}$  is the numerical flux across a cell interface. Similar finite volume formulations can be derived in 2-D and 3-D, respectively.

### 3.1.2 Roe's Flux Difference Splitting Scheme in 1-D

The philosophy behind Roe's approximate Riemann solver is to compute approximate solutions to the Riemann problem by considering the set of linear conservation laws. Its derivation is based on a one-dimensional interaction of characteristic waves. Hence, the velocities parallel to the cell interface are ignored and the differences in the parallel components are assumed to occur across the contact surface [2].

One-dimensional space is divided uniformly by numerical cells and each cell occupies a small space  $x \in [x_{j-1/2}, x_{j+1/2}]$  where  $j + 1/2$  denotes the cell interface between cells  $j$  and  $j + 1$ . The first order Roe's flux difference splitting schemes is presented below:

#### 3.1.2.1 The First Order Formulation

Since Roe scheme is based on linear conservative laws and the Euler equations are nonlinear, the equations are linearized by evaluating the Jacobian matrix  $\mathbf{A} = \partial\mathbf{F}/\partial\mathbf{Q}$  with the following averaged quantities:

$$\tilde{\rho} = \sqrt{\rho_j \rho_{j+1}}, \quad (3.7)$$

$$\tilde{U} = \frac{U_j + U_{j+1} \sqrt{\rho_{j+1}/\rho_j}}{1 + \sqrt{\rho_{j+1}/\rho_j}}, \quad (3.8)$$

$$\tilde{H} = \frac{H_j + H_{j+1} \sqrt{\rho_{j+1}/\rho_j}}{1 + \sqrt{\rho_{j+1}/\rho_j}}, \quad (3.9)$$

$$\tilde{a}^2 = (\gamma - 1) \left( \tilde{H} - \frac{\tilde{U}^2}{2} \right). \quad (3.10)$$

The Roe-averaged matrix  $\tilde{\mathbf{A}}$  is the mean value of  $\mathbf{A}$  with the following properties:

- $\tilde{\mathbf{A}}(\mathbf{Q}_j, \mathbf{Q}_{j+1}) \rightarrow \mathbf{A}(\mathbf{Q})$  as  $\mathbf{Q}_j \rightarrow \mathbf{Q}_{j+1} \rightarrow \mathbf{Q}$ ,
- $\tilde{\mathbf{A}}(\mathbf{Q}_j, \mathbf{Q}_{j+1})[\mathbf{Q}_{j+1} - \mathbf{Q}_j] = \mathbf{F}(\mathbf{Q}_{j+1}) - \mathbf{F}(\mathbf{Q}_j)$ ,
- $\tilde{\mathbf{A}}$  has a complete set of real eigenvalues and eigenvectors.

The third property ensures that the matrix  $\tilde{\mathbf{A}}$  has three independent eigenvalues, which allows the matrix to be written in canonical form:

$$|\tilde{\mathbf{A}}| = \tilde{\mathbf{R}} |\tilde{\mathbf{\Lambda}}| \tilde{\mathbf{L}} \quad (3.11)$$

where  $\tilde{\mathbf{R}}$  and  $\tilde{\mathbf{L}}$  are the right and left eigenvectors, respectively, and  $\tilde{\mathbf{\Lambda}}$  is the diagonal matrix of eigenvalues.

Finally, the numerical fluxes for the mass, momentum and energy across each cell interface can be found as

$$\mathbf{F}_{j+1/2} = \begin{pmatrix} F_\rho \\ F_{\rho U} \\ F_{\rho E} \end{pmatrix}_{j+1/2} = \frac{1}{2} [\mathbf{F}(\mathbf{Q}_j) + \mathbf{F}(\mathbf{Q}_{j+1}) - |\tilde{\mathbf{A}}| (\mathbf{Q}_{j+1} - \mathbf{Q}_j)]. \quad (3.12)$$

### 3.1.2.2 Physical and Numerical Analysis

As specified in the previous section, Roe's approximate Riemann solver is based on the linearized conservation laws and depends highly on the Jacobian matrix. The first property given ensures consistency of the governing equation so that the approximate solution tends to the exact solution for small dif-

ferences in data across the cell interface. Moreover, the second property guarantees that the Roe-averaged Jacobian matrix satisfies the Rankine-Hugoniot shock jump condition and is responsible for the sharp resolution of steady shock waves. However, a major problem may appear for expansion fans in some extreme cases and the entropy condition may be violated [2, 61]. In order to prevent this unphysical solution, an entropy fix should be employed and there is no mathematical or physical justification for applying such a fix. In addition, the scheme is not positivity preserving and negative density/pressure may be observed for a flow expanding into vacuum [51]. The dependency on the Jacobian matrix also limits the flexibility of the scheme. That is, the Jacobian matrix differs for flows with different equations of state (e.g., real gas flows) and the determination of the matrix for those cases is not always straightforward.

### 3.1.3 The Kinetic Flux Vector Splitting Scheme in 1-D

The Kinetic Flux Vector Splitting (KFVS) scheme is based on the collisionless Boltzmann equation, which ignores the particle collisions in the gas evolution. In this section, the first and second order accurate upwind formulations for one-dimensional flows are presented and the physical and numerical aspects are discussed in detail.

The collisionless Boltzmann equation in 1-D can be written as

$$\frac{\partial f}{\partial t} + u \frac{\partial f}{\partial x} = 0. \quad (3.13)$$

When the initial conditions are taken into consideration, the solution of this

equation around any  $x$  is

$$f = f_0(x - ut, t). \quad (3.14)$$

The equilibrium state is assumed to be a Maxwellian (see Eq. (2.24)) and has one-to-one correspondence with the macroscopic flow variables  $(\rho, \rho U, \rho E)$ :

$$g = \rho \left(\frac{\lambda}{\pi}\right)^{\frac{K+1}{2}} \exp \{-\lambda [(u - U)^2 + \xi^2]\} \quad (3.15)$$

where  $\lambda$  is given by

$$\lambda = \frac{m}{2kT} = \frac{K+1}{4} \frac{\rho}{\rho E - \frac{1}{2}\rho U^2}. \quad (3.16)$$

One-dimensional space is divided uniformly by numerical cells and each cell occupies a small space  $x \in [x_{j-1/2}, x_{j+1/2}]$  where  $j + 1/2$  denotes the cell interface between cells  $j$  and  $j + 1$ . The first and second order Kinetic Flux Vector Splitting schemes are presented below:

### 3.1.3.1 The First Order Formulation

Assuming two constant equilibrium states to the left and right of a cell interface (Fig. 3.1), the solution of the collisionless Boltzmann equation (Eq. (3.14)) at  $x_{j+1/2}$  and time  $t$  becomes

$$\begin{aligned} f(x_{j+1/2}, u, \xi, t) &= f_0(x - ut)|_{x=x_{j+1/2}} \\ &= g_j H(u) + g_{j+1} [1 - H(u)] \end{aligned} \quad (3.17)$$

where  $H(u)$  is the Heaviside function defined as

$$H(u) = \begin{cases} 0, & u < 0 \\ 1, & u > 0 \end{cases}.$$



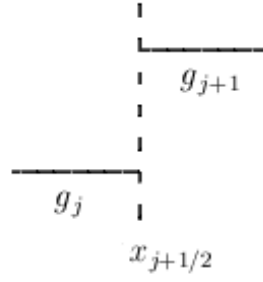


**Figure 3.1:** Constant initial gas distribution function for the first order KFVS scheme.

From the above distribution function, the numerical fluxes for the mass, momentum and energy across the cell interface can be found as

$$\mathbf{F}_{j+1/2} = \begin{pmatrix} F_\rho \\ F_{\rho U} \\ F_{\rho E} \end{pmatrix}_{j+1/2} = \int_{-\infty}^{+\infty} \int_{-\infty}^{+\infty} u f(x_{j+1/2}, u, \xi, t) \boldsymbol{\psi} du d\xi \quad (3.18)$$

$$= \int_{-\infty}^{+\infty} \int_0^{+\infty} u g_j \boldsymbol{\psi} du d\xi + \int_{-\infty}^{+\infty} \int_{-\infty}^0 u g_{j+1} \boldsymbol{\psi} du d\xi$$

where  $\boldsymbol{\psi}$  stands for moments vector

$$\boldsymbol{\psi} = \begin{pmatrix} 1 \\ u \\ \frac{1}{2}(u^2 + \xi^2) \end{pmatrix}. \quad (3.19)$$

Using the recursive relations given in Appendix A to calculate these integrals, the explicit form of the numerical fluxes in Eq. (3.18) becomes

$$\begin{pmatrix} F_\rho \\ F_{\rho U} \\ F_{\rho E} \end{pmatrix}_{j+1/2} = \rho_j \begin{pmatrix} \frac{U_j}{2} \operatorname{erfc}(-\sqrt{\lambda_j} U_j) + \frac{1}{2} \frac{\exp(-\lambda_j U_j^2)}{\sqrt{\pi \lambda_j}} \\ (\frac{U_j^2}{2} + \frac{1}{4\lambda_j}) \operatorname{erfc}(-\sqrt{\lambda_j} U_j) + \frac{U_j}{2} \frac{\exp(-\lambda_j U_j^2)}{\sqrt{\pi \lambda_j}} \\ (\frac{U_j^3}{4} + \frac{K+3}{8\lambda_j} U_j) \operatorname{erfc}(-\sqrt{\lambda_j} U_j) + (\frac{U_j^2}{4} + \frac{K+2}{8\lambda_j}) \frac{\exp(-\lambda_j U_j^2)}{\sqrt{\pi \lambda_j}} \end{pmatrix}$$

$$+ \rho_{j+1} \left( \begin{array}{c} \frac{U_{j+1}}{2} \operatorname{erfc}(\sqrt{\lambda_{j+1}} U_{j+1}) - \frac{1}{2} \frac{\exp(-\lambda_{j+1} U_{j+1}^2)}{\sqrt{\pi \lambda_{j+1}}} \\ \left( \frac{U_{j+1}^2}{2} + \frac{1}{4\lambda_{j+1}} \right) \operatorname{erfc}(\sqrt{\lambda_{j+1}} U_{j+1}) - \frac{U_{j+1}}{2} \frac{\exp(-\lambda_{j+1} U_{j+1}^2)}{\sqrt{\pi \lambda_{j+1}}} \\ \left( \frac{U_{j+1}^3}{4} + \frac{K+3}{8\lambda_{j+1}} U_{j+1} \right) \operatorname{erfc}(\sqrt{\lambda_{j+1}} U_{j+1}) - \left( \frac{U_{j+1}^2}{4} + \frac{K+2}{8\lambda_{j+1}} \right) \frac{\exp(-\lambda_{j+1} U_{j+1}^2)}{\sqrt{\pi \lambda_{j+1}}} \end{array} \right)$$

where  $\operatorname{erfc}$  is the complementary error function (a special case of the incomplete gamma function) is defined as

$$\operatorname{erfc}(x) = \frac{2}{\pi} \int_x^\infty \exp(-t^2) dt.$$

### 3.1.3.2 The Second Order Formulation

For the second order scheme, the reconstruction of conservative variables is based on MUSCL (Monotonic Upstream Schemes for Conservation Laws) approach proposed by Van Leer [52]

$$\bar{\mathbf{Q}}_j = \mathbf{Q}_j + \frac{1}{2} (\widehat{\Delta \mathbf{Q}})_{j-\frac{1}{2}}, \quad (3.20)$$

$$\bar{\mathbf{Q}}_{j+1} = \mathbf{Q}_{j+1} - \frac{1}{2} (\widehat{\Delta \mathbf{Q}})_{j+\frac{3}{2}}, \quad (3.21)$$

where

$$\mathbf{Q} = \begin{pmatrix} \rho \\ \rho U \\ \rho E \end{pmatrix}$$

and *min-mod* slope limiter is used to prevent unwanted oscillations,

$$(\widehat{\Delta \mathbf{Q}})_{j-\frac{1}{2}} = \minmod [(\Delta \mathbf{Q})_{j-\frac{1}{2}}, \omega(\Delta \mathbf{Q})_{j+\frac{1}{2}}],$$

$$(\widehat{\Delta \mathbf{Q}})_{j+\frac{3}{2}} = \minmod [(\Delta \mathbf{Q})_{j+\frac{3}{2}}, \omega(\Delta \mathbf{Q})_{j+\frac{1}{2}}],$$

with

$$(\Delta \mathbf{Q})_{j+\frac{1}{2}} = \mathbf{Q}_{j+1} - \mathbf{Q}_j.$$

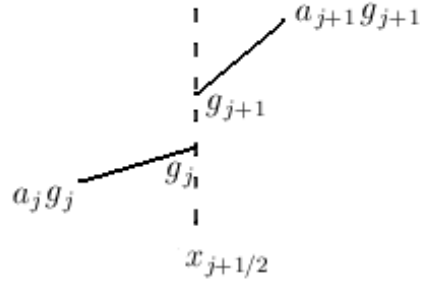


**Figure 3.2:** Linearly varying initial gas distribution function for the second order KFVS scheme.

The min-mod limiter function is defined as

$$\text{minmod}(a, \omega b) = \text{sgn}(a) \max\{0, \min[|a|, \omega b \text{sgn}(a)]\}$$

where  $1 \leq \omega \leq 2$  and  $\text{sgn}(x)$  denotes the sign of  $x$ .

Assuming two linearly varying equilibrium states to the left and right of a cell interface (Fig. 3.2), the solution of the collisionless Boltzmann equation at  $x_{j+1/2}$  and time  $t$  becomes

$$\begin{aligned} f(x_{j+1/2}, u, \xi, t) &= f_0(x - ut)|_{x=x_{j+1/2}} & (3.22) \\ &= g_j (1 - a_j ut) H(u) + g_{j+1} (1 - a_{j+1} ut) [1 - H(u)] \end{aligned}$$

where  $a_j$  and  $a_{j+1}$  are the spatial slopes of the form

$$a_j = a_j^{(1)} + a_j^{(2)} u + a_j^{(3)} \frac{1}{2} (u^2 + \xi^2), \quad (3.23)$$

$$a_{j+1} = a_{j+1}^{(1)} + a_{j+1}^{(2)} u + a_{j+1}^{(3)} \frac{1}{2} (u^2 + \xi^2). \quad (3.24)$$

Based on the relation between macroscopic and microscopic variables (see Eq. (2.26)), the equilibrium states to the left and right of the cell interface can

be determined using the Eqs. (3.20) and (3.21):

$$\bar{\mathbf{Q}}_j = \int_{-\infty}^{+\infty} \int_0^{+\infty} g_j \boldsymbol{\psi} du d\xi, \quad \bar{\mathbf{Q}}_{j+1} = \int_{-\infty}^{+\infty} \int_{-\infty}^0 g_{j+1} \boldsymbol{\psi} du d\xi. \quad (3.25)$$

Once  $g_j$  and  $g_{j+1}$  are obtained, the spatial slopes of the initial gas distribution function, which have unique correspondence with the slopes of the conservative variables to the left and right of the cell interface, can be found from

$$\frac{\bar{\mathbf{Q}}_j - \mathbf{Q}_j}{\Delta x} = \int_{-\infty}^{+\infty} \int_0^{+\infty} a_j g_j \boldsymbol{\psi} du d\xi, \quad (3.26)$$

$$\frac{\bar{\mathbf{Q}}_{j+1} - \mathbf{Q}_{j+1}}{\Delta x} = \int_{-\infty}^{+\infty} \int_{-\infty}^0 a_{j+1} g_{j+1} \boldsymbol{\psi} du d\xi. \quad (3.27)$$

Finally, the corresponding numerical fluxes for the mass, momentum and energy across the cell interface can be obtained using

$$\begin{aligned} \mathbf{F}_{j+1/2} &= \begin{pmatrix} F_\rho \\ F_{\rho U} \\ F_{\rho E} \end{pmatrix}_{j+1/2} = \frac{1}{\Delta t} \int_0^{\Delta t} \int_{-\infty}^{+\infty} \int_{-\infty}^{+\infty} u f(x_{j+1/2}, t, u, \xi) \boldsymbol{\psi} du d\xi dt \\ &= \frac{1}{\Delta t} \int_0^{\Delta t} \int_{-\infty}^{+\infty} \int_0^{+\infty} u g_j (1 - a_j ut) \boldsymbol{\psi} du d\xi dt \\ &\quad + \frac{1}{\Delta t} \int_0^{\Delta t} \int_{-\infty}^{+\infty} \int_{-\infty}^0 u g_{j+1} (1 - a_{j+1} ut) \boldsymbol{\psi} du d\xi dt. \end{aligned} \quad (3.28)$$

### 3.1.3.3 Physical and Numerical Analysis

The gas evolution model in the Kinetic Flux Vector Splitting scheme is based on the collisionless Boltzmann equation and it is shown in Chapter 2 that the Euler equations can be derived from the Boltzmann equation with a local equilibrium distribution function. Although the gas distribution is a Maxwellian

inside each cell, the real gas distribution function which is used to evaluate the numerical fluxes across the cell boundary is not Maxwellian at all; it is composed of *two half Maxwellians* in  $u < 0$  and  $u > 0$  regions separately (see Figs. 3.1 and 3.2). These nonequilibrium distributions do not correspond to the real Euler solutions! In order to better understand the physical and numerical mechanism, the first order scheme is analyzed in detail.

As every numerical scheme, the first order Kinetic Flux Vector Splitting scheme is composed of two parts: the *gas evolution* and the *projection*. In the gas evolution stage, the collisionless Boltzmann equation is solved and the particles can transport freely at this stage. This free transport mechanism in the gas evolution stage always evolves the system away from the Euler solutions (i.e.,  $f$  becomes more and more different from the Maxwellian)! In the projection stage, the conservative variables are averaged inside each cell through conservation principles to have an equilibrium state, which actually corresponds to a numerical collision process. Therefore, the projection stage drives the system back to approach the Euler solution (i.e., the preparation of the equilibrium state) and without the projection stage, the Kinetic Flux Vector Splitting scheme can not approach to Euler solutions.

On the other hand, the positivity property of the first order KFVS scheme has been proved [53]. That is, negative density or pressure have never been observed in the first order KFVS once the initial conditions are physically reasonable, even in the case of flow expanding into vacuum. Practically, positivity is an important property for any numerical scheme especially in the inviscid flow

solution of high speed flows. There are many popular methods which can not satisfy this property, one of which is Roe's approximate Riemann solver [51]!

It should also be noted that the evaluation of pressure which is based on the equation of state employed does not appear in the formulations explicitly. Therefore, the Kinetic Flux Vector Splitting scheme can easily be applied to real gas flows as opposed to the Roe scheme, which requires the reformulation of the Jacobian matrix.

In summary, although the KFVS scheme is positivity preserving and converges to the Euler solution with the time step  $\Delta t$  and cell size  $\Delta x$  approaching zero, with finite time step and cell size, the scheme usually gives dissipative results due to the underlying physical and numerical consideration (i.e., insufficient *numerical* collisions in the projection stage) and a real *physical* collision mechanism is necessary.

### 3.1.4 The Gas-Kinetic BGK Scheme in 1-D

The Gas-Kinetic BGK scheme is based on the Boltzmann BGK equation. In this section, the first and second order accurate upwind formulations for one-dimensional flows are presented and the physical and numerical aspects are discussed in detail.

The Boltzmann BGK equation in 1-D can be written as

$$\frac{\partial f}{\partial t} + u \frac{\partial f}{\partial x} = \frac{g - f}{\tau} \quad (3.29)$$

where  $g$  is the equilibrium state approached by  $f$  over particle collision time  $\tau$ ,

$$g = \rho \left(\frac{\lambda}{\pi}\right)^{\frac{K+1}{2}} \exp \{-\lambda [(u - U)^2 + \xi^2]\}. \quad (3.30)$$

Since mass, momentum and energy are conserved during particle collisions,  $f$  and  $g$  must satisfy the conservation constraint of

$$\int_{-\infty}^{+\infty} \int_{-\infty}^{+\infty} \frac{g - f}{\tau} \psi \, du \, d\xi = 0. \quad (3.31)$$

The general solution of this equation around any  $x$  is (see Eq. (2.27))

$$f(x, u, \xi, t) = \frac{1}{\tau} \int_0^t g(x', u, \xi, t') \exp[-(t-t')/\tau] \, dt' + \exp(-t/\tau) f_0(x-ut) \quad (3.32)$$

where  $x' = x - u(t - t')$  is the trajectory of a particle,  $f_0$  is the initial nonequilibrium distribution function and  $g$  is the corresponding equilibrium state.

One-dimensional space is divided uniformly by numerical cells and each cell occupies a small space  $x \in [x_{j-1/2}, x_{j+1/2}]$  where  $j + 1/2$  denotes the cell interface between cells  $j$  and  $j + 1$ . The first and second order Gas-Kinetic BGK schemes are presented below:

### 3.1.4.1 The First Order Formulation

Assuming two constant equilibrium states for the initial gas distribution function to the left and right of a cell interface and a constant equilibrium state at the cell interface (Fig. 3.3),

$$f_0(x - ut)|_{x=x_{j+1/2}} = g_j H(u) + g_{j+1} [1 - H(u)], \quad (3.33)$$

$$g|_{x=x_{j+1/2}} = g_0, \quad (3.34)$$

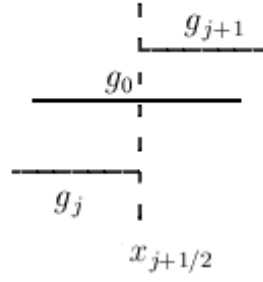


**Figure 3.3:** Constant initial gas distribution function and the equilibrium state for the first order Gas-Kinetic BGK scheme.

the solution of the Boltzmann BGK equation (Eq. 3.30) at  $x_{j+1/2}$  and time  $t$  becomes

$$f(x_{j+1/2}, u, \xi, t) = [1 - \exp(-t/\tau)] g|_{x=x_{j+1/2}} + \exp(-t/\tau) f_0|_{x=x_{j+1/2}}. \quad (3.35)$$

The equilibrium state at the cell interface,  $g_0$ , is found by applying the conservation constraint (Eq. (3.31)) along the cell interface

$$\begin{aligned} \int_{-\infty}^{+\infty} \int_{-\infty}^{+\infty} g_0 \psi \, du \, d\xi &= \int_{-\infty}^{+\infty} \int_{-\infty}^{+\infty} f_0(x - ut)|_{x=x_{j+1/2}} \psi \, du \, d\xi \\ &= \int_{-\infty}^{+\infty} \int_0^{+\infty} g_j \psi \, du \, d\xi + \int_{-\infty}^{+\infty} \int_{-\infty}^0 g_{j+1} \psi \, du \, d\xi. \end{aligned} \quad (3.36)$$

The underlying physical assumption in the above equation is that the left and right moving particles collapse at the cell interface to form an equilibrium state  $g_0$ .

From the above distribution function, the numerical fluxes for the mass, mo-



momentum and energy across the cell interface can be found as

$$\mathbf{F}_{j+1/2} = \begin{pmatrix} F_\rho \\ F_{\rho U} \\ F_{\rho E} \end{pmatrix}_{j+1/2} = \frac{1}{\Delta t} \int_0^{\Delta t} \int_{-\infty}^{+\infty} \int_{-\infty}^{+\infty} u f(x_{j+1/2}, u, \xi, t) \psi du d\xi dt. \quad (3.37)$$

In the first order Gas-Kinetic BGK scheme for 1-D flows, the term  $\exp(-t/\tau)$  in Eq. (3.35) is usually assumed to be a constant ( $\chi$ ). Using the relations in Appendix A, the explicit form of the numerical fluxes in Eq. (3.37) becomes

$$\begin{pmatrix} F_\rho \\ F_{\rho U} \\ F_{\rho E} \end{pmatrix}_{j+1/2} = \chi \begin{pmatrix} F_\rho^\dagger \\ F_{\rho U}^\dagger \\ F_{\rho E}^\dagger \end{pmatrix}_{j+1/2} + (1 - \chi) \begin{pmatrix} F_\rho^\ddagger \\ F_{\rho U}^\ddagger \\ F_{\rho E}^\ddagger \end{pmatrix}_{j+1/2}$$

where

$$\begin{pmatrix} F_\rho^\dagger \\ F_{\rho U}^\dagger \\ F_{\rho E}^\dagger \end{pmatrix}_{j+1/2} = \rho_j \begin{pmatrix} \frac{U_j}{2} \operatorname{erfc}(-\sqrt{\lambda_j} U_j) + \frac{1}{2} \frac{\exp(-\lambda_j U_j^2)}{\sqrt{\pi \lambda_j}} \\ (\frac{U_j^2}{2} + \frac{1}{4\lambda_j}) \operatorname{erfc}(-\sqrt{\lambda_j} U_j) + \frac{U_j}{2} \frac{\exp(-\lambda_j U_j^2)}{\sqrt{\pi \lambda_j}} \\ (\frac{U_j^3}{4} + \frac{K+3}{8\lambda_j} U_j) \operatorname{erfc}(-\sqrt{\lambda_j} U_j) + (\frac{U_j^2}{4} + \frac{K+2}{8\lambda_j}) \frac{\exp(-\lambda_j U_j^2)}{\sqrt{\pi \lambda_j}} \end{pmatrix} \\ + \rho_{j+1} \begin{pmatrix} \frac{U_{j+1}}{2} \operatorname{erfc}(\sqrt{\lambda_{j+1}} U_{j+1}) - \frac{1}{2} \frac{\exp(-\lambda_{j+1} U_{j+1}^2)}{\sqrt{\pi \lambda_{j+1}}} \\ (\frac{U_{j+1}^2}{2} + \frac{1}{4\lambda_{j+1}}) \operatorname{erfc}(\sqrt{\lambda_{j+1}} U_{j+1}) - \frac{U_{j+1}}{2} \frac{\exp(-\lambda_{j+1} U_{j+1}^2)}{\sqrt{\pi \lambda_{j+1}}} \\ (\frac{U_{j+1}^3}{4} + \frac{K+3}{8\lambda_{j+1}} U_{j+1}) \operatorname{erfc}(\sqrt{\lambda_{j+1}} U_{j+1}) - (\frac{U_{j+1}^2}{4} + \frac{K+2}{8\lambda_{j+1}}) \frac{\exp(-\lambda_{j+1} U_{j+1}^2)}{\sqrt{\pi \lambda_{j+1}}} \end{pmatrix},$$

and

$$\begin{pmatrix} F_\rho^\ddagger \\ F_{\rho U}^\ddagger \\ F_{\rho E}^\ddagger \end{pmatrix}_{j+1/2} = \rho_0 \begin{pmatrix} U_0 \\ U_0^2 + \frac{1}{2\lambda_0} \\ \frac{1}{2} U_0^3 + \frac{K+3}{4\lambda_0} U_0 \end{pmatrix}.$$

Here the conservative variables at equilibrium state are found from Eq. (3.36)

$$\begin{pmatrix} \rho_0 \\ \rho_0 U_0 \\ \rho_0 E_0 \end{pmatrix}_{j+1/2} = \rho_j \begin{pmatrix} \frac{1}{2} \operatorname{erfc}(-\sqrt{\lambda_j} U_j) \\ \frac{U_j}{2} \operatorname{erfc}(-\sqrt{\lambda_j} U_j) + \frac{1}{2} \frac{\exp(-\lambda_j U_j^2)}{\sqrt{\pi \lambda_j}} \\ \left(\frac{U_j^2}{2} + \frac{1}{4\lambda_j}\right) \operatorname{erfc}(-\sqrt{\lambda_j} U_j) + \frac{U_j}{2} \frac{\exp(-\lambda_j U_j^2)}{\sqrt{\pi \lambda_j}} \end{pmatrix} \\ + \rho_{j+1} \begin{pmatrix} \frac{1}{2} \operatorname{erfc}(\sqrt{\lambda_{j+1}} U_{j+1}) \\ \frac{U_{j+1}}{2} \operatorname{erfc}(\sqrt{\lambda_{j+1}} U_{j+1}) - \frac{1}{2} \frac{\exp(-\lambda_{j+1} U_{j+1}^2)}{\sqrt{\pi \lambda_{j+1}}} \\ \left(\frac{U_{j+1}^2}{2} + \frac{1}{4\lambda_{j+1}}\right) \operatorname{erfc}(\sqrt{\lambda_{j+1}} U_{j+1}) - \frac{U_{j+1}}{2} \frac{\exp(-\lambda_{j+1} U_{j+1}^2)}{\sqrt{\pi \lambda_{j+1}}} \end{pmatrix}.$$

### 3.1.4.2 The Second Order Formulation

For the second order scheme, the reconstruction of conservative variables is again based on MUSCL approach

$$\bar{\mathbf{Q}}_j = \mathbf{Q}_j + \frac{1}{2} (\Delta \widetilde{\mathbf{Q}})_{j-\frac{1}{2}}, \quad (3.38)$$

$$\bar{\mathbf{Q}}_{j+1} = \mathbf{Q}_{j+1} - \frac{1}{2} (\Delta \widehat{\mathbf{Q}})_{j+\frac{3}{2}}. \quad (3.39)$$

Assuming two linearly varying equilibrium states for the initial gas distribution function to the left and right of a cell interface and a linearly varying equilibrium state at the cell interface (Fig. 3.4),

$$\begin{aligned} f_0(x - ut)|_{x=x_{j+1/2}} &= g_j (1 - a_j ut) H(u) \\ &+ g_{j+1} (1 - a_{j+1} ut) [1 - H(u)], \end{aligned} \quad (3.40)$$

$$\begin{aligned} g|_{x=x_{j+1/2}} &= g_0 \{1 + H(u) (1 - \bar{a}_j ut) \\ &+ [1 - H(u)] (1 - \bar{a}_{j+1} ut) + \bar{A}t\}, \end{aligned} \quad (3.41)$$

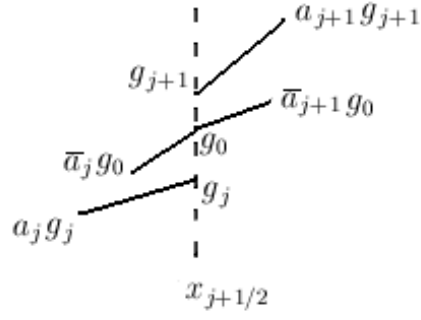


**Figure 3.4:** Linearly varying initial gas distribution function and the equilibrium state for the second order Gas-Kinetic BGK scheme.

the solution of the Boltzmann BGK equation (Eq. (3.29)) at  $x_{j+1/2}$  and time  $t$  becomes

$$\begin{aligned}
f(x_{j+1/2}, u, \xi, t) &= [1 - \exp(-t/\tau)] g_0 \\
&+ \{\tau [-1 + \exp(-t/\tau)]\} \{\bar{a}_j H(u) + \bar{a}_{j+1} [1 - H(u)]\} u g_0 \\
&+ \tau [t/\tau - 1 + \exp(-t/\tau)] \bar{A} g_0 \\
&+ \exp(-t/\tau) \{(1 - a_j ut) H(u) g_j \\
&+ (1 - a_{j+1} ut) [1 - H(u)] g_{j+1}\}.
\end{aligned} \tag{3.42}$$

Here  $a_j$  and  $a_{j+1}$  are the spatial slopes of the initial distribution function,  $\bar{a}_j$  and  $\bar{a}_{j+1}$  are the spatial slopes of the equilibrium state and  $\bar{A}$  is the time slope all given by

$$a_j = a_j^{(1)} + a_j^{(2)} u + a_j^{(3)} \frac{1}{2} (u^2 + \xi^2), \tag{3.43}$$

$$a_{j+1} = a_{j+1}^{(1)} + a_{j+1}^{(2)} u + a_{j+1}^{(3)} \frac{1}{2} (u^2 + \xi^2), \tag{3.44}$$

$$\bar{a}_j = \bar{a}_j^{(1)} + \bar{a}_j^{(2)} u + \bar{a}_j^{(3)} \frac{1}{2} (u^2 + \xi^2), \tag{3.45}$$

$$\bar{a}_{j+1} = \bar{a}_{j+1}^{(1)} + \bar{a}_{j+1}^{(2)} u + \bar{a}_{j+1}^{(3)} \frac{1}{2} (u^2 + \xi^2), \tag{3.46}$$

$$\bar{A} = \bar{A}^{(1)} + \bar{A}^{(2)}u + \bar{A}^{(3)}\frac{1}{2}(u^2 + \xi^2). \quad (3.47)$$

Based on the relation between macroscopic and microscopic variables (see Eq. (2.26)), the equilibrium states to the left and right of the cell interface can be determined using the Eqs. (3.38) and (3.39):

$$\bar{\mathbf{Q}}_j = \int_{-\infty}^{+\infty} \int_0^{+\infty} g_j \boldsymbol{\psi} du d\xi, \quad \bar{\mathbf{Q}}_{j+1} = \int_{-\infty}^{+\infty} \int_{-\infty}^0 g_{j+1} \boldsymbol{\psi} du d\xi. \quad (3.48)$$

Once  $g_j$  and  $g_{j+1}$  are obtained, the spatial slopes of the initial gas distribution function, which have unique correspondence with the slopes of the conservative variables to the left and right of the cell interface, can be found from

$$\frac{\bar{\mathbf{Q}}_j - \mathbf{Q}_j}{\Delta x} = \int_{-\infty}^{+\infty} \int_0^{+\infty} a_j g_j \boldsymbol{\psi} du d\xi, \quad (3.49)$$

$$\frac{\bar{\mathbf{Q}}_{j+1} - \mathbf{Q}_{j+1}}{\Delta x} = \int_{-\infty}^{+\infty} \int_{-\infty}^0 a_{j+1} g_{j+1} \boldsymbol{\psi} du d\xi \quad (3.50)$$

After determining  $f_0$ , the equilibrium state at the cell interface,  $g_0$ , can be obtained by applying the conservation constraint (Eq. 3.31) along the cell interface

$$\int_{-\infty}^{+\infty} \int_{-\infty}^{+\infty} g_0 \boldsymbol{\psi} du d\xi = \int_{-\infty}^{+\infty} \int_0^{+\infty} g_j \boldsymbol{\psi} du d\xi + \int_{-\infty}^{+\infty} \int_{-\infty}^0 g_{j+1} \boldsymbol{\psi} du d\xi \quad (3.51)$$

from which  $\rho_0$ ,  $\rho_0 U_0$  and  $\rho_0 E_0$  can be found. The spatial slopes of the equilibrium state can then be determined from

$$\frac{\bar{\mathbf{Q}}_j - \mathbf{Q}_0}{\Delta x} = \int_{-\infty}^{+\infty} \int_0^{+\infty} \bar{a}_j g_0 \boldsymbol{\psi} du d\xi, \quad (3.52)$$

$$\frac{\bar{\mathbf{Q}}_{j+1} - \mathbf{Q}_0}{\Delta x} = \int_{-\infty}^{+\infty} \int_{-\infty}^0 \bar{a}_{j+1} g_0 \boldsymbol{\psi} du d\xi. \quad (3.53)$$

Up to this point, the equilibrium states to the left, right and in the middle of the cell interface as well as the corresponding spatial slopes are determined.

The only unknown term is the time slope term  $\bar{A}$ . Since both  $f$  and  $g$  contain the time slope  $\bar{A}$ , the conservation constraint (Eq. (3.31)) at the cell interface can be applied and integrated over the time step  $\Delta t$

$$\int_0^{\Delta t} \int_{-\infty}^{+\infty} \int_{-\infty}^{+\infty} (f - g) \psi \, du \, d\xi \, dt = 0, \quad (3.54)$$

from which  $\bar{A}$  can be calculated.

Finally, the corresponding numerical fluxes for the mass, momentum and energy across the cell interface can be obtained using

$$\mathbf{F}_{j+1/2} = \begin{pmatrix} F_\rho \\ F_{\rho U} \\ F_{\rho E} \end{pmatrix}_{j+1/2} = \frac{1}{\Delta t} \int_0^{\Delta t} \int_{-\infty}^{+\infty} \int_{-\infty}^{+\infty} u f(x_{j+1/2}, u, \xi, t) \psi \, du \, d\xi \, dt. \quad (3.55)$$

### 3.1.4.3 Physical and Numerical Analysis

The gas evolution model in the Gas-Kinetic BGK scheme is based on the Boltzmann BGK equation, which takes into account the particle collisions. As stated by the Boltzmann's H-theorem, this physical collision mechanism, which is the main deficiency in the Kinetic Flux Vector Splitting scheme, causes the nonequilibrium gas distribution function to approach to the equilibrium state in the gas evolution stage. Thus, the Gas-Kinetic BGK scheme captures the Euler solutions without giving dissipative results. Moreover, the entropy increasing property in the gas evolution stage along with the dissipative property in the projection stage prevents the formation of any unphysical phenomena in the Gas-Kinetic BGK scheme.

As derived in Chapter 2, the Gas-Kinetic BGK scheme converges to the Navier-Stokes equations in its second order approximation. The viscous fluxes are related to the linear slope of the equilibrium state at the cell interface so that separate evaluation of the viscous fluxes is not necessary as in the classical schemes.

The positivity property of the first order Gas-Kinetic BGK scheme can be proved. Since  $g_0 > 0$ ,  $f_0 > 0$  and  $\chi \in [0, 1]$ ,  $f$  is strictly positive for all particle velocities. Therefore,  $f$  has a positive density and temperature at the cell interface due to the following relations

$$\int_{-\infty}^{+\infty} \int_{-\infty}^{+\infty} f \, dud\xi > 0; \quad \int_{-\infty}^{+\infty} \int_{-\infty}^{+\infty} u^2 f \, dud\xi - \frac{(\int_{-\infty}^{+\infty} \int_{-\infty}^{+\infty} u f \, dud\xi)^2}{\int_{-\infty}^{+\infty} \int_{-\infty}^{+\infty} f \, dud\xi} > 0.$$

Positive density and pressure at a cell interface does not mean that the final scheme will keep the density and pressure positive inside each cell in the next time step. However, the general proof of positivity for the Gas-Kinetic BGK scheme is very difficult. The difficulty is mainly due to the variation of  $\chi$  in a real flow situation and an inappropriate choice of  $\chi$  will not keep the scheme positive. There have been various numerical studies for different values of  $\chi$  and it has been shown numerically that the Gas-Kinetic BGK scheme satisfies the positivity up to a Mach number of  $10^4$  as long as  $\chi \in [0, 1]$  [54, 55].

From gas-kinetic theory, the collision time should depend on macroscopic flow variables such as density and temperature. For the Euler calculations, the collision time  $\tau$  is composed of two parts

$$\tau = C_1 \Delta t + \min[1, C_2 \frac{|\rho_{j+1}/\lambda_{j+1} - \rho_j/\lambda_j|}{(\rho_{j+1}/\lambda_{j+1} + \rho_j/\lambda_j)}] \Delta t \quad (3.56)$$

where  $\Delta t$  is the time step. The first term on the right hand side gives a limiting threshold for the collision time to avoid the blowing up of the scheme in the evaluations of  $\Delta t/\tau$  and  $\exp(\Delta t/\tau)$ . It also provides a background dissipation for the numerical calculations. For example, if  $C_1 = 0.01$ , there will be 100 collisions in the smooth flow regions, which means that the artificial viscosity coefficient in the Gas-Kinetic BGK scheme is reduced to 1/100 of the value in the KFVS scheme. The second term is related to the pressure jump which introduces additional artificial dissipation if high pressure gradients are present in the flow. Generally, for 1-D shock tube problems, the results are not sensitive to the values of  $C_1$  and  $C_2$ .  $C_1$  takes the values from 0.01 to 0.1 and  $C_2$  is on the order of 1. However, the values of  $C_1$  and  $C_2$  for 2-D and 3-D flows is a major question!

Similar to the Kinetic Flux Vector Splitting scheme, in the Gas-Kinetic BGK scheme, the evaluation of pressure, which is based on the equation of state employed, does not appear in the formulations explicitly. Therefore, the Gas-Kinetic BGK scheme can easily be applied to real gas flows as opposed to the Roe scheme, which requires the reformulation of the Jacobian matrix.

### **3.2 Numerical Methodology in 2-D and 3-D**

In this section, numerical methodology for the finite volume Gas-Kinetic BGK method in 2-D and 3-D is presented. Since the finite volume method is constructed on separate discretization in space and time, the methodology employed is explained in terms of spatial and temporal discretization.

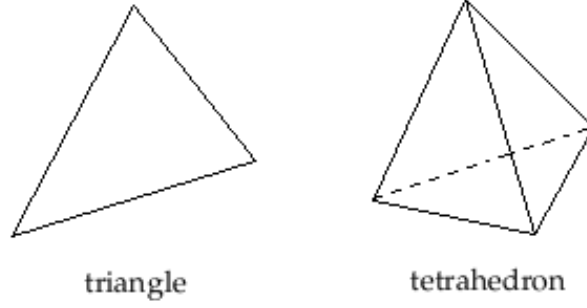


**Figure 3.5:** Elements of unstructured grids in 2-D and 3-D.

### 3.2.1 Spatial Discretization

The physical domain is first subdivided into a number of elements or control volumes in order to construct a finite volume spatial discretization. In the present study, unstructured and hybrid grids are employed. Unstructured grids consist of triangular and tetrahedral elements in 2-D and 3-D, respectively (Fig. 3.5). On the other hand, hybrid grids are comprised of triangular and quadrilateral elements in 2-D and a combination of tetrahedron, prismatic, pyramid and hexahedron elements are used in 3-D (Fig. 3.6).

Following the methodology given in § 3.1.1, finite volume spatial discretization for the Gas-Kinetic BGK method can be derived in 2-D and 3-D to be

$$\frac{\partial \mathbf{Q}}{\partial t} = -\frac{1}{\Omega} \oint_{\partial \Omega} \bar{\mathbf{F}} \cdot d\mathbf{S} \quad (3.57)$$

where  $\Omega$  is any control volume and the surface integral denotes the fluxes through control surfaces. Specifically, for the grid element volumes mentioned



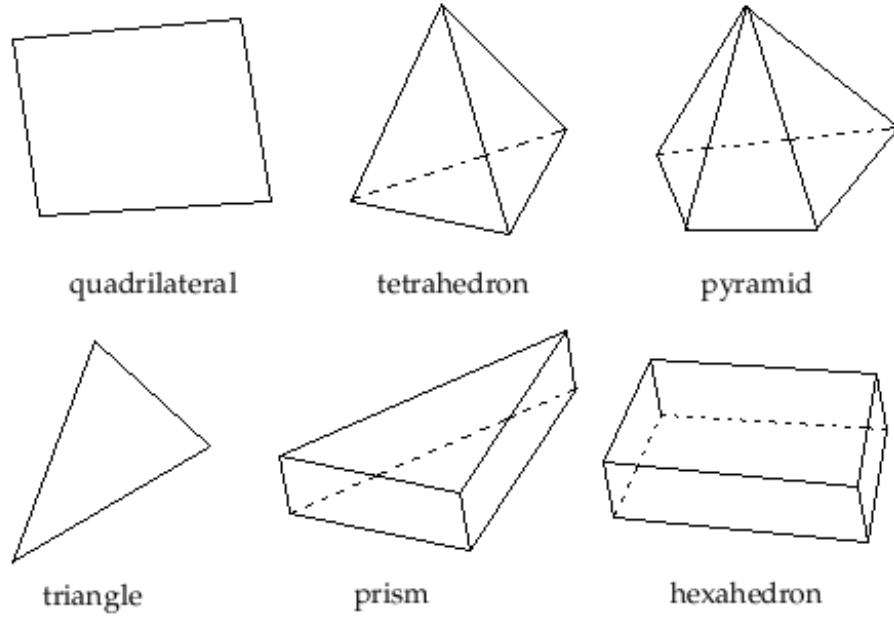


**Figure 3.6:** Elements of hybrid grids in 2-D and 3-D.

above, Eq. (3.57) can be approximated as

$$\frac{d\mathbf{Q}}{dt} = -\frac{1}{\Omega_e} \sum_{j=1}^N \mathbf{F}_{ci}^j \Delta S_j. \quad (3.58)$$

Here  $\Omega_e$  is the surface area or volume of the grid element,  $\Delta S_j$  is the length or surface area of the  $j$ th edge or surface,  $\mathbf{F}_{ci}^j$  is the numerical flux through the midpoint or centroid of  $j$ th edge or surface and  $N$  is the number of edges or faces in 2-D or 3-D, respectively. This approach is called as *cell-centered* approach, where the fluxes are evaluated through the boundaries of the grid elements and the conservative variables are updated at the cell centroids.

In the following sections, the Gas-Kinetic BGK scheme to evaluate the numerical fluxes (Eq. (3.58)) in 2-D and 3-D is presented.

### 3.2.1.1 The Gas-Kinetic BGK Scheme in 2-D

The Boltzmann BGK equation in 2-D can be written as

$$\frac{\partial f}{\partial t} + u \frac{\partial f}{\partial x} + v \frac{\partial f}{\partial y} = \frac{g - f}{\tau} \quad (3.59)$$

where  $g$  is the equilibrium state approached by  $f$  over particle collision time  $\tau$ ,

$$g = \rho \left(\frac{\lambda}{\pi}\right)^{\frac{K+2}{2}} \exp\{-\lambda[(u - U)^2 + (v - V)^2 + \xi^2]\}. \quad (3.60)$$

and  $\lambda$  is given by

$$\lambda = \frac{m}{2kT} = \frac{K+2}{4} \frac{\rho}{\rho E - \frac{1}{2}\rho(U^2 + V^2)}. \quad (3.61)$$

Since mass, momentum and energy are conserved during particle collisions,  $f$  and  $g$  must satisfy the conservation constraint of

$$\int_{-\infty}^{+\infty} \int_{-\infty}^{+\infty} \int_{-\infty}^{+\infty} \frac{g - f}{\tau} \boldsymbol{\psi} \, du \, dv \, d\xi = 0 \quad (3.62)$$

where  $\boldsymbol{\psi}$  is moments vector given by

$$\boldsymbol{\psi} = \begin{pmatrix} 1 \\ u \\ v \\ \frac{1}{2}(u^2 + v^2 + \xi^2) \end{pmatrix}. \quad (3.63)$$

The general solution of this equation around any  $s$  is

$$\begin{aligned} f(s, u, v, \xi, t) &= \frac{1}{\tau} \int_0^t g(s', u, v, \xi, t') \exp[-(t - t')/\tau] \, dt' \\ &\quad + \exp(-t/\tau) f_0(s - ut - vt) \end{aligned} \quad (3.64)$$

where  $s' = s - u(t - t') - v(t - t')$  is the trajectory of a particle,  $f_0$  is the initial nonequilibrium distribution function and  $g$  is the corresponding equilibrium state.

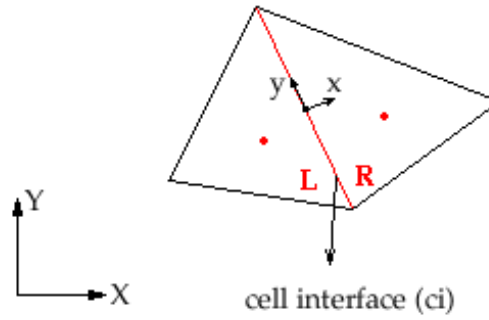


**Figure 3.7:** Sample triangular control volumes, cell interface and coordinate systems.

Consider the sample triangular control volumes, cell interface and coordinate systems given in Fig. 3.7 where *dots in red* represent cell centroids, the *dot in black* shows the midpoint of the cell interface,  $L$  and  $R$  the left and right states,  $x$  and  $y$  the local coordinate system normal and tangent to the cell interface  $ci$ , respectively,  $X$  and  $Y$  the global coordinate system. In cell-centered, finite volume Gas-Kinetic BGK scheme on unstructured/hybrid grids, the local coordinate system at the cell interface is used to find the numerical fluxes. The velocity components  $U_x$  and  $U_y$  in local (normal and tangential) coordinate system are found from global coordinate system counterparts  $U$  and  $V$ . The first and second order Gas-Kinetic BGK schemes are presented below:

### **The First Order Formulation**

Assuming two constant equilibrium states for the initial gas distribution function to the left and right of a cell interface and a constant equilibrium state at the cell interface

$$f_0(x - u_x t - u_y t)|_{x=x_{ci}} = g_L H(u_x) + g_R [1 - H(u_x)], \quad (3.65)$$

$$g|_{x=x_{ci}} = g_0, \quad (3.66)$$

the solution of the Boltzmann BGK equation at the cell interface  $x_{ci}$  and time  $t$  becomes

$$f|_{x=x_{ci}} = [1 - \exp(-t/\tau)] g|_{x=x_{ci}} + \exp(-t/\tau) f_0|_{x=x_{ci}}. \quad (3.67)$$

Here the equilibrium distribution functions to the left, right and in the middle of the cell interface  $ci$  are expressed as

$$g_* = \rho_* \left(\frac{\lambda_*}{\pi}\right)^{\frac{K+2}{2}} \exp\{-\lambda_* [(u_x^* - U_x^*)^2 + (u_y^* - U_y^*)^2 + \xi^2]\}. \quad (3.68)$$

The equilibrium state at the cell interface,  $g_0$ , is found by applying the conservation constraint (Eq. (3.62)) along the cell interface

$$\begin{aligned} & \int_{-\infty}^{+\infty} \int_{-\infty}^{+\infty} \int_{-\infty}^{+\infty} g_0 \boldsymbol{\psi}_{ci} du_x du_y d\xi \\ &= \int_{-\infty}^{+\infty} \int_{-\infty}^{+\infty} \int_{-\infty}^{+\infty} f_0(x - u_x t - u_y t)|_{x=x_{ci}} \boldsymbol{\psi}_{ci} du_x du_y d\xi \quad (3.69) \\ &= \int_{-\infty}^{+\infty} \int_{-\infty}^{+\infty} \int_0^{+\infty} \boldsymbol{\psi}_{ci} g_L du_x du_y d\xi \\ & \quad + \int_{-\infty}^{+\infty} \int_{-\infty}^{+\infty} \int_{-\infty}^0 \boldsymbol{\psi}_{ci} g_R du_x du_y d\xi. \end{aligned}$$

where  $\boldsymbol{\psi}_{ci}$  stands for moments vector

$$\boldsymbol{\psi}_{ci} = \begin{pmatrix} 1 \\ u_x \\ u_y \\ \frac{1}{2} (u_x^2 + u_y^2 + \xi^2) \end{pmatrix}. \quad (3.70)$$

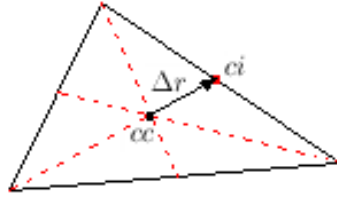


**Figure 3.8:** Reconstruction procedure in an arbitrary triangular cell.

From the above distribution function, the numerical fluxes for the mass, momentum and energy across the cell interface can be found as

$$\mathbf{F}_{ci} = \begin{pmatrix} F_{\rho} \\ F_{\rho U_x} \\ F_{\rho U_y} \\ F_{\rho E} \end{pmatrix}_{ci} = \frac{1}{\Delta t} \int_0^{\Delta t} \int_{-\infty}^{+\infty} \int_{-\infty}^{+\infty} \int_{-\infty}^{+\infty} u_x f|_{x=x_{ci}} \psi_{ci} du_x du_y d\xi dt. \quad (3.71)$$

The numerical fluxes found in the local coordinate system are finally converted to the global coordinate system.

### **The Second Order Formulation**

For the second order scheme, the reconstruction of conservative flow variables is achieved by expanding the cell-centered solution to each cell interface with a Taylor series (Fig. 3.8)

$$\mathbf{Q}_{ci} = \mathbf{Q}_{cc} + \nabla \mathbf{Q}_{cc} \Delta \mathbf{r} + O(\Delta \mathbf{r}^2) \quad (3.72)$$

where

$$\mathbf{Q} = \begin{pmatrix} \rho \\ \rho U \\ \rho V \\ \rho E \end{pmatrix},$$

$ci$  and  $cc$  refer to the cell interface and cell centroid, respectively and  $\Delta \mathbf{r}$  is the vector from the cell centroid to the midpoint of the cell interface. The midpoint pointwise values of  $\mathbf{Q}$  are first estimated by forming an arithmetic average of the two cells that share a common edge and then the gradient at the cell centroid is calculated using the midpoint trapezoidal rule.

Assuming two linearly varying equilibrium states for the initial gas distribution function to the left and right of a cell interface and a linearly varying equilibrium state at the cell interface,

$$\begin{aligned} f_0(x - u_x t - u_y t)|_{x=x_{ci}} &= g_L (1 - a_L u_x t) H(u_x) \\ &+ g_R (1 - a_R u_x t) [1 - H(u_x)], \end{aligned} \quad (3.73)$$

$$\begin{aligned} g|_{x=x_{ci}} &= g_0 \{1 + H(u_x) (1 - \bar{a}_L u_x t) \\ &+ [1 - H(u_x)] (1 - \bar{a}_R u_x t) + \bar{A}t\}, \end{aligned} \quad (3.74)$$

the solution of the Boltzmann BGK equation (Eq. (3.59)) at  $x_{ci}$  and time  $t$  becomes

$$\begin{aligned}
f|_{x=x_{ci}} &= [1 - \exp(-t/\tau)] g_0 & (3.75) \\
&+ \{\tau [-1 + \exp(-t/\tau)]\} \{\bar{a}_L H(u_x) + \bar{a}_R [1 - H(u_x)]\} u_x g_0 \\
&+ \tau [t/\tau - 1 + \exp(-t/\tau)] \bar{A} g_0 \\
&+ \exp(-t/\tau) \{(1 - a_L u_x t) H(u_x) g_L + (1 - a_R u_x t) [1 - H(u_x)] g_R\}.
\end{aligned}$$

Here  $a_L$  and  $a_R$  are the spatial slopes of the initial distribution function,  $\bar{a}_L$  and  $\bar{a}_R$  are the spatial slopes of the equilibrium state and  $\bar{A}$  is the time slope all given by

$$a_L = a_L^{(1)} + a_L^{(2)} u_x + a_L^{(3)} u_y + a_L^{(4)} \frac{1}{2} (u_x^2 + u_y^2 + \xi^2), \quad (3.76)$$

$$a_R = a_R^{(1)} + a_R^{(2)} u_x + a_R^{(3)} u_y + a_R^{(4)} \frac{1}{2} (u_x^2 + u_y^2 + \xi^2), \quad (3.77)$$

$$\bar{a}_L = \bar{a}_L^{(1)} + \bar{a}_L^{(2)} u_x + \bar{a}_L^{(3)} u_y + \bar{a}_L^{(4)} \frac{1}{2} (u_x^2 + u_y^2 + \xi^2), \quad (3.78)$$

$$\bar{a}_R = \bar{a}_R^{(1)} + \bar{a}_R^{(2)} u_x + \bar{a}_R^{(3)} u_y + \bar{a}_R^{(4)} \frac{1}{2} (u_x^2 + u_y^2 + \xi^2), \quad (3.79)$$

$$\bar{A} = \bar{A}^{(1)} + \bar{A}^{(2)} u_x + \bar{A}^{(3)} u_y + \bar{A}^{(4)} \frac{1}{2} (u_x^2 + u_y^2 + \xi^2). \quad (3.80)$$

Based on the relation between macroscopic and microscopic variables, the equilibrium states to the left and right of the cell interface can be determined:

$$\mathbf{Q}_{ci}^L = \int_{-\infty}^{+\infty} \int_{-\infty}^{+\infty} \int_0^{+\infty} g_L \psi_{ci} du_x du_y d\xi, \quad (3.81)$$

$$\mathbf{Q}_{ci}^R = \int_{-\infty}^{+\infty} \int_{-\infty}^{+\infty} \int_{-\infty}^0 g_R \psi_{ci} du_x du_y d\xi. \quad (3.82)$$

Once  $g_L$  and  $g_R$  are obtained, the spatial slopes of the initial gas distribution function, which have unique correspondence with the slopes of the conservative variables to the left and right of the cell interface, can be found from

$$\frac{\mathbf{Q}_{ci}^L - \mathbf{Q}_{cc}^L}{\Delta r} = \int_{-\infty}^{+\infty} \int_{-\infty}^{+\infty} \int_0^{+\infty} a_L g_L \psi_{ci} du_x du_y d\xi, \quad (3.83)$$

$$\frac{\mathbf{Q}_{ci}^R - \mathbf{Q}_{cc}^R}{\Delta r} = \int_{-\infty}^{+\infty} \int_{-\infty}^{+\infty} \int_{-\infty}^0 a_R g_R \psi_{ci} du_x du_y d\xi. \quad (3.84)$$

After determining  $f_0$ , the equilibrium state at the cell interface,  $g_0$ , can be obtained by using applying the conservation constraint along the cell interface

$$\begin{aligned} \int_{-\infty}^{+\infty} \int_{-\infty}^{+\infty} \int_{-\infty}^{+\infty} g_0 \psi_{ci} du_x du_y d\xi &= \int_{-\infty}^{+\infty} \int_{-\infty}^{+\infty} \int_0^{+\infty} g_L \psi_{ci} du_x du_y d\xi \\ &+ \int_{-\infty}^{+\infty} \int_{-\infty}^{+\infty} \int_{-\infty}^0 g_R \psi_{ci} du_x du_y d\xi \end{aligned} \quad (3.85)$$

from which the conservative variables at the cell interface can be found. The spatial slopes of the equilibrium state can then be determined from

$$\frac{\mathbf{Q}_{ci}^L - \mathbf{Q}_0}{\Delta r} = \int_{-\infty}^{+\infty} \int_{-\infty}^{+\infty} \int_0^{+\infty} \bar{a}_L g_0 \psi_{ci} du_x du_y d\xi, \quad (3.86)$$

$$\frac{\mathbf{Q}_{ci}^R - \mathbf{Q}_0}{\Delta r} = \int_{-\infty}^{+\infty} \int_{-\infty}^{+\infty} \int_{-\infty}^0 \bar{a}_R g_0 \psi_{ci} du_x du_y d\xi. \quad (3.87)$$

Up to this point, the equilibrium states to the left, right and in the middle of the cell interface as well as the corresponding spatial slopes are determined. The only unknown term is the time slope term  $\bar{A}$ . Since both  $f$  and  $g$  contain the time slope  $\bar{A}$ , the conservation constraint at the cell interface can be applied and integrated over the time step  $\Delta t$

$$\int_0^{\Delta t} \int_{-\infty}^{+\infty} \int_{-\infty}^{+\infty} \int_{-\infty}^{+\infty} (f - g) \psi_{ci} du_x du_y d\xi dt = 0 \quad (3.88)$$

from which  $\bar{A}$  can be calculated.

Finally, the corresponding numerical fluxes for the mass, momentum and energy across the cell interface can be obtained using



$$\mathbf{F}_{ci} = \begin{pmatrix} F_{\rho} \\ F_{\rho U_x} \\ F_{\rho U_y} \\ F_{\rho E} \end{pmatrix}_{ci} = \frac{1}{\Delta t} \int_0^{\Delta t} \int_{-\infty}^{+\infty} \int_{-\infty}^{+\infty} \int_{-\infty}^{+\infty} u_x f|_{x=x_{ci}} \boldsymbol{\psi}_{ci} du_x du_y d\xi dt. \quad (3.89)$$

The numerical fluxes found in the local coordinate system are then converted to the global coordinate system.

### 3.2.1.2 The Gas-Kinetic BGK Scheme in 3-D

The Boltzmann BGK equation in 3-D can be written as

$$\frac{\partial f}{\partial t} + u \frac{\partial f}{\partial x} + v \frac{\partial f}{\partial y} + w \frac{\partial f}{\partial z} = \frac{g - f}{\tau} \quad (3.90)$$

where  $g$  is the equilibrium state approached by  $f$  over particle collision time  $\tau$ ,

$$g = \rho \left(\frac{\lambda}{\pi}\right)^{\frac{K+3}{2}} \exp \{-\lambda [(u - U)^2 + (v - V)^2 + (w - W)^2 + \xi^2]\}. \quad (3.91)$$

and  $\lambda$  is given by

$$\lambda = \frac{m}{2kT} = \frac{K+3}{4} \frac{\rho}{\rho E - \frac{1}{2}\rho(U^2 + V^2 + W^2)}. \quad (3.92)$$

Since mass, momentum and energy are conserved during particle collisions,  $f$  and  $g$  must satisfy the conservation constraint of

$$\int_{-\infty}^{+\infty} \int_{-\infty}^{+\infty} \int_{-\infty}^{+\infty} \int_{-\infty}^{+\infty} \frac{g - f}{\tau} \boldsymbol{\psi} du dv dw d\xi = 0 \quad (3.93)$$

where  $\boldsymbol{\psi}$  stands for moments vector

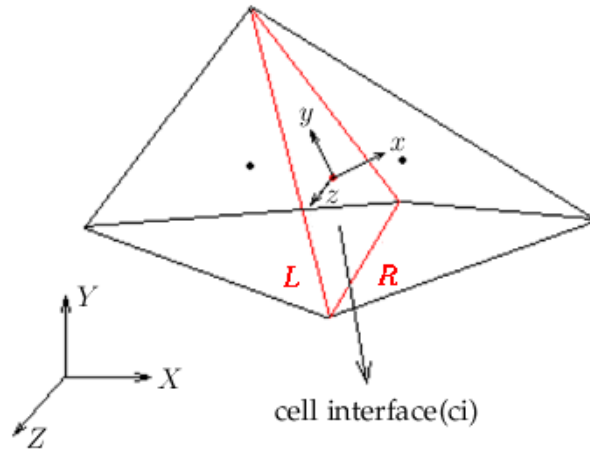


**Figure 3.9:** Sample tetrahedron control volumes, cell interface and coordinate systems.

$$\psi = \begin{pmatrix} 1 \\ u \\ v \\ w \\ \frac{1}{2}(u^2 + v^2 + w^2 + \xi^2) \end{pmatrix}. \quad (3.94)$$

The general solution of this equation around any  $s$  is

$$f(s, u, v, w, \xi, t) = \frac{1}{\tau} \int_0^t g(s', u, v, w, \xi, t') \exp[-(t-t')/\tau] dt' + \exp(-t/\tau) f_0(s - ut - vt - wt) \quad (3.95)$$

where  $s' = s - u(t-t') - v(t-t') - w(t-t')$  is the trajectory of a particle,  $f_0$  is the initial nonequilibrium distribution function and  $g$  is the corresponding equilibrium state.

Consider the sample tetrahedron control volumes, cell interface and coordinate systems given in Fig. 3.9 where *dots in black* represent cell centroids, the *dot in red* shows the cell interface centroid,  $L$  and  $R$  the left and right states,  $x$ ,  $y$  and  $z$  the local coordinate system normal and tangent to the cell interface  $ci$ , respectively,  $X$ ,  $Y$  and  $Z$  the global coordinate system. In cell-centered, finite volume Gas-Kinetic BGK scheme on unstructured/hybrid grids, the local coordinate system at the cell interface is used to find the numerical fluxes. The velocity components  $U_x$ ,  $U_y$  and  $U_z$  in local (normal and tangential) coordinate system are found from global coordinate system counterparts  $U$ ,  $V$  and  $W$ . The first and second order Gas-Kinetic BGK schemes are presented below:

### **The First Order Formulation**

Assuming two constant equilibrium states for the initial gas distribution function to the left and right of a cell interface and a constant equilibrium state at the cell interface

$$f_0(x - u_x t - u_y t - u_z t)|_{x=x_{ci}} = g_L H(u_x) + g_R [1 - H(u_x)], \quad (3.96)$$

$$g|_{x=x_{ci}} = g_0, \quad (3.97)$$

the solution of the Boltzmann BGK equation at the cell interface  $x_{ci}$  and time  $t$  becomes

$$f|_{x=x_{ci}} = [1 - \exp(-t/\tau)] g|_{x=x_{ci}} + \exp(-t/\tau) f_0|_{x=x_{ci}}. \quad (3.98)$$

Here the equilibrium distribution functions to the left, right and at the centroid of the cell interface  $ci$  are expressed as

$$g_* = \rho_* \left(\frac{\lambda_*}{\pi}\right)^{\frac{K+3}{2}} \exp\{-\lambda_* [(u_x^* - U_x^*)^2 + (u_y^* - U_y^*)^2 + (u_z^* - U_z^*)^2 + \xi^2]\}. \quad (3.99)$$

The equilibrium state at the cell interface,  $g_0$ , is found by applying the conservation constraint (Eq. (3.93)) across the cell interface

$$\begin{aligned}
& \int_{-\infty}^{+\infty} \int_{-\infty}^{+\infty} \int_{-\infty}^{+\infty} \int_{-\infty}^{+\infty} g_0 \boldsymbol{\psi}_{ci} du_x du_y du_z d\xi \\
&= \int_{-\infty}^{+\infty} \int_{-\infty}^{+\infty} \int_{-\infty}^{+\infty} \int_{-\infty}^{+\infty} f_0|_{x=x_{ci}} \boldsymbol{\psi}_{ci} du_x du_y du_z d\xi \quad (3.100) \\
&= \int_{-\infty}^{+\infty} \int_{-\infty}^{+\infty} \int_{-\infty}^{+\infty} \int_0^{+\infty} g_L \boldsymbol{\psi}_{ci} du_x du_y du_z d\xi \\
&\quad + \int_{-\infty}^{+\infty} \int_{-\infty}^{+\infty} \int_{-\infty}^{+\infty} \int_{-\infty}^0 g_R \boldsymbol{\psi}_{ci} du_x du_y du_z d\xi
\end{aligned}$$

where  $\boldsymbol{\psi}_{ci}$  stands for moments vector

$$\boldsymbol{\psi}_{ci} = \begin{pmatrix} 1 \\ u_x \\ u_y \\ u_z \\ \frac{1}{2} (u_x^2 + u_y^2 + u_z^2 + \xi^2) \end{pmatrix}. \quad (3.101)$$

From the above distribution function, the numerical fluxes for the mass, momentum and energy across the cell interface can be found as

$$\mathbf{F}_{ci} = \begin{pmatrix} F_\rho \\ F_{\rho U_x} \\ F_{\rho U_y} \\ F_{\rho U_z} \\ F_{\rho E} \end{pmatrix}_{ci} = \frac{1}{\Delta t} \int_0^{\Delta t} \int_{-\infty}^{+\infty} \int_{-\infty}^{+\infty} \int_{-\infty}^{+\infty} \int_{-\infty}^{+\infty} u_x f|_{x=x_{ci}} \boldsymbol{\psi}_{ci} du_x du_y du_z d\xi dt. \quad (3.102)$$

The numerical fluxes found in the local coordinate system are finally converted to the global coordinate system.

## The Second Order Formulation

For the second order scheme, the reconstruction of conservative flow variables is again achieved by expanding the cell-centered solution to each cell interface with a Taylor series

$$\mathbf{Q}_{ci} = \mathbf{Q}_{cc} + \nabla \mathbf{Q}_{cc} \Delta \mathbf{r} + O(\Delta \mathbf{r}^2) \quad (3.103)$$

where

$$\mathbf{Q} = \begin{pmatrix} \rho \\ \rho U \\ \rho V \\ \rho W \\ \rho E \end{pmatrix},$$

$ci$  and  $cc$  refer to the cell interface and cell centroid, respectively and  $\Delta \mathbf{r}$  is the vector from the cell centroid to the centroid of the cell interface. The centroidal pointwise values of  $\mathbf{Q}$  are first estimated by forming an arithmetic average of the two cells that share a common face and then the gradient at the cell centroid is calculated using the midpoint trapezoidal rule.

Assuming two linearly varying equilibrium states for the initial gas distribution function to the left and right of a cell interface and a linearly varying equilibrium state at the cell interface,

$$\begin{aligned} f_0(x - u_x t - u_y t - u_z t)|_{x=x_{ci}} &= g_L (1 - a_L u_x t) H(u_x) \\ &+ g_R (1 - a_R u_x t) [1 - H(u_x)], \end{aligned} \quad (3.104)$$

$$\begin{aligned}
g|_{x=x_{ci}} &= g_0 \{1 + H(u_x) (1 - \bar{a}_L u_x t) \\
&\quad + [1 - H(u_x)] (1 - \bar{a}_R u_x t) + \bar{A}t\}, \tag{3.105}
\end{aligned}$$

the solution of the Boltzmann BGK equation (Eq. (3.90)) at  $x_{ci}$  and time  $t$  becomes

$$\begin{aligned}
f|_{x=x_{ci}} &= [1 - \exp(-t/\tau)] g_0 \tag{3.106} \\
&\quad + \{\tau [-1 + \exp(-t/\tau)]\} \{\bar{a}_L H(u_x) + \bar{a}_R [1 - H(u_x)]\} u_x g_0 \\
&\quad + \tau [t/\tau - 1 + \exp(-t/\tau)] \bar{A} g_0 \\
&\quad + \exp(-t/\tau) \{(1 - a_L u_x t) H(u_x) g_L + (1 - a_R u_x t) [1 - H(u_x)] g_R\}.
\end{aligned}$$

Here  $a_L$  and  $a_R$  are the spatial slopes of the initial distribution function,  $\bar{a}_L$  and  $\bar{a}_R$  are the spatial slopes of the equilibrium state and  $\bar{A}$  is the time slope all given by

$$a_L = a_L^{(1)} + a_L^{(2)} u_x + a_L^{(3)} u_y + a_L^{(4)} u_z + a_L^{(5)} \frac{1}{2} (u_x^2 + u_y^2 + u_z^2 + \xi^2), \tag{3.107}$$

$$a_R = a_R^{(1)} + a_R^{(2)} u_x + a_R^{(3)} u_y + a_R^{(4)} u_z + a_R^{(5)} \frac{1}{2} (u_x^2 + u_y^2 + u_z^2 + \xi^2), \tag{3.108}$$

$$\bar{a}_L = \bar{a}_L^{(1)} + \bar{a}_L^{(2)} u_x + \bar{a}_L^{(3)} u_y + \bar{a}_L^{(4)} u_z + \bar{a}_L^{(5)} \frac{1}{2} (u_x^2 + u_y^2 + u_z^2 + \xi^2), \tag{3.109}$$

$$\bar{a}_R = \bar{a}_R^{(1)} + \bar{a}_R^{(2)} u_x + \bar{a}_R^{(3)} u_y + \bar{a}_R^{(4)} u_z + \bar{a}_R^{(5)} \frac{1}{2} (u_x^2 + u_y^2 + u_z^2 + \xi^2), \tag{3.110}$$

$$\bar{A} = \bar{A}^{(1)} + \bar{A}^{(2)} u_x + \bar{A}^{(3)} u_y + \bar{A}^{(4)} u_z + \bar{A}^{(5)} \frac{1}{2} (u_x^2 + u_y^2 + u_z^2 + \xi^2). \tag{3.111}$$

Based on the relation between macroscopic and microscopic variables, the equilibrium states to the left and right of the cell interface can be determined:

$$\mathbf{Q}_{ci}^L = \int_{-\infty}^{+\infty} \int_{-\infty}^{+\infty} \int_{-\infty}^{+\infty} \int_0^{+\infty} g_L \psi_{ci} du_x du_y du_z d\xi, \tag{3.112}$$

$$\mathbf{Q}_{ci}^R = \int_{-\infty}^{+\infty} \int_{-\infty}^{+\infty} \int_{-\infty}^{+\infty} \int_{-\infty}^0 g_R \psi_{ci} du_x du_y du_z d\xi. \tag{3.113}$$

Once  $g_L$  and  $g_R$  are obtained, the spatial slopes of the initial gas distribution function, which have unique correspondence with the slopes of the conservative variables to the left and right of the cell interface, can be found from

$$\frac{\mathbf{Q}_{ci}^L - \mathbf{Q}_{cc}^L}{\Delta r} = \int_{-\infty}^{+\infty} \int_{-\infty}^{+\infty} \int_{-\infty}^{+\infty} \int_0^{+\infty} a_L g_L \psi_{ci} du_x du_y du_z d\xi, \quad (3.114)$$

$$\frac{\mathbf{Q}_{ci}^R - \mathbf{Q}_{cc}^R}{\Delta r} = \int_{-\infty}^{+\infty} \int_{-\infty}^{+\infty} \int_{-\infty}^{+\infty} \int_{-\infty}^0 a_R g_R \psi_{ci} du_x du_y du_z d\xi. \quad (3.115)$$

After determining  $f_0$ , the equilibrium state at the cell interface,  $g_0$ , can be obtained by using applying the conservation constraint along the cell interface

$$\begin{aligned} & \int_{-\infty}^{+\infty} \int_{-\infty}^{+\infty} \int_{-\infty}^{+\infty} \int_{-\infty}^{+\infty} g_0 \psi_{ci} du_x du_y du_z d\xi \\ &= \int_{-\infty}^{+\infty} \int_{-\infty}^{+\infty} \int_{-\infty}^{+\infty} \int_0^{+\infty} g_L \psi_{ci} du_x du_y du_z d\xi \\ & \quad + \int_{-\infty}^{+\infty} \int_{-\infty}^{+\infty} \int_{-\infty}^{+\infty} \int_{-\infty}^0 g_R \psi_{ci} du_x du_y du_z d\xi \end{aligned} \quad (3.116)$$

from which the conservative variables at the cell interface can be found. The spatial slopes of the equilibrium state can then be determined from

$$\frac{\mathbf{Q}_{ci}^L - \mathbf{Q}_0}{\Delta r} = \int_{-\infty}^{+\infty} \int_{-\infty}^{+\infty} \int_{-\infty}^{+\infty} \int_0^{+\infty} \bar{a}_L g_0 \psi_{ci} du_x du_y du_z d\xi, \quad (3.117)$$

$$\frac{\mathbf{Q}_{ci}^R - \mathbf{Q}_0}{\Delta r} = \int_{-\infty}^{+\infty} \int_{-\infty}^{+\infty} \int_{-\infty}^{+\infty} \int_{-\infty}^0 \bar{a}_R g_0 \psi_{ci} du_x du_y du_z d\xi. \quad (3.118)$$

Up to this point, the equilibrium states to the left, right and at the centroid of the cell interface as well as the corresponding spatial slopes are determined. The only unknown term is the time slope term  $\bar{A}$ . Since both  $f$  and  $g$  contain the time slope  $\bar{A}$ , the conservation constraint at the cell interface can be applied and integrated over the time step  $\Delta t$

$$\int_0^{\Delta t} \int_{-\infty}^{+\infty} \int_{-\infty}^{+\infty} \int_{-\infty}^{+\infty} \int_{-\infty}^{+\infty} (f - g) \psi_{ci} du_x du_y du_z d\xi dt = 0 \quad (3.119)$$

from which  $\bar{A}$  can be calculated.

Finally, the corresponding numerical fluxes for the mass, momentum and energy across the cell interface can be obtained using

$$\mathbf{F}_{ci} = \begin{pmatrix} F_\rho \\ F_{\rho U_x} \\ F_{\rho U_y} \\ F_{\rho U_z} \\ F_{\rho E} \end{pmatrix}_{ci} = \frac{1}{\Delta t} \int_0^{\Delta t} \int_{-\infty}^{+\infty} \int_{-\infty}^{+\infty} \int_{-\infty}^{+\infty} u_x f|_{x=x_{ci}} \psi_{ci} du_x du_y du_z d\xi dt. \quad (3.120)$$

The numerical fluxes found in the local coordinate system are then converted to the global coordinate system.

### 3.2.1.3 Inviscid and Viscous Solutions From the Gas-Kinetic BGK Scheme

In this section, the first and second order Gas-Kinetic BGK schemes are discussed for the Euler and Navier-Stokes solutions and the some simplified versions are given.

For the first order Gas-Kinetic BGK scheme, the gas distribution function at the cell interface (Eq. (3.67) or (3.98)), which is comprised of the constant states, is rewritten as

$$f|_{x=x_{ci}} = g_0 + \exp(-t/\tau) (f_0 - g_0). \quad (3.121)$$

The first term in Eq. (3.121) is similar to the well-known Lax-Wendroff type Euler fluxes presented in [56]. The second term is the dissipation term, which should be large in discontinuous regions in order to keep  $f$  staying in a nonequi-



librium state. As a result, the parameter  $\exp(-t/\tau)$  should go to zero in smooth regions and should be large in discontinuous regions. There is not any parameter related to the viscous terms, thus, the first order Gas-Kinetic BGK scheme could only be used for the Euler solutions. For steady state solutions, Eq. (3.121) could be simplified further. The parameter  $\exp(-t/\tau)$  is replaced by a local switching function and a time-independent gas distribution function is obtained

$$f|_{x=x_{ci}} = g_0 + \epsilon (f_0 - g_0) \quad (3.122)$$

where the switching function  $\epsilon$  is related to the local pressure gradient:

$$\epsilon = 1 - \exp\left(-0.5 \frac{|p_L - p_R|}{p_L + p_R}\right).$$

Here the  $p_L$  and  $p_R$  are the local pressures to the left and right of the cell interface, respectively.

For the second order Gas-Kinetic BGK scheme, the gas distribution function at the cell interface (Eq. (3.75) or (3.106)) is comprised of linearly varying states:

$$\begin{aligned} f|_{x=x_{ci}} = & [1 - \exp(-t/\tau)] g_0 \quad (3.123) \\ & + \{\tau [-1 + \exp(-t/\tau)]\} \{\bar{a}_L H(u_x) + \bar{a}_R [1 - H(u_x)]\} u_x g_0 \\ & + \tau [t/\tau - 1 + \exp(-t/\tau)] \bar{A} g_0 \\ & + \exp(-t/\tau) \{(1 - a_L u_x t) H(u_x) g_L + (1 - a_R u_x t) [1 - H(u_x)] g_R\}. \end{aligned}$$

The first term in Eq. (3.123) is again similar to the Lax-Wendroff type Euler fluxes mentioned above. The second term, actually the spatial slopes of the equilibrium state at the cell interface, represents the viscous fluxes and accounts for the physical viscosity and heat conductivity effects. The third term

contributes to both the time evolution and the viscous term. The fourth term is the dissipative term and the spatial slopes of the equilibrium states to the left and right of the cell interface cause additional dissipation. Although the second order Gas-Kinetic BGK scheme actually results in the Navier-Stokes solutions, it could also be employed for the Euler solutions. The only difference is the use of the collision time. For the Euler solutions, the collision time given in Eq. (3.56) could be used while the collision time is chosen according to the physical viscosity coefficient for the Navier-Stokes solutions:

$$\tau = \frac{\mu}{p} + \frac{|\rho_L/\lambda_L - \rho_R/\lambda_R|}{(\rho_L/\lambda_L + \rho_R/\lambda_R)} \Delta t \quad (3.124)$$

Here the second term controls the numerical viscosity and necessary in the under-resolved flow regions. On the other hand, much simplified versions could also be obtained for both Euler and Navier-Stokes solutions in order to reduce the computation time. For example, the Gas-Kinetic BGK scheme can be simplified as

$$f = g_0(1 + \bar{A}t) + \epsilon(f_0 - g_0) \quad (3.125)$$

for Euler solutions and

$$f = g_0\{1 + \bar{A}(t - \tau) - \tau u_x(\bar{a}_L H(u_x) + \bar{a}_R [1 - H(u_x)])\} + \epsilon(f_0 - g_0) \quad (3.126)$$

for the Navier-Stokes solutions by deleting the corresponding slopes terms. Here  $f_0$  is the same as in Eq. (3.73) or (3.104). In the present study, Eqs. (3.125) and (3.126) are utilized for the Euler and Navier-Stokes solutions, respectively.

### 3.2.2 Temporal Discretization

The finite volume temporal discretization is performed based on Eq. (3.58) after the numerical fluxes are evaluated:

$$\frac{d\mathbf{Q}}{dt} = -\frac{1}{\Omega_e} \mathbf{R}_e. \quad (3.127)$$

Here the total numerical flux at the control volume is called as the residual.

From Eq. (3.127), a basic explicit scheme can be derived

$$\Delta\mathbf{Q}^n = -\frac{\Delta t}{\Omega_e} \mathbf{R}_e^n \quad (3.128)$$

where

$$\Delta\mathbf{Q}^n = \mathbf{Q}^{n+1} - \mathbf{Q}^n.$$

In the present study, an explicit three-stage Runge-Kutta time-stepping scheme is employed, the details of which is given in the following section.

#### 3.2.2.1 Explicit Three-Stage Runge-Kutta Time-Stepping Scheme

The concept of explicit multistage schemes was first presented by Jameson *et al.* [57]. The multistage scheme advances the solution in a number of steps so-called stages. Based on Eq. (3.127), three-stage Runge-Kutta time-stepping scheme is given by

$$\mathbf{Q}^{(0)} = \mathbf{Q}^{(n)}, \quad (3.129)$$

$$\mathbf{Q}^{(1)} = \mathbf{Q}^{(0)} - \alpha_1 \frac{\Delta t}{\Omega_e} \mathbf{R}_e^{(0)}, \quad (3.130)$$

$$\mathbf{Q}^{(2)} = \mathbf{Q}^{(0)} - \alpha_2 \frac{\Delta t}{\Omega_e} \mathbf{R}_e^{(1)}, \quad (3.131)$$

$$\mathbf{Q}^{(n+1)} = \mathbf{Q}^{(0)} - \alpha_3 \frac{\Delta t}{\Omega_e} \mathbf{R}_e^{(2)}, \quad (3.132)$$

where  $\alpha_k$  are the stage coefficients with

$$\alpha_1 = \frac{1}{3}, \quad \alpha_2 = \frac{1}{2}, \quad \alpha_3 = 1,$$

$\Delta t$  is the local time step calculated in each control volume and  $\mathbf{R}_e^{(k)}$  are the residuals evaluated with the solution  $\mathbf{Q}^{(k)}$  of the  $k$ th stage. The local time-stepping is used in steady-state solutions to accelerate the convergence.

### 3.3 Boundary Conditions

In the inviscid and viscous flow computations, flow tangency, no-slip wall, farfield and symmetry boundary conditions are employed. The boundary conditions are implemented through the use of ghost cells, which are the imaginary cells neighboring the actual boundary cells. In the flux evaluations at the boundaries, these ghost cells define the proper flow properties at the *right state*,  $(R)$ .

#### 3.3.1 Wall Boundary Condition

The inviscid wall boundary condition imposes the flow tangency at the wall boundary. The normal momentum density of the ghost cell is assigned to the negative of that of the computational cell adjacent to the boundary. The normal velocity component at the wall is effectively set to zero. The remaining momentum densities as well as the mass and energy densities at the ghost cell are set to those of the corresponding interior cell so as to ensure that no mass or energy transfer exist through the wall.

The viscous wall boundary condition imposes a no-slip condition and a zero pressure gradient at the wall. Therefore, all the momentum densities of the ghost cell is assigned to the negative of those of the computational cell adjacent to the boundary. The mass and energy densities of the ghost cell are set to those of the corresponding interior cell.

### 3.3.2 Farfield Boundary Condition

Characteristic boundary conditions are applied at the farfield boundaries using fixed and extrapolated Riemann invariants. The Riemann invariants correspond to the incoming and outgoing waves traveling in the characteristic directions, which are defined normal to the boundary [58, 59]. The two locally one-dimensional Riemann invariants are given by

$$R^{\pm} = U \pm \frac{2a}{\gamma - 1} \quad (3.133)$$

where  $R^-$  is the incoming Riemann invariant determined from the freestream conditions,  $R^+$  is the outgoing Riemann invariant extrapolated from the interior flow conditions,  $U$  and  $a$  are the corresponding velocity and speed of sound, all normal to the boundary. Using the local Mach number and characteristic directions, the farfield boundary can be decided to be a subsonic inflow, subsonic outflow, supersonic inflow or supersonic outflow. The boundary conditions are then determined using the Riemann invariants, entropy condition and the equation of state.

### 3.3.3 Symmetry Boundary Condition

The symmetry boundary condition is the same as the inviscid wall boundary condition. It is simply a reflecting boundary condition. The flow tangency at the symmetry boundary is enforced by setting the normal component of the flow velocity to zero.

## 3.4 Parallel Processing Methodology

The parallel processing methodology utilized in the present study is based on domain decomposition. The unstructured/hybrid grid is partitioned using METIS software package. For unstructured grids, METIS partitions the computational domain automatically. On the other hand, a *graph file* is necessary for the hybrid grids, which is actually the neighbor connectivity of the control volume cells. A sample hybrid grid and the corresponding graph is given in Fig. 3.10. The numbers written in the grid elements denote the cell indices. The

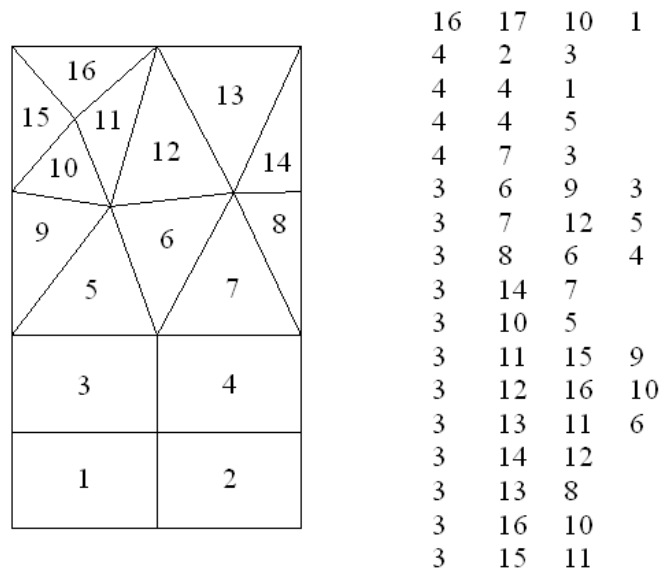


**Figure 3.10:** Sample hybrid grid in 2-D and the corresponding graph.

first line in the graph represents the *total number of cells*, *total number of nodes*, *weighting option* and *number of weights*, respectively. The remaining lines show the *number of edges* and the *cell indices of the neighbors* of the corresponding cell. For example, the *sixth line* says that the *fifth cell* has 3 edges and the cell indices of its neighbors are 6, 9 and 3. The partitioning of the graph is performed using *kmetis* program. During the partitioning, each cell is weighted by its number of edges so that each partition has about the same number of total edges to improve the load balancing in parallel computations.

*Parallel Virtual Machine* (PVM) message-passing library routines are employed in a *master-worker* algorithm. The *master* process performs all the input-output, starts up PVM, spawns worker processes and sends the initial data to the workers. The *worker* processes first receive the initial data, apply the interface and the flow boundary conditions, and solve the flowfield within the partition. The flow variables at the interface boundaries are exchanged among the neighboring partitions at each time step for the implementation of inter-partition boundary conditions.

## CHAPTER 4

### RESULTS AND DISCUSSION

In this chapter, the gas-kinetic methods developed are applied to various flow problems ranging from subsonic to supersonic, inviscid to viscous in 1-D, 2-D and 3-D. The inviscid flows solutions are obtained on unstructured grids while hybrid grids are used in viscous flow computations. The results are discussed in terms of accuracy, robustness and parallel efficiency.

#### 4.1 1-D Shock-Tube Problems

In this section, preliminary results obtained from the gas-kinetic methods in 1-D are presented. Three different shock-tube problems, which are well-known in the literature, are solved with gas-kinetic methods and they are compared to the exact solutions as well as the results of the classical methods. In all computations 400 grid cells are employed.



### 4.1.1 Case 1: Sod Shock-Tube Problem

This case is first considered by Sod [60]. The initial conditions for this case are given in Table 4.1. The  $L$  and  $R$  indices in Table 4.1 show the *left* and *right* states. The length of the tube is 2 unit and  $x$  varies from  $-1$  to  $+1$ . The gas is separated at  $x = 0$ .

**Table 4.1:** Initial conditions for Case 1.

$\rho_L$	$U_L$	$p_L$	$\rho_R$	$U_R$	$p_R$
1.0	0.0	1.0	0.125	0.0	0.1

Figures 4.1, 4.2 and 4.3 present comparisons of the results of the first order accurate Kinetic Flux Vector Splitting and the Gas-Kinetic BGK schemes with the exact solution as well as the results of the classical schemes in terms of den-

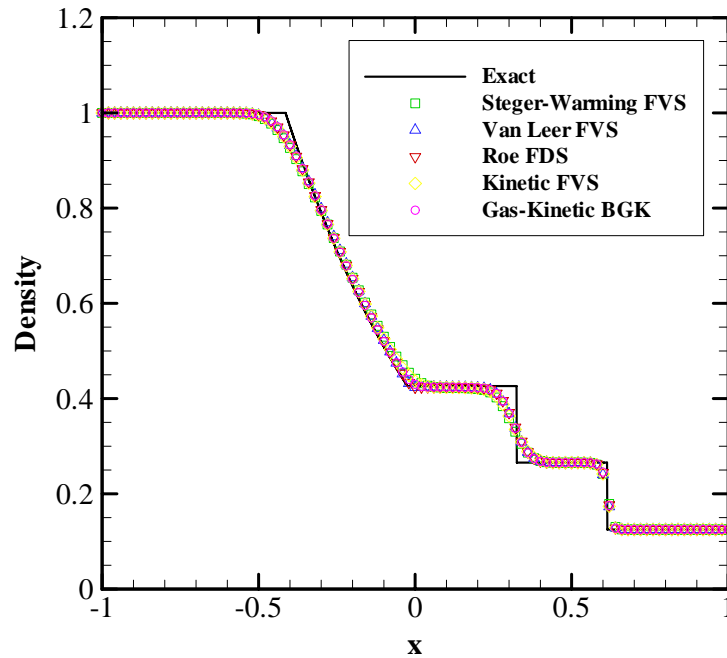


**Figure 4.1:** Density distribution for Case 1 (First order results).

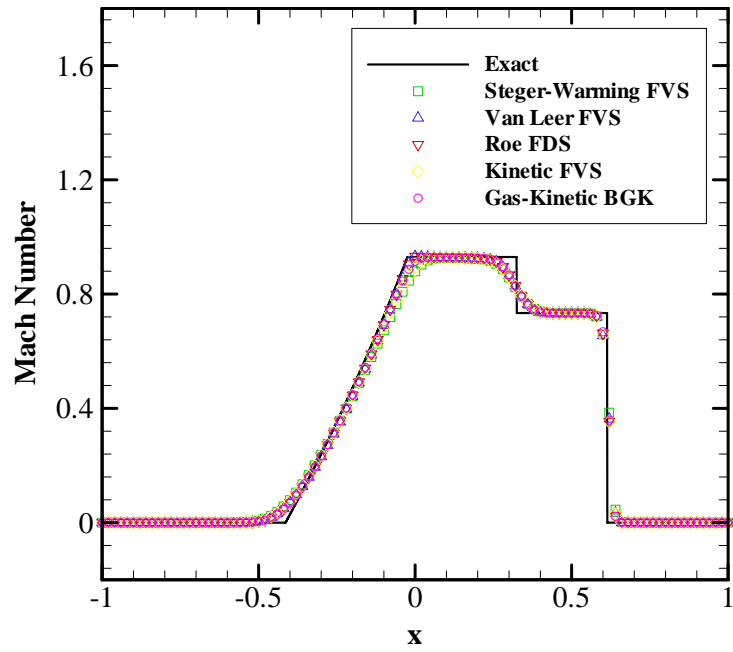


Figure 4.2: Mach number distribution for Case 1 (First order results).

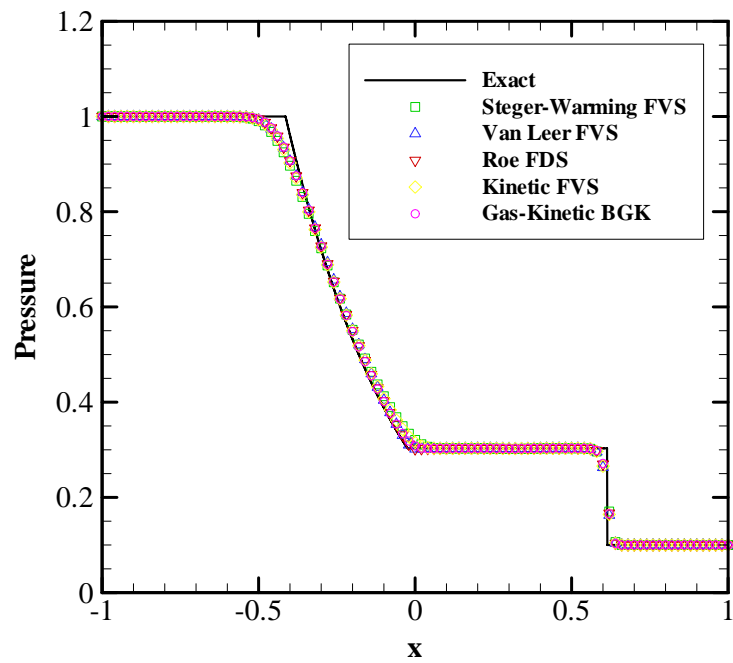
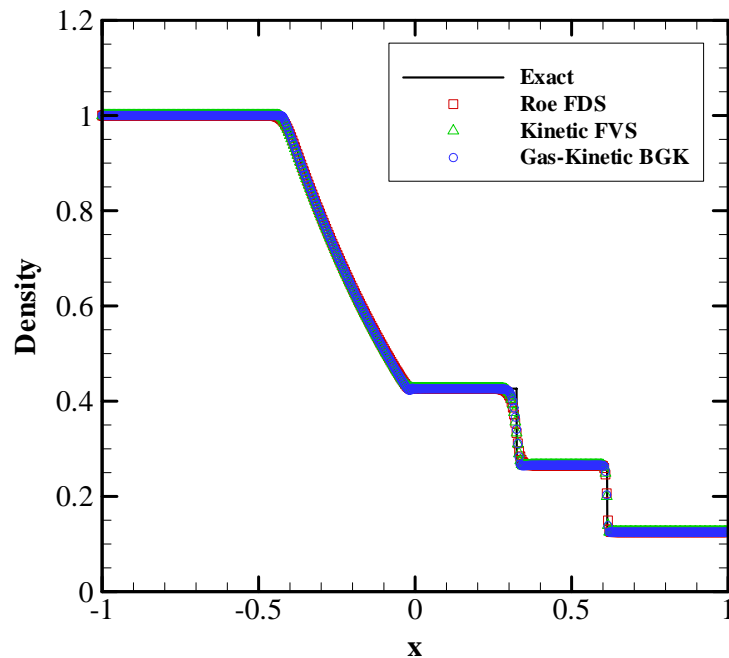


Figure 4.3: Pressure distribution for Case 1 (First order results).

sity, Mach number and pressure at  $t = 0.35$ . The results obtained from the classical flux vector splitting schemes (Steger-Warming, Van-Leer FVS) seem slightly more dissipative than those of Roe's flux difference splitting and the Gas-Kinetic BGK schemes. It is attributed to the fact that the classical flux vector splitting schemes give accurate results especially in smooth regions. Due to the underlying principles explained in Chapter 2, the Kinetic Flux Vector Splitting scheme gives similar results as the classical flux vector splitting schemes. The results obtained from the Gas-Kinetic BGK scheme are more accurate than those of the flux vector splitting schemes and nearly the same with the Roe's flux difference splitting scheme. This is not surprising since the Gas-Kinetic BGK scheme has an advanced gas evolution model, which is based on particle collisions. The comparisons of the second order accurate results with the



**Figure 4.4:** Density distribution for Case 1 (Second order results).

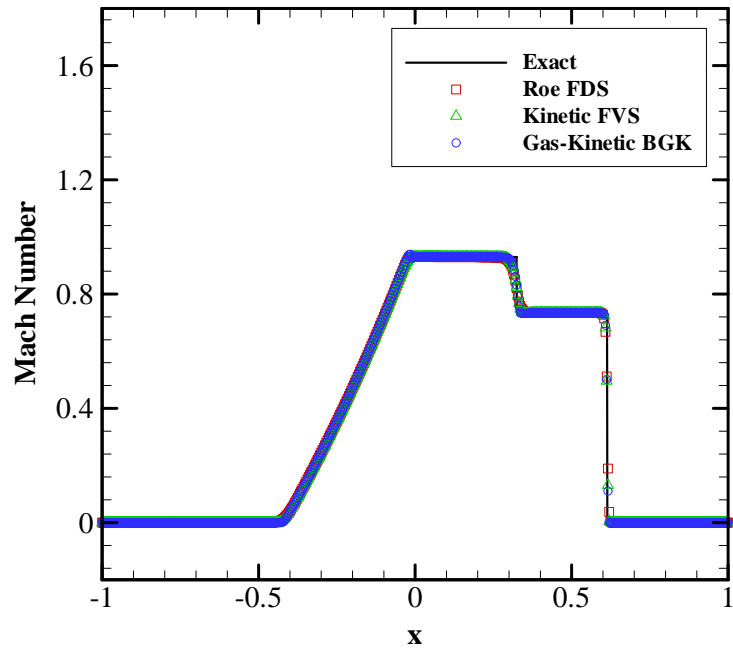


Figure 4.5: Mach number distribution for Case 1 (Second order results).

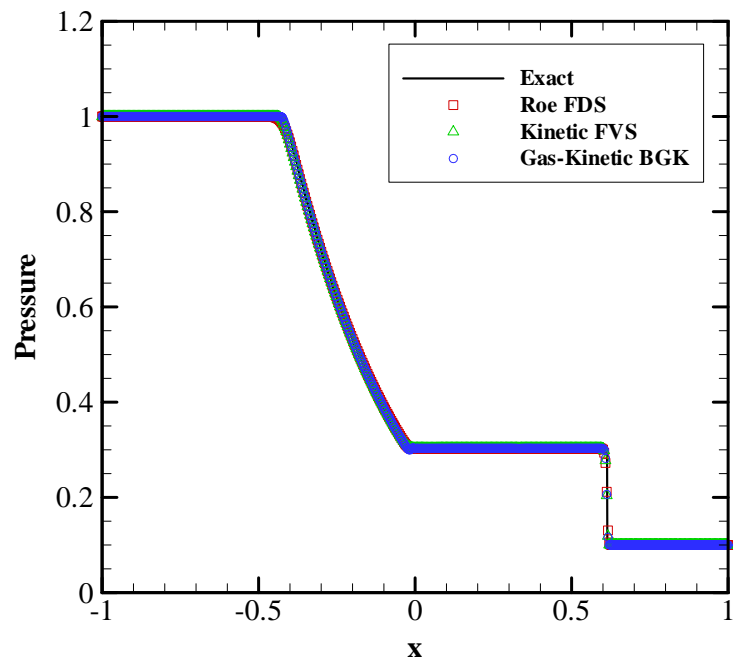


Figure 4.6: Pressure distribution for Case 1 (Second order results).

exact solution are given in Figs. 4.4, 4.5 and 4.6. All the second order accurate results are based on the MUSCL approach and min-mod limiter is utilized. Since Roe's flux difference splitting scheme is shown to be more successful than other classical schemes in the first order accurate results, only this scheme is used in the comparisons. The results of all the schemes exhibit obvious improvement over first order accurate results although the results of the Gas-Kinetic BGK and Roe scheme is slightly better than those of the Kinetic Flux Vector Splitting scheme.

#### 4.1.2 Case 2: Arora-Roe Shock-Tube Problem

This case is first utilized by Arora and Roe [61]. It is an interesting case that reveals the weaknesses of the classical schemes. The initial conditions for this case are given in Table 4.2. The  $L$  and  $R$  indices in Table 4.2 show the *left* and *right* states. The length of the tube is again 2 unit and  $x$  varies from  $-1$  to  $+1$ . The gas is separated at  $x = 0$ .

**Table 4.2:** Initial conditions for Case 2.

$\rho_L$	$U_L$	$p_L$	$\rho_R$	$U_R$	$p_R$
3.857	0.92	10.333	1.0	3.55	1.0

Figures 4.7, 4.8 and 4.9 present comparisons of the results of the first order accurate Kinetic Flux Vector Splitting and the Gas-Kinetic BGK schemes with the exact solution as well as the results of the classical schemes in terms of density, Mach number and pressure at  $t = 0.09$ . Roe's flux difference splitting scheme gives wrong solution for this case. This is due to the fact that Roe

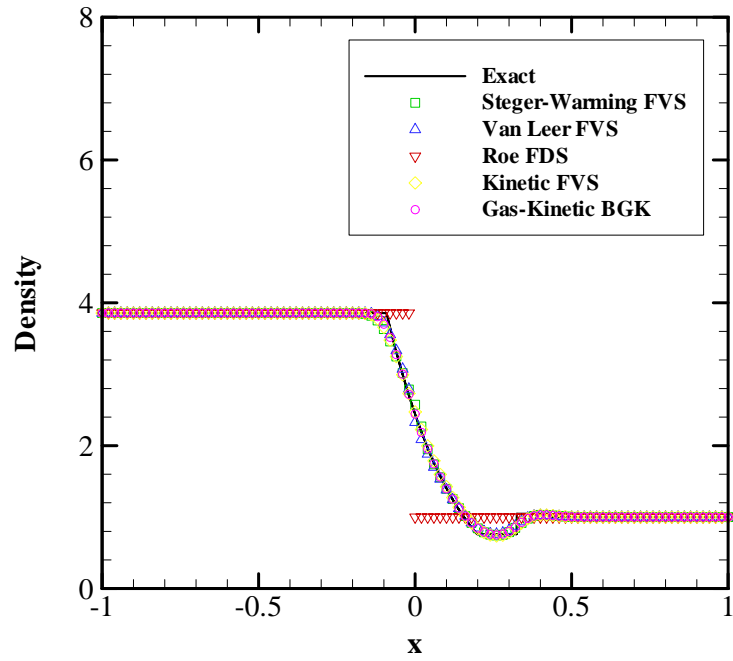


Figure 4.7: Density distribution for Case 2 (First order results).

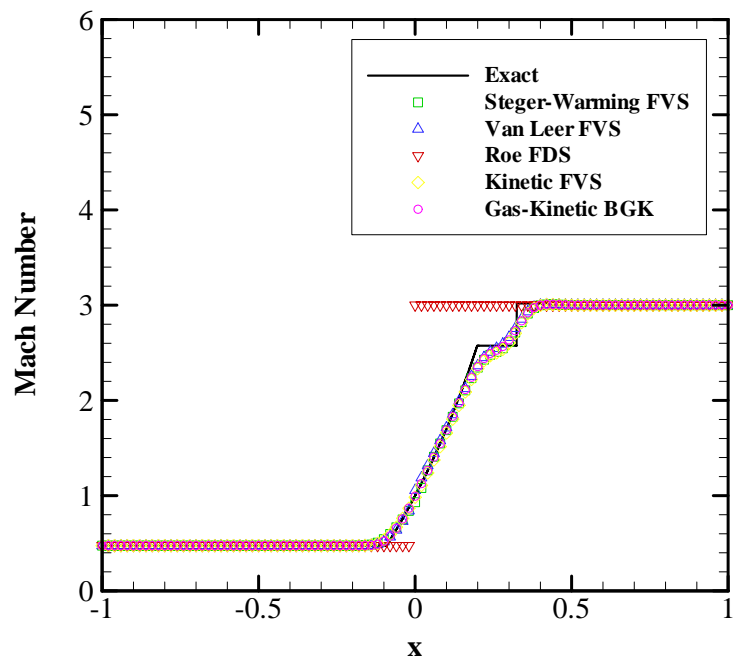
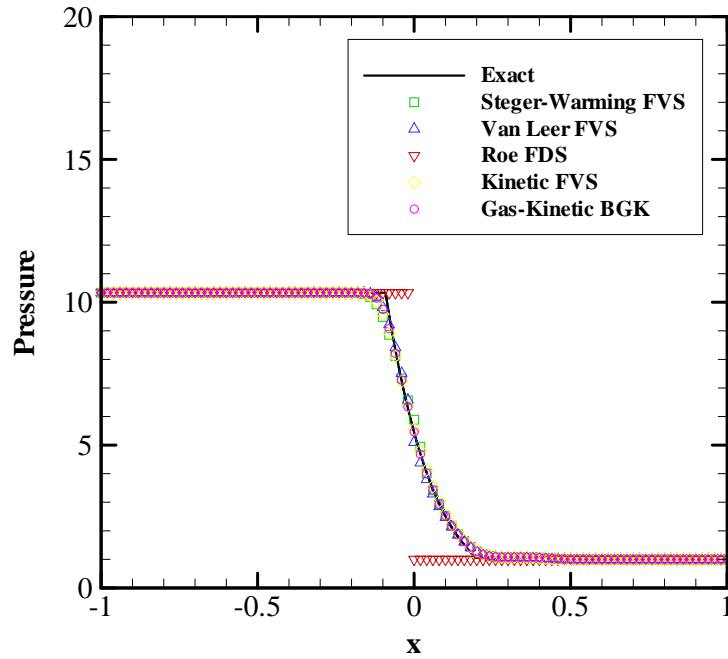


Figure 4.8: Mach number distribution for Case 2 (First order results).



**Figure 4.9:** Pressure distribution for Case 2 (First order results).

scheme does not catch the sonic rarefactions and that results in negative entropy near the sonic region. This problem can be corrected with an entropy fix to the scheme, but this fix has no physical meaning. The classical flux vector splitting schemes have also some problems in this region. On the other hand, the gas-kinetic theory based schemes have no problem near the sonic region. The comparisons of the second order accurate results with the exact solution are given in Figs. 4.10, 4.11 and 4.12. All the second order accurate results are based on the MUSCL approach and min-mod limiter is utilized. Again, only Roe's flux difference splitting scheme is considered. The problem of the Roe scheme near the sonic region is disappeared with the second order accurate formulation. On the other hand, it is interesting to note that the results of the Roe scheme near the discontinuities are not so good as the gas-kinetic schemes.

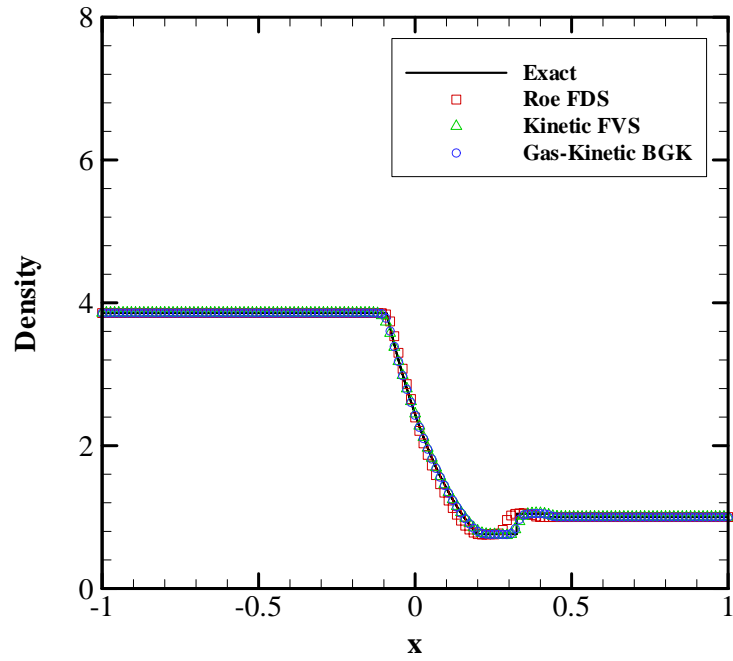


Figure 4.10: Density distribution for Case 2 (Second order results).

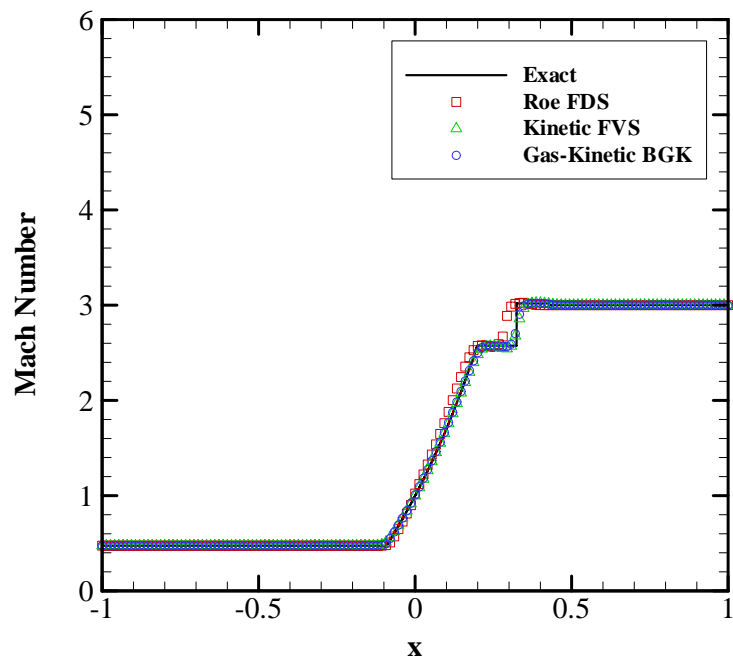
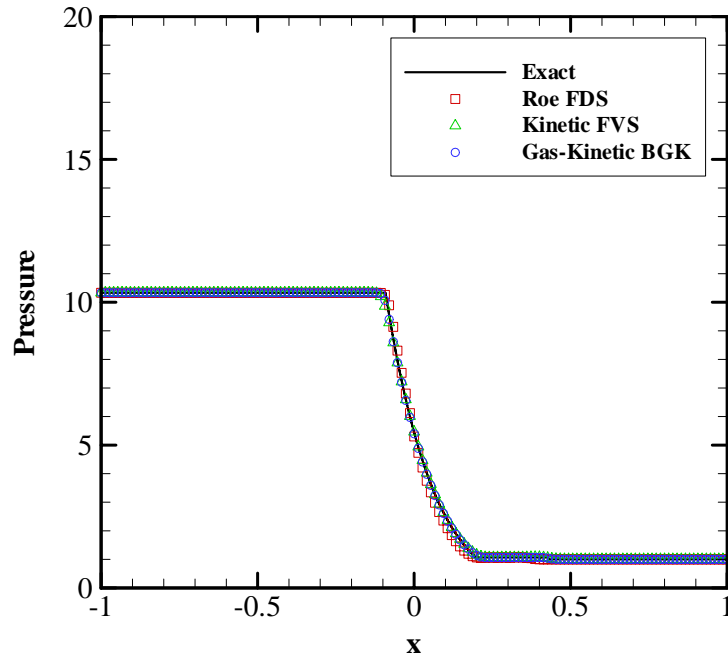


Figure 4.11: Mach number distribution for Case 2 (Second order results).





**Figure 4.12:** Pressure distribution for Case 2 (Second order results).

For this case, the most accurate results are obtained from the Gas-Kinetic BGK scheme.

### 4.1.3 Case 3: Woodward-Colella Shock-Tube Problem

This case is first tested by Woodward and Colella [62]. It is a difficult case with three different initial states, which are given in Table 4.3. The  $L$ ,  $M$  and  $R$  indices in Table 4.3 show the *left*, *middle* and *right* states, respectively. The length of the tube is 2 unit and  $x$  varies from  $-1$  to  $+1$ . The gas is separated at  $x = -0.8$  and  $x = 0.8$ .

**Table 4.3:** Initial conditions for Case 3.

$\rho_L$	$U_L$	$p_L$	$\rho_M$	$U_M$	$p_M$	$\rho_R$	$U_R$	$p_R$
1.0	0.0	1000.0	1.0	0.0	0.01	1.0	0.0	100.0

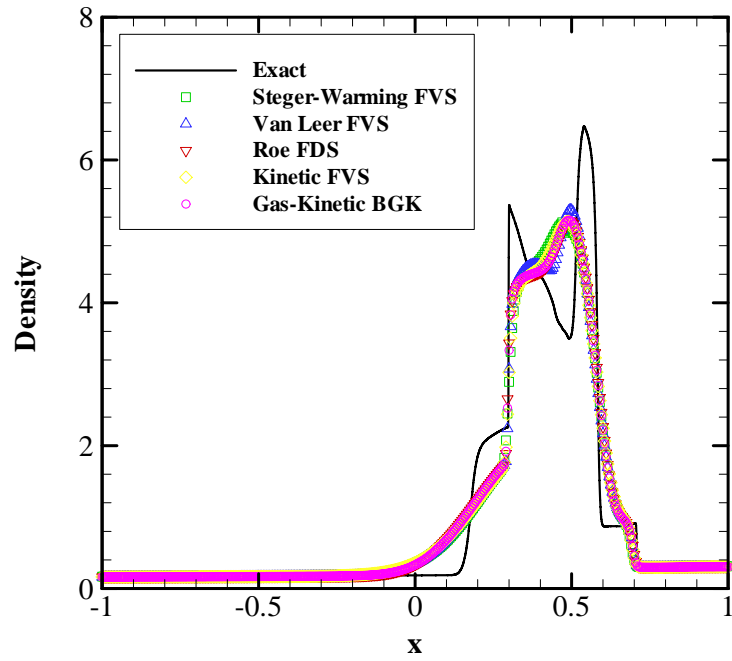


Figure 4.13: Density distribution for Case 3 (First order results).

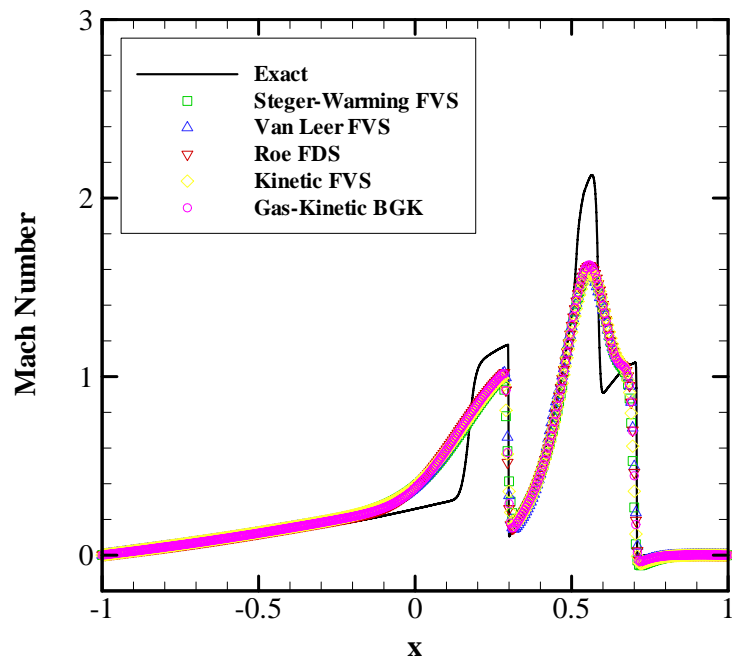
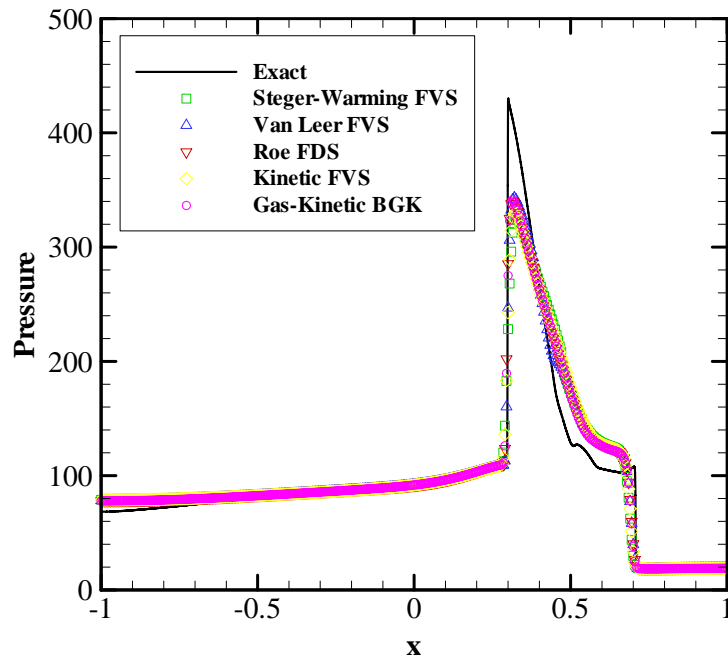


Figure 4.14: Mach number distribution for Case 3 (First order results).



**Figure 4.15:** Pressure distribution for Case 3 (First order results).

Figures 4.13, 4.14 and 4.15 present comparisons of the results of the first order accurate Kinetic Flux Vector Splitting and the Gas-Kinetic BGK schemes with the exact solution as well as the results of the classical schemes in terms of density, Mach number and pressure at  $t = 0.075$ . All of the first order accurate results are far from matching the exact solution for this difficult case. Roe's flux difference splitting and Gas-Kinetic BGK schemes seem to be slightly more accurate than others. The comparisons of the second order accurate results with the exact solution are given in Figs. 4.16, 4.17 and 4.18. All the second order accurate results are based on the MUSCL approach and min-mod limiter is used. The results obtained from the Gas-Kinetic BGK scheme are the most accurate one among others and the Kinetic Flux Vector Splitting scheme gives again dissipative results.

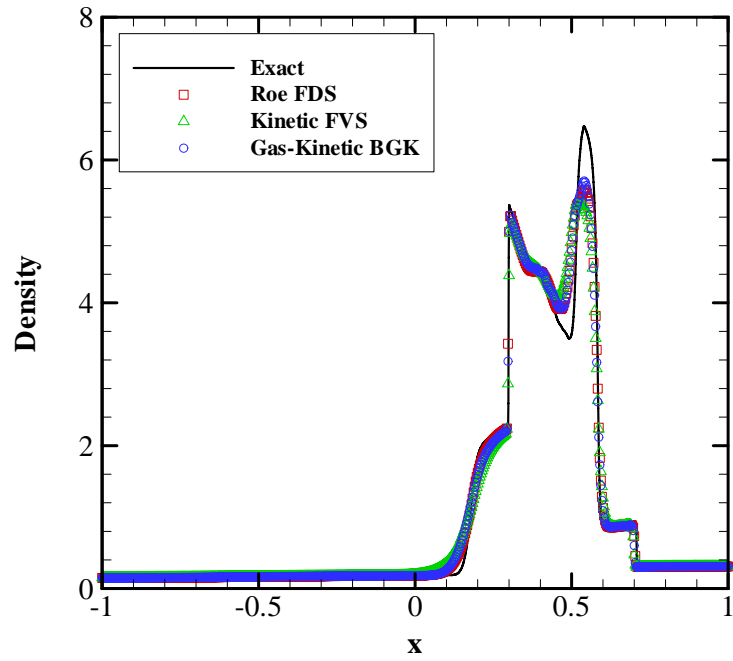


Figure 4.16: Density distribution for Case 3 (Second order results).

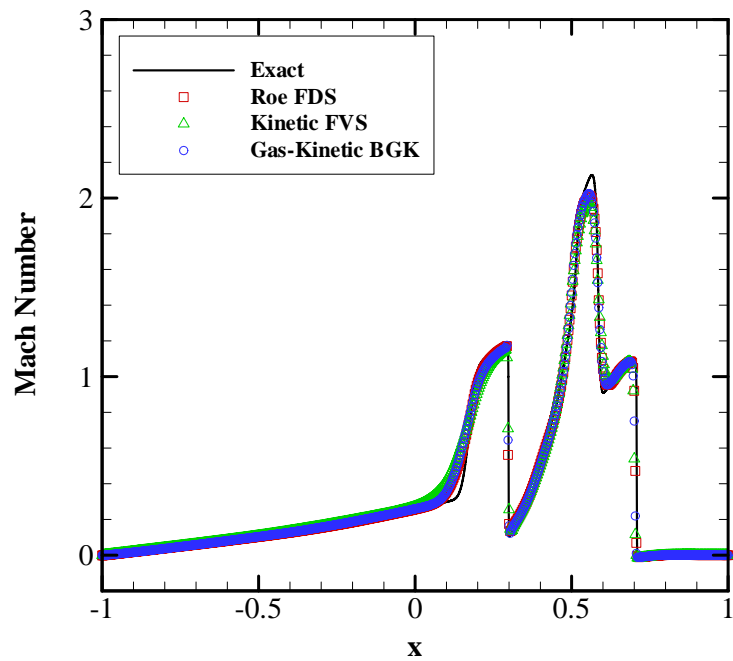


Figure 4.17: Mach number distribution for Case 3 (Second order results).

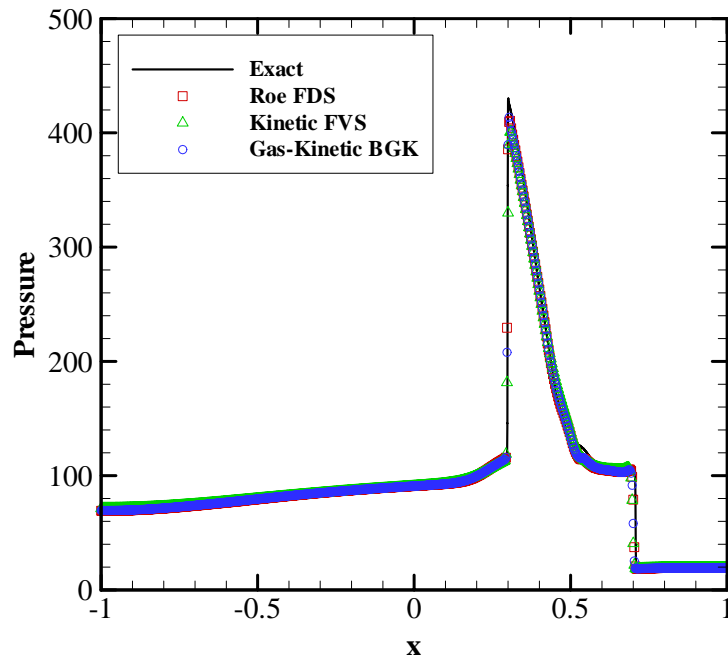


Figure 4.18: Pressure distribution for Case 3 (Second order results).

#### 4.1.4 Summary

The preliminary study in 1-D indicates that the results obtained from gas-kinetic theory based methods are comparable with those of classical methods. The gas-kinetic methods do not give unphysical results nor need any special treatment in certain problems as their classical counterparts. The Kinetic Flux Vector Splitting scheme show similar behavior as the classical flux vector splitting schemes. The Gas-Kinetic BGK scheme gives accurate results due to its underlying theory based on particle collisions.

## 4.2 2-D Flows

In this section, 2-D flow solutions based on the Gas-Kinetic BGK scheme are presented. Various inviscid and viscous test cases are considered to show the accuracy and robustness of the methodology. The solutions are obtained in parallel, which significantly improves the computation time, a significant deficiency of the gas-kinetic methods. The results are compared to those of classical schemes as well as available experimental data.

### 4.2.1 Case 1: Inviscid Flow Over a Transonic Airfoil

RAE 2822 transonic airfoil, which has available experimental data [63], is selected as a first test case. The freestream conditions and the computational mesh with partitions for this case are given in Table 4.4 and Fig. 4.19, respectively. These conditions actually correspond to a chordwise Reynolds number of 6.5 million. The computational mesh consists of 7652 nodes and 14872 cells.

**Table 4.4:** Freestream conditions for Case 1.

Mach Number	Angle of Attack, <i>deg</i>	Pressure, <i>Pa</i>	Temperature, <i>K</i>
0.729	2.31	101325	288

Figures 4.20, 4.21, 4.22 and 4.23, 4.24, 4.25 show the Mach and entropy contours for the Kinetic Flux Vector Splitting, the Gas-Kinetic BGK, Roe's flux difference splitting schemes, respectively. The Gas-Kinetic BGK and Roe schemes give very similar results and they clearly capture the shock wave generated on the upper surface of the airfoil. In addition, the entropy generation levels behind

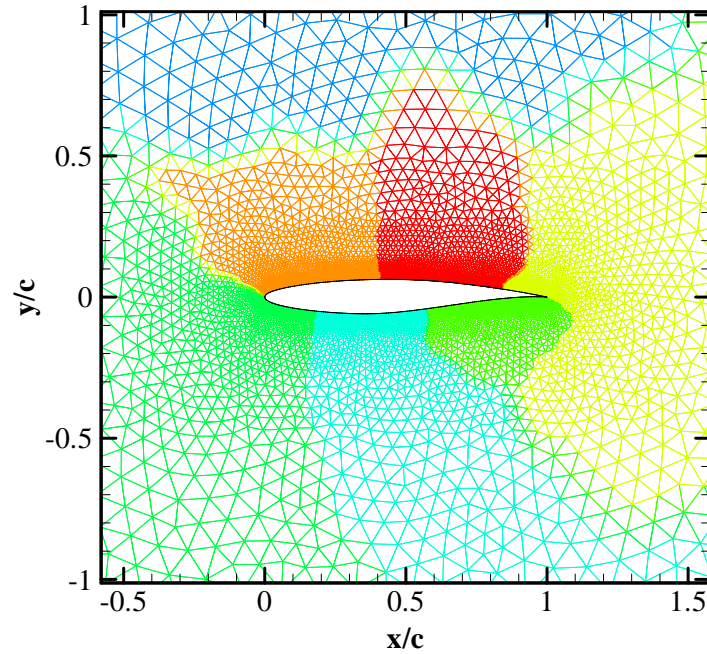


**Figure 4.19:** Computational mesh with partitions for Case 1 (Zoomed view).

the shock wave and entropy distributions predicted by the two schemes agree quite well. On the other hand, due to the dissipative nature common in flux vector splitting schemes, the Kinetic Flux Vector Splitting scheme smears out this shock wave. Moreover, it appears that the numerical entropy generation is significantly higher than those of the Gas-Kinetic BGK and Roe schemes. In Figs. 4.26, 4.27 and 4.28, the comparisons of pressure coefficient obtained from the Kinetic Flux Vector Splitting, the Gas-Kinetic BGK and Roe schemes with the experimental data are given. The results of Gas-Kinetic BGK and Roe schemes are generally in good agreement with the experimental data. The shock wave on the upper surface is well-captured; however, the shock location is overpredicted in comparison to the experimental data and the pressure is underpredicted at the trailing edge. These disagreements are attributed to

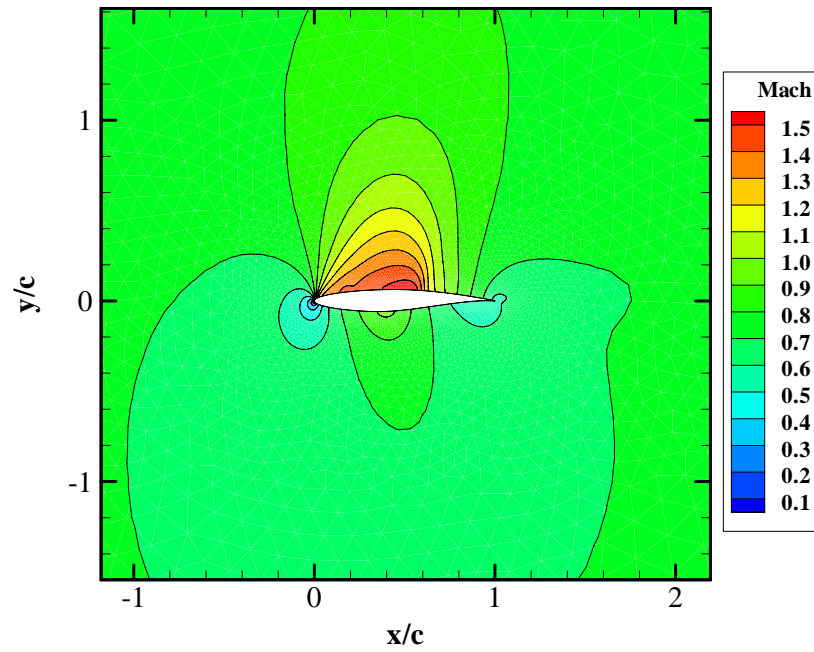


Figure 4.20: Mach number contours for Case 1 (Kinetic FVS scheme).

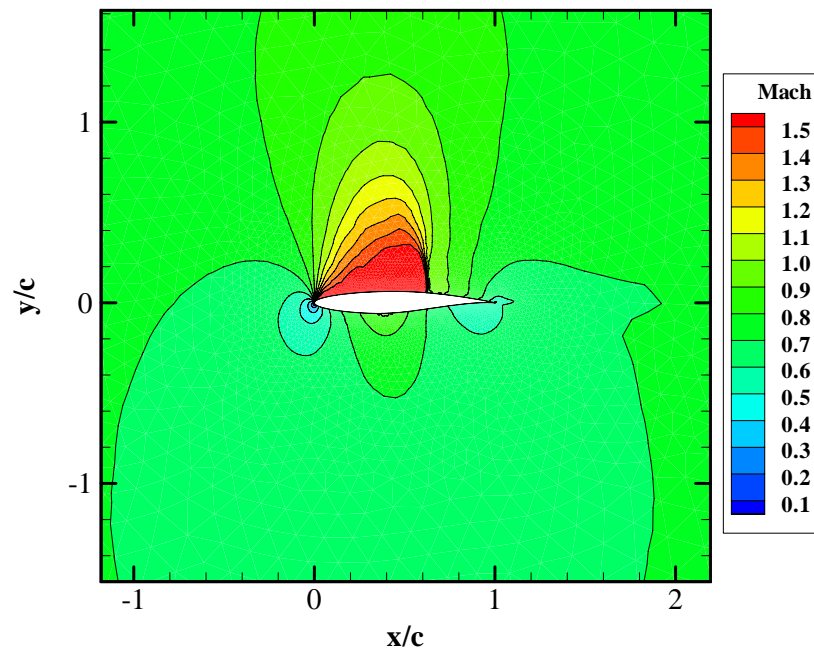


Figure 4.21: Mach number contours for Case 1 (Gas-Kinetic BGK scheme).



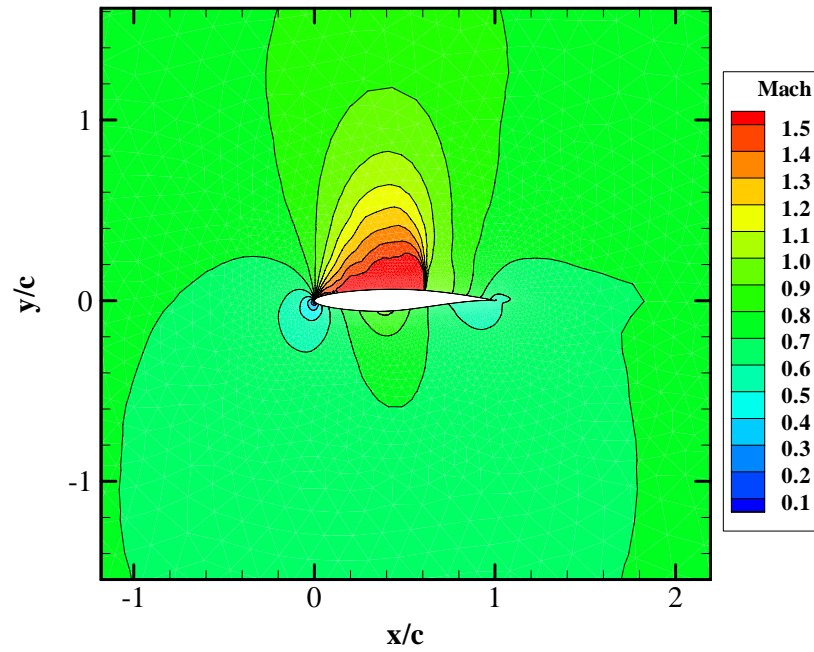


Figure 4.22: Mach number contours for Case 1 (Roe's FDS scheme).

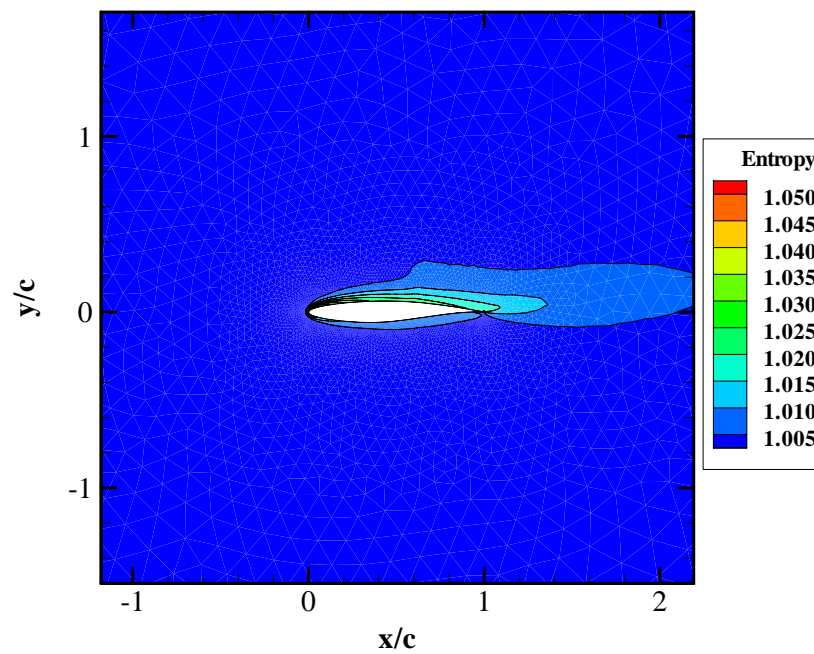


Figure 4.23: Entropy contours for Case 1 (Kinetic FVS scheme).

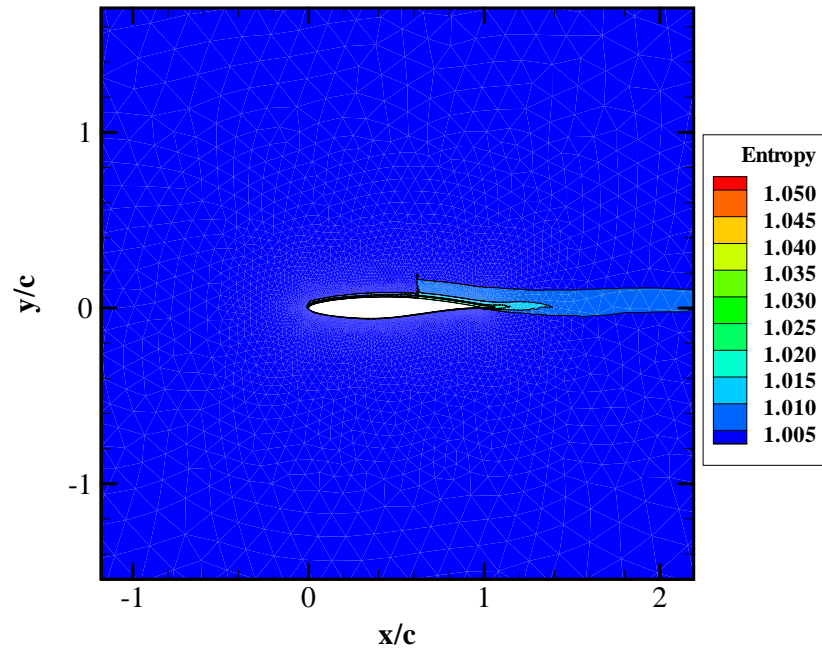


Figure 4.24: Entropy contours for Case 1 (Gas-Kinetic BGK scheme).

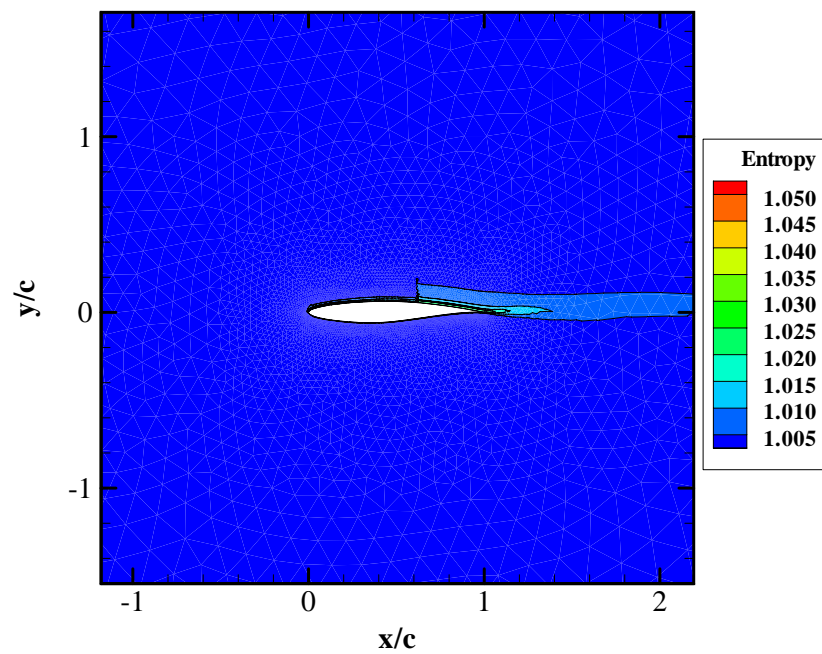
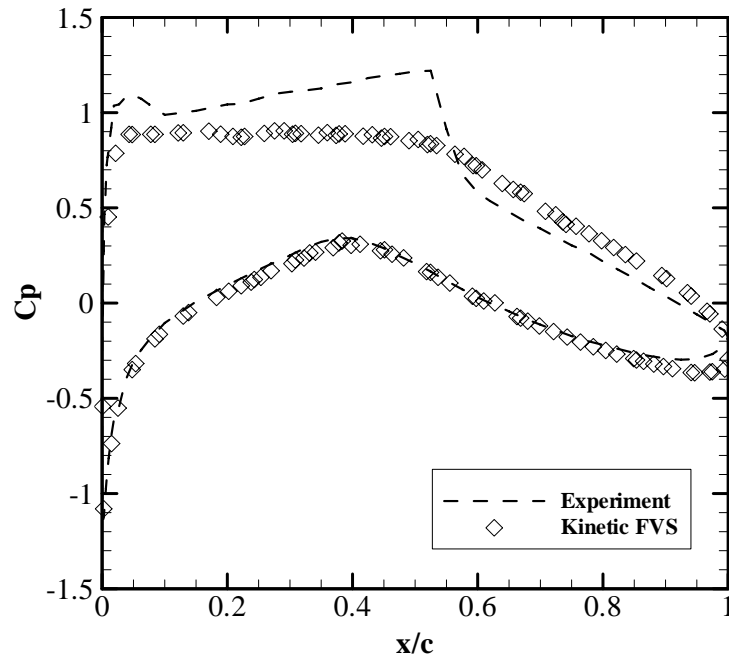


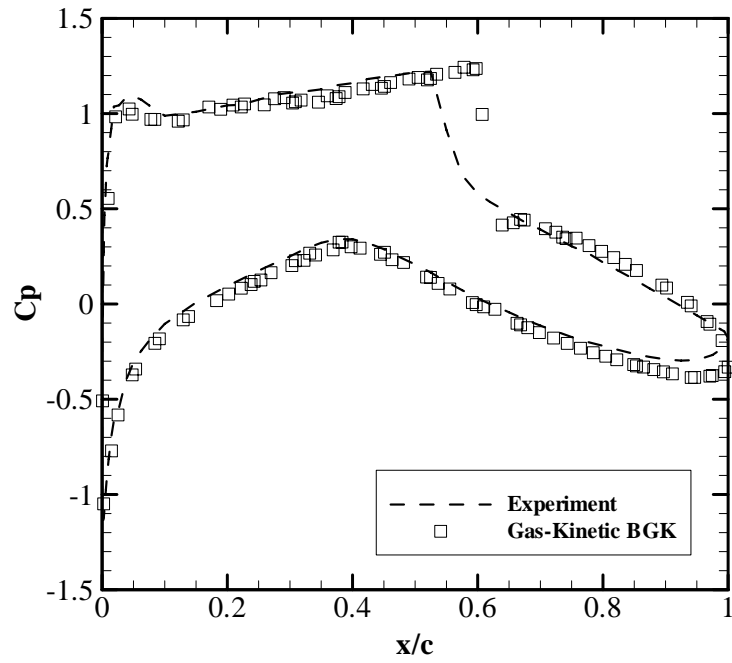
Figure 4.25: Entropy contours for Case 1 (Roe's FDS scheme).

the viscous effects which are absent in the present inviscid flow computations. The Kinetic Flux Vector Splitting scheme smears out the shock wave and underpredicts the suction pressure on the upper surface.

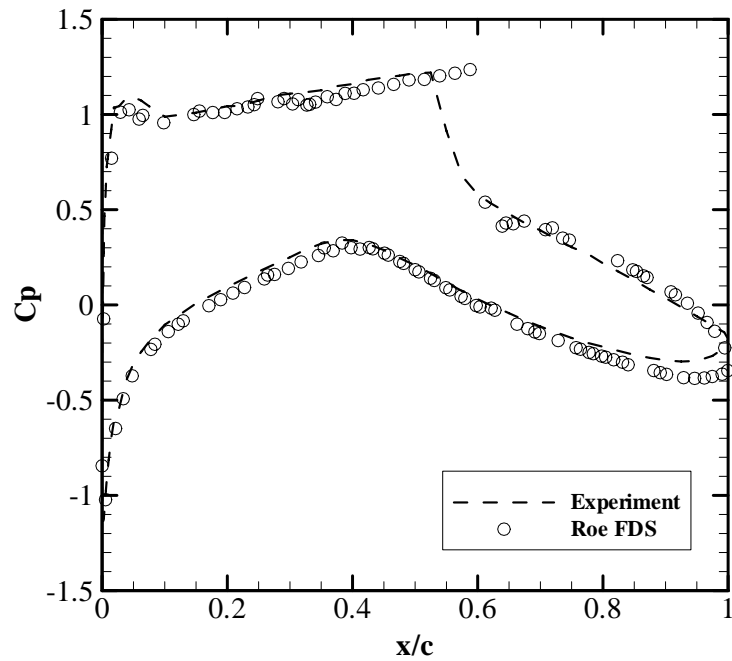
Numerical entropy generation of the Gas-Kinetic BGK scheme is also assessed in a low speed inviscid flow solution. The flow around the RAE 2822 airfoil is now computed at a Mach number of 0.3 and the entropy distributions computed by both the Gas-Kinetic BGK and Roe scheme are given in Fig. 4.29. The contour levels are plotted with  $\Delta s = 0.001$ . As shown in the figures, the numerical entropy generation of the Gas-Kinetic BGK scheme is significantly smaller than that of the Roe scheme.



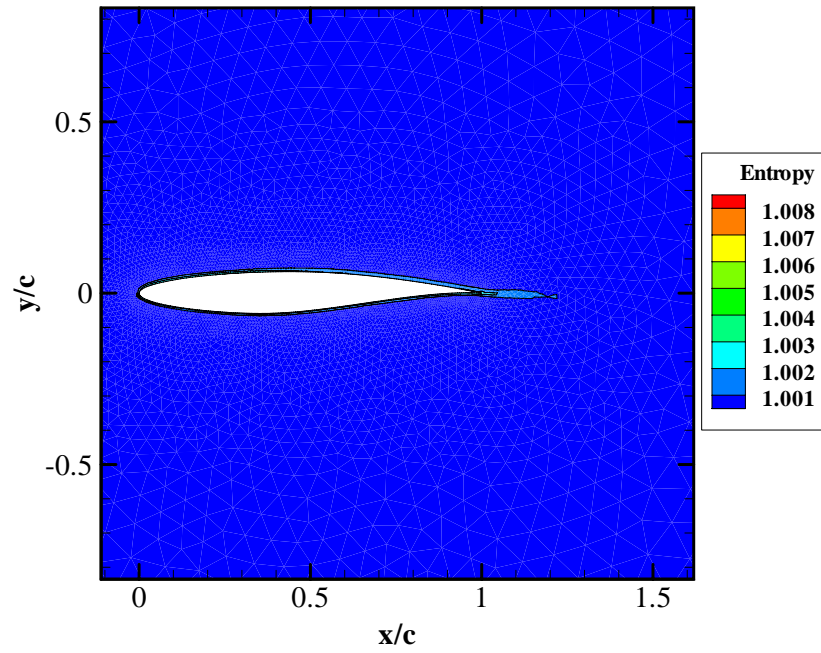
**Figure 4.26:** Pressure distribution on the airfoil surface for Case 1 (Kinetic FVS scheme, every other three data point is displayed).



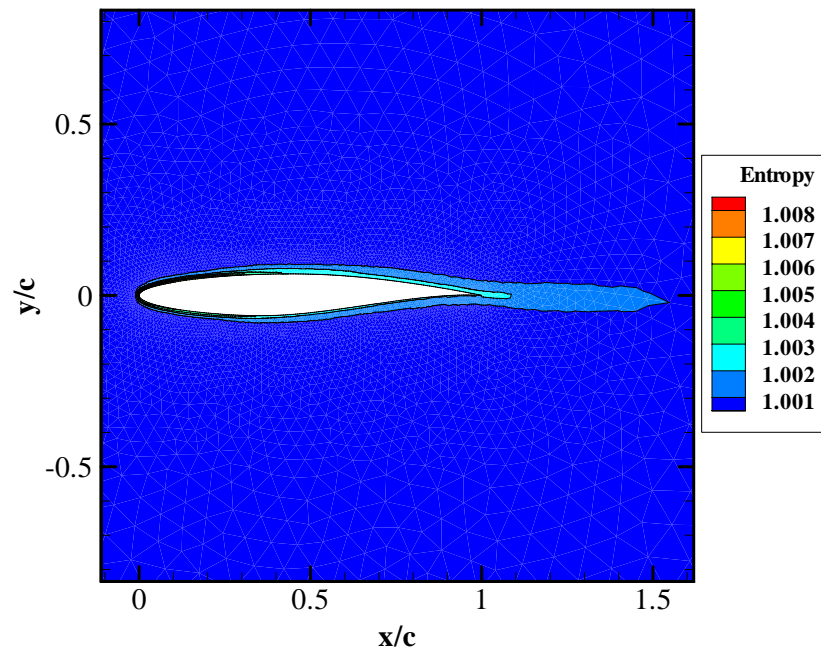
**Figure 4.27:** Pressure distribution on the airfoil surface for Case 1 (Gas-Kinetic BGK scheme, every other three data point is displayed).



**Figure 4.28:** Pressure distribution on the airfoil surface for Case 1 (Roe's FDS scheme, every other three data point is displayed).



(a) Gas-Kinetic BGK scheme



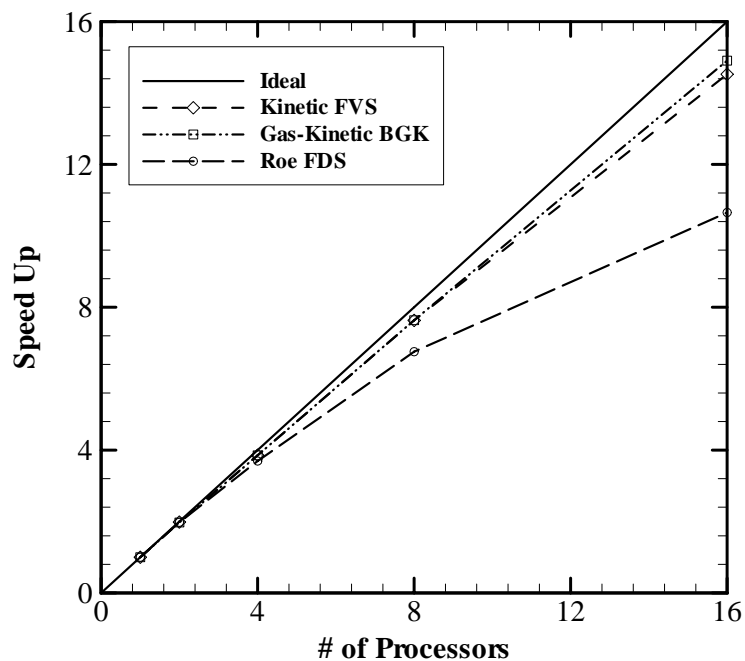
(b) Roe's FDS scheme

Figure 4.29: Entropy contours over RAE 2822 airfoil at  $M = 0.3$ .

**Table 4.5:** Parallel efficiency of computations.

Number of Nodes	Computational Efficiency, <i>sec/iter</i>		
	Kinetic FVS	Gas-Kinetic BGK	Roe's FDS
1	0.0388	0.0439	0.0308
2	0.0195	0.0222	0.0156
4	0.0101	0.0114	0.0083
8	0.0051	0.0057	0.0046
16	0.0027	0.0029	0.0029

The parallel computations are performed on an *Itanium 2* cluster running on Linux. Dual *Itanium 2* processors operate at 1.3Ghz with 3MB L2 cache and 2GB of memory for each. The parallel efficiency of the computations is given in Table 4.5 and Fig. 4.30. It is observed that the Gas-Kinetic BGK scheme is about 1.13 times computationally more expensive than the Kinetic Flux Vector Splitting scheme and about 1.42 times more expensive than Roe scheme



**Figure 4.30:** Computational speed-up for Case 1.

in serial computations. On the other hand, the high parallel efficiency of the gas-kinetic schemes is maintained as the number of processors increases as opposed to Roe scheme, which is attributed to the high computing to communication ratio in the gas-kinetic schemes. Although the gas-kinetic schemes are more expensive in serial computations, it may not be an issue in parallel computations.

Finally, the convergence histories are shown in Fig. 4.31. The Kinetic Flux Vector Splitting scheme, which is the most dissipative one, converges faster and smoother than the others. The Gas-Kinetic BGK and Roe schemes have similar convergence behavior.

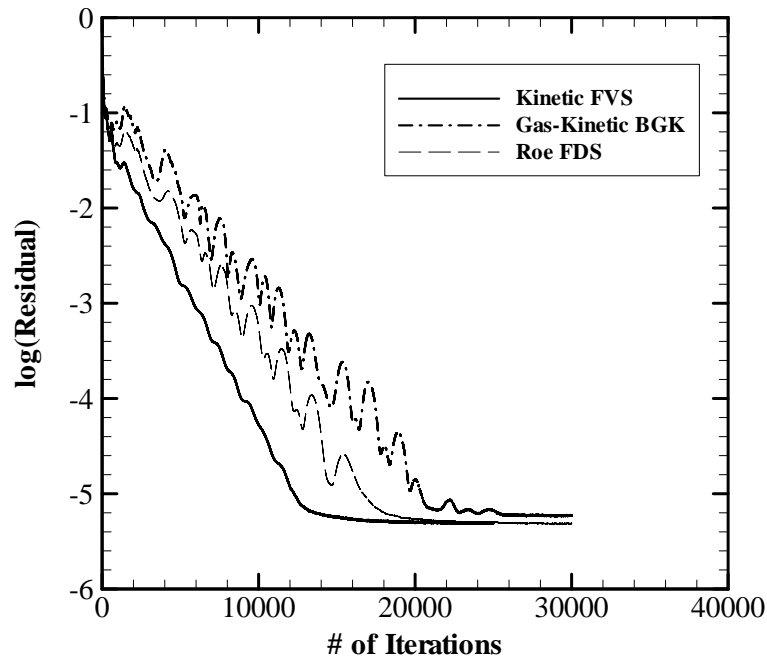


**Figure 4.31:** Convergence history for Case 1.

#### 4.2.2 Case 2: Inviscid Supersonic Flow Over a Wedge

The inviscid supersonic flow over a wedge is selected as a second test case, which is taken from [64]. This is actually a channel flow in which there is a  $15^\circ$  ramp. The freestream conditions and the computational mesh with partitions for this case are given in Table 4.6 and Fig. 4.32, respectively. The computational mesh consists of 30819 nodes and 60132 cells.

**Table 4.6:** Freestream conditions for Case 2.

Mach Number	Angle of Attack, <i>deg</i>	Pressure, <i>Pa</i>	Temperature, <i>K</i>
1.8	0.0	101325	288

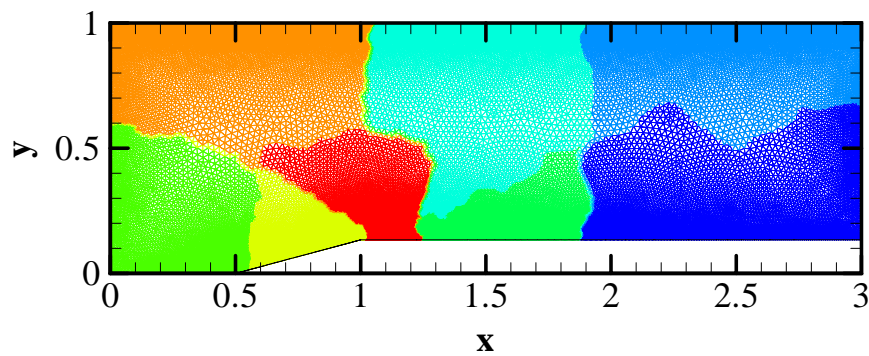


**Figure 4.32:** Computational mesh with partitions for Case 2.

Figures 4.33 and 4.34 show the Mach and pressure contours obtained from the Gas-Kinetic BGK scheme, respectively. It can be clearly seen that there is an attached shock at the compression corner of the ramp, which is reflected from the top wall forming a Mach stem. The shock wave continues to reflect from the bottom and top walls before exiting the channel. The expansion fan at the expansion corner of the ramp weakens the first reflected shock from



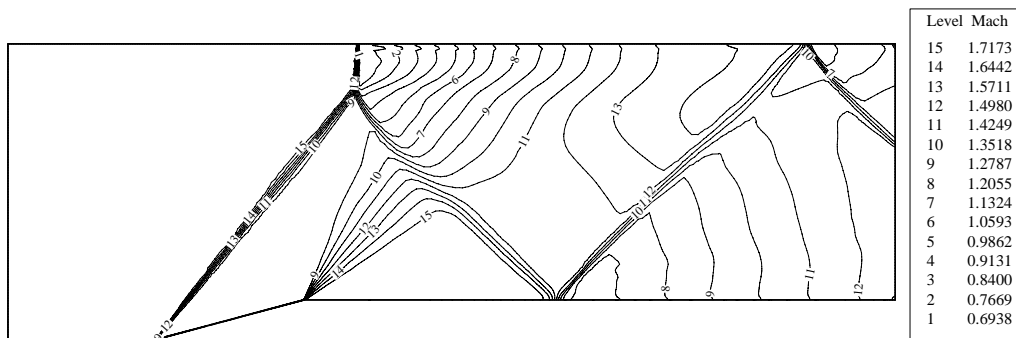


Figure 4.33: Mach number contours for Case 2.

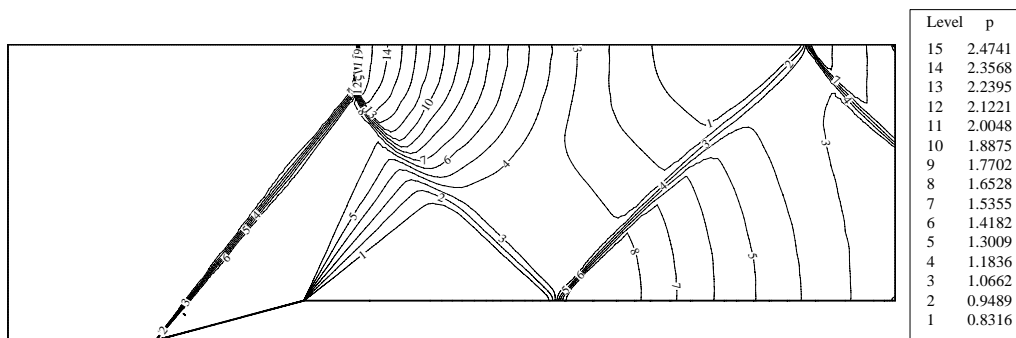


Figure 4.34: Pressure contours for Case 2.

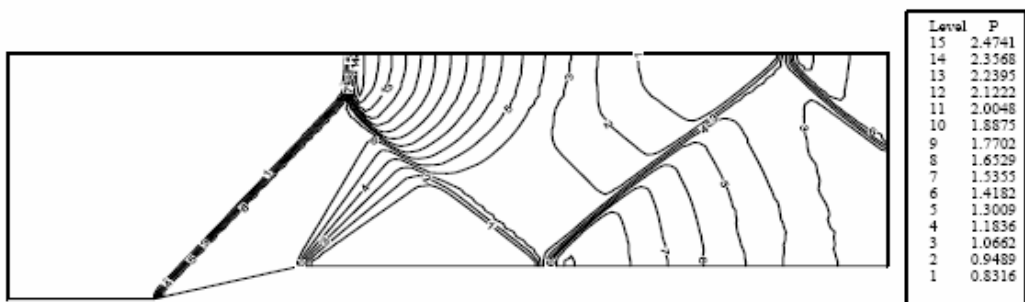
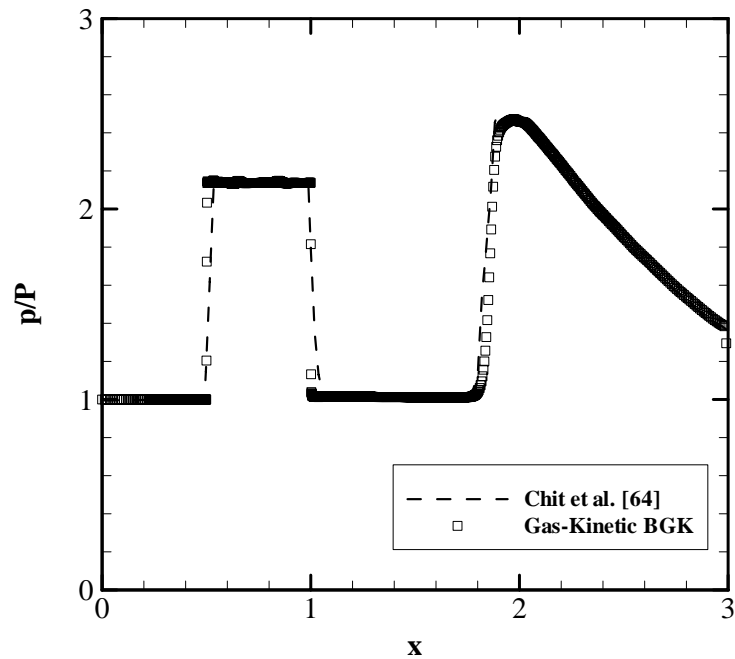


Figure 4.35: Pressure contours taken from [64].



**Figure 4.36:** Nondimensional pressure distribution along the lower wall of the channel for Case 2.

the top wall. Although the present case is solved with first order accurate Gas-Kinetic BGK scheme, the pressure contours are in very good agreement with the second order accurate results of [64], which is given in Fig. 4.35. The pressure distribution along the lower wall of the channel is shown in Fig. 4.36. As seen, the present prediction is in good agreement with the data given in Ref. [64].

### 4.2.3 Case 3: Inviscid High-Speed Flow Over a Blunt Body

The inviscid high-speed flow over a blunt body is selected as a third test case. The importance of this case comes from the fact that most of the classical schemes fail for such high-speed flows due to numerical instability [13, 14].

**Table 4.7:** Freestream conditions for Case 3.

Mach Number	Angle of Attack, <i>deg</i>	Pressure, <i>Pa</i>	Temperature, <i>K</i>
6.0	0.0	101325	288

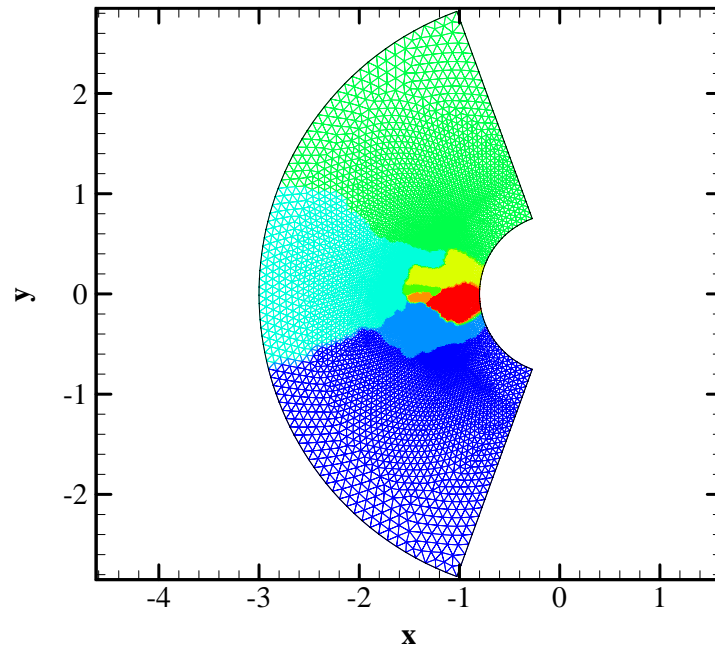


**Figure 4.37:** Computational mesh with partitions for Case 3.

This is known as the *carbuncle phenomenon*. The freestream conditions and the computational mesh with partitions are given in Table 4.7 and Fig. 4.37, respectively. The computational mesh consists of 13904 nodes and 27614 cells. Since the spurious oscillations are expected behind the bow shock along the stagnation streamline, computational grid is refined in this region.

Figures 4.38 and 4.39 show the density contours for the Gas-Kinetic BGK and Roe schemes, respectively. The Gas-Kinetic BGK scheme resolve the bow shock and stagnation region very well. On the other hand, Roe scheme could not add

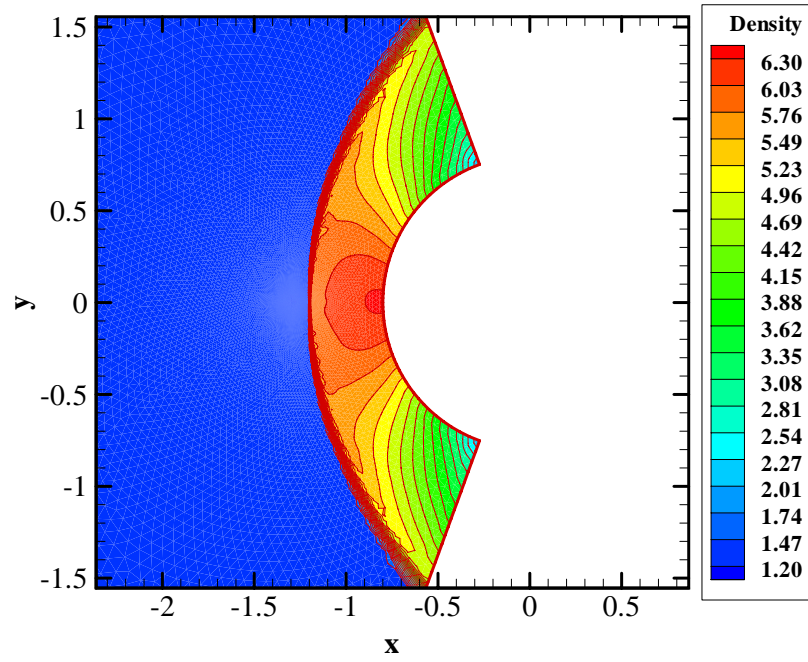


**Figure 4.38:** Density contours for Case 3 (Gas-Kinetic BGK scheme, zoomed view).

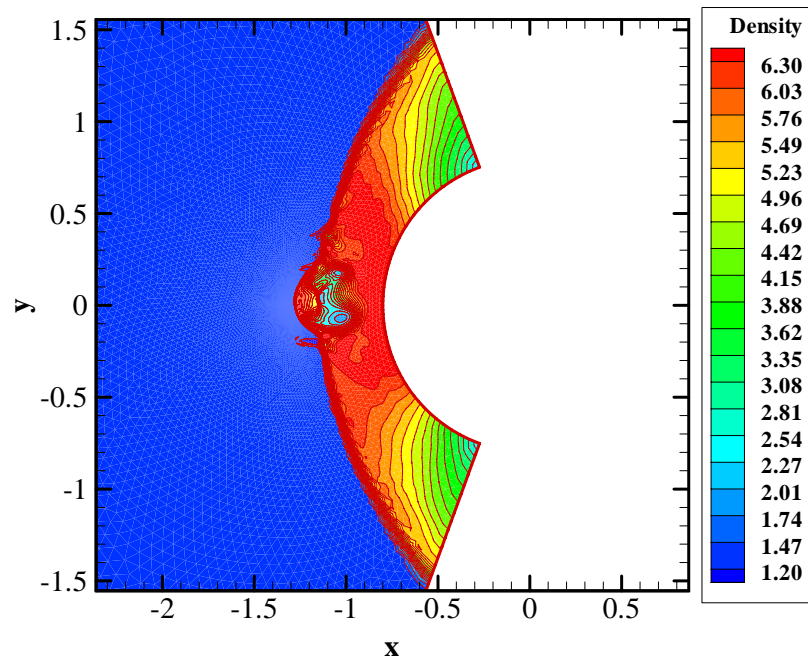


**Figure 4.39:** Density contours for Case 3 (Roe's FDS scheme, zoomed view).

enough dissipation in this region via contact and shear waves and gives spurious oscillations, so-called carbuncle phenomenon. Although this phenomenon can definitely be cured with entropy fix, there is no justification, either physical or mathematical for applying such a fix. It is also reported in the literature that there are other failings of Roe scheme without entropy fix such as odd-even decoupling and kinked Mach stem [13, 14]. The Gas-Kinetic BGK scheme is immune to this type of instabilities due to its underlying theory based on the particle distribution function.

#### 4.2.4 Case 4: Laminar Flow Over a Flat Plate

A flat plate at zero angle of attack is selected as a fourth test case for which the analytical Blasius solution is available. The freestream conditions and the computational mesh with partitions for this case are given in Table 4.8 and Fig. 4.40, respectively. The computational mesh consists of 14456 nodes and 22623 cells. The flat plate is placed between 0 and 1 and the boundary layer region is meshed with quadrilateral cells while triangular cells are used outside the boundary layer.

**Table 4.8:** Freestream conditions for Case 4.

Mach Number	Angle of Attack, <i>deg</i>	Reynolds Number
0.1	0.0	10000

Figure 4.41 shows the Mach contours and velocity vectors inside the boundary layer on the flat plate and the *u*-velocity and *v*-velocity profiles at four different *x*-locations are given in Figs. 4.42 and 4.43, respectively, along with the analyt-

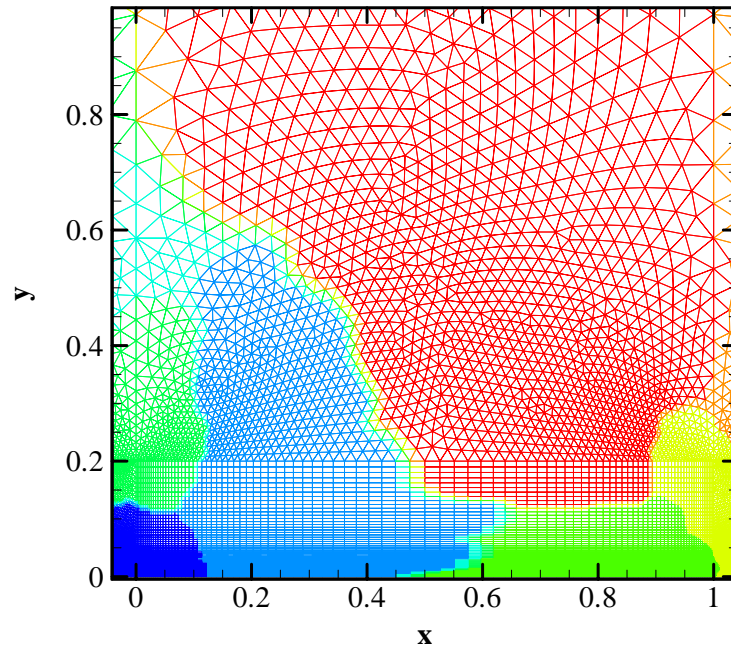


**Figure 4.40:** Computational mesh with partitions for Case 4 (Zoomed view).

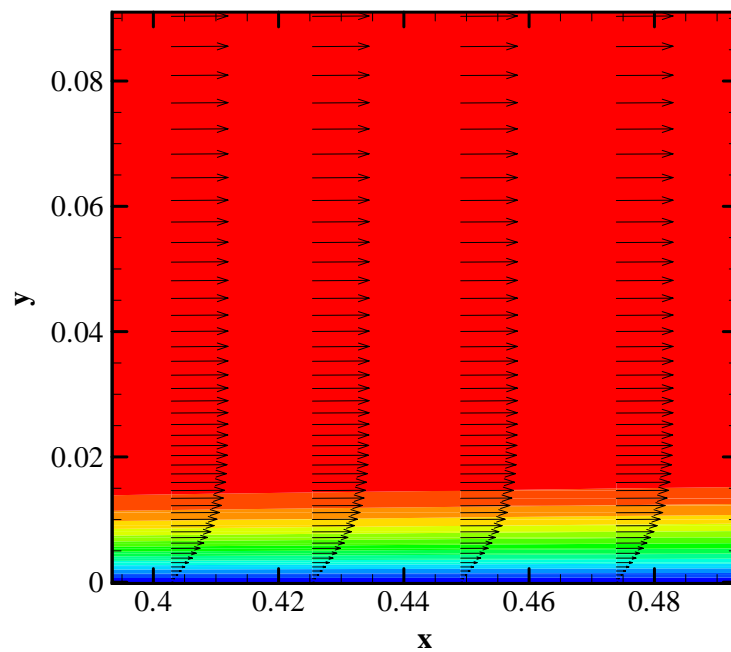


**Figure 4.41:** Mach number contours and velocity vectors for Case 4 (Zoomed view).

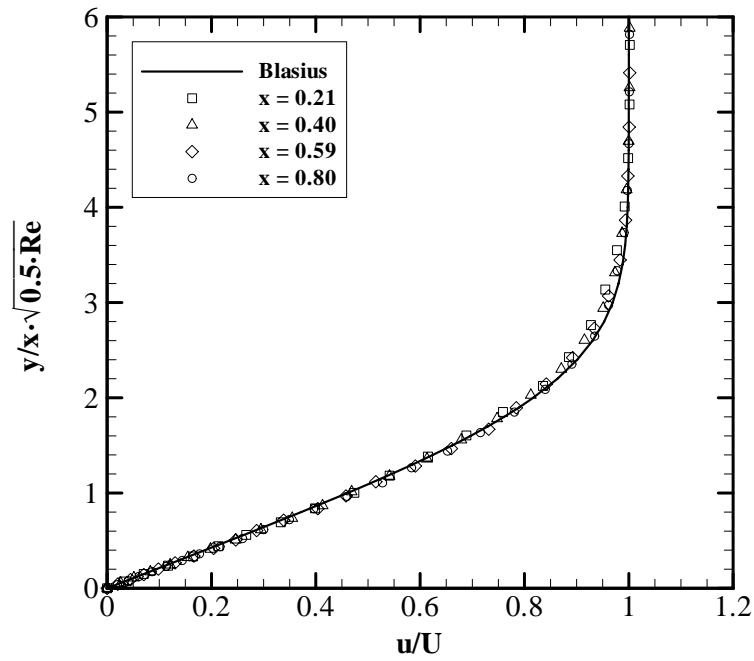


Figure 4.42: u-velocity profile in the boundary layer for Case 4.

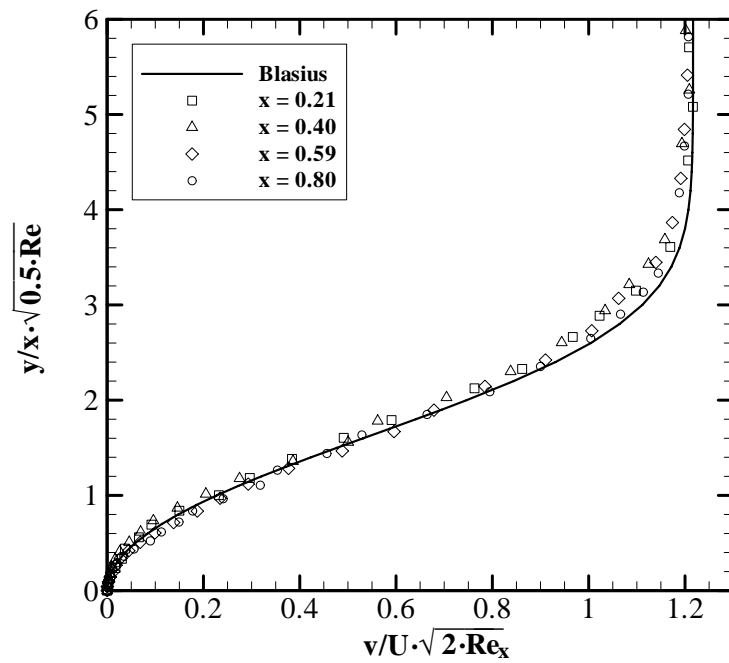


Figure 4.43: v-velocity profile in the boundary layer for Case 4.

ical Blasius solutions. The results compare well with the Blasius solutions. The Gas-Kinetic BGK scheme produces Navier-Stokes solution in smooth flow regions as expected. Moreover, the use of quadrilateral cells near the wall region leads to the better resolution of the boundary layers while the use of triangular cells outside reduces the overall number of cells.

#### 4.2.5 Case 5: Laminar Flow Over a Transonic Airfoil

The laminar flow over NACA0012 airfoil is selected as a fifth test case. This case has been used as a benchmark for viscous flows [65]. The freestream conditions and the computational mesh with partitions are given in Table 4.9 and Fig. 4.44, respectively. The computational mesh consists of 10662 nodes and 13914 cells.

**Table 4.9:** Freestream conditions for Case 5.

Mach Number	Angle of Attack, <i>deg</i>	Reynolds Number
0.8	10.0	500

The Mach contours obtained from the Gas-Kinetic BGK scheme is shown in Fig. 4.45. The shock wave on the upper surface of the airfoil interacts with the boundary layer and the flow separates near the trailing-edge. The separation on the suction side of the airfoil can be seen more clearly with streamlines, which is given in Fig. 4.46. Recently, May and Jameson [66] solved the same problem with a modified Gas-Kinetic BGK scheme on unstructured grids. A snapshot of the separation region presented in [66] is shown in Fig. 4.47. The size and shape of the recirculation region found in the two studies are in good agreement. The nondimensional pressure distribution on the surface of the



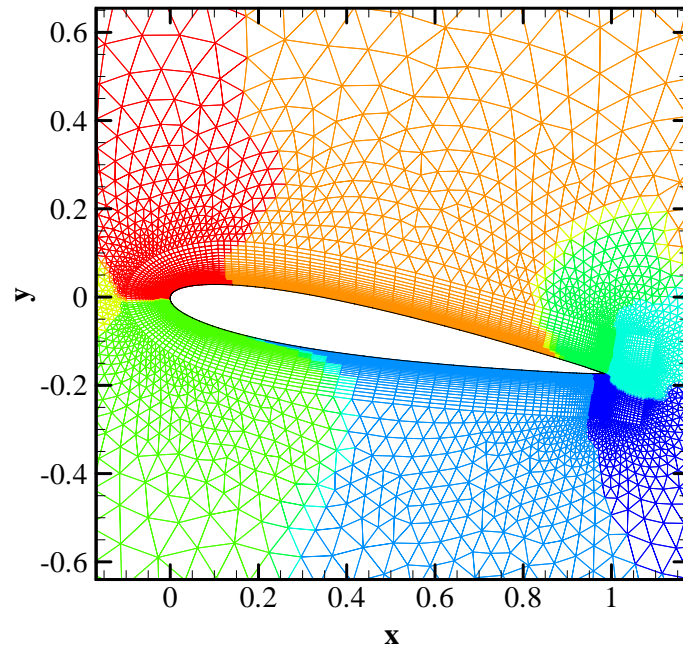


Figure 4.44: Computational mesh with partitions for Case 5 (Zoomed view).

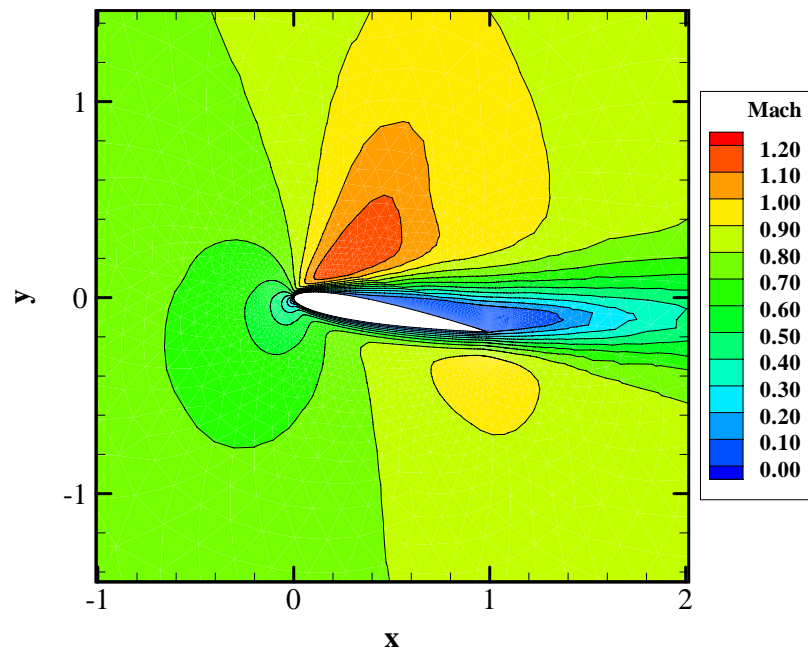


Figure 4.45: Mach number contours for Case 5.

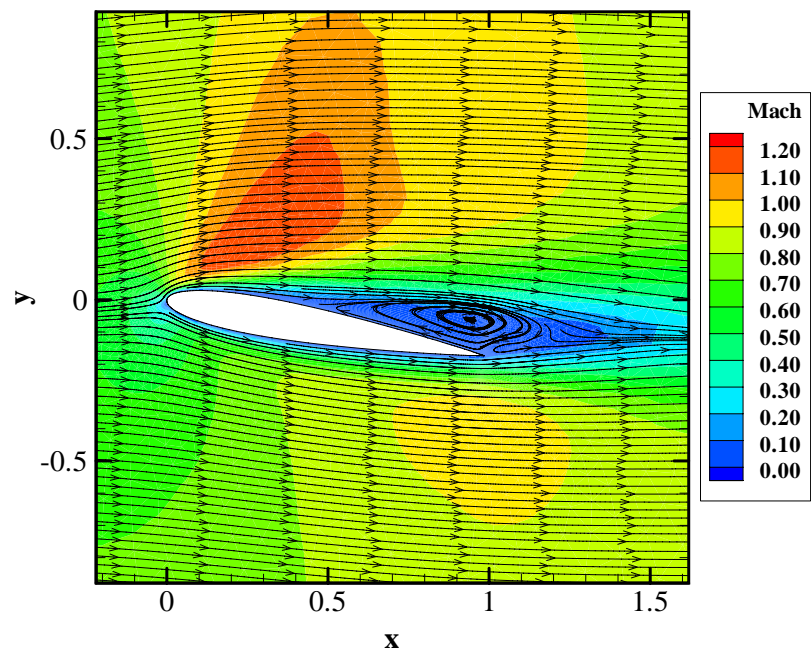


Figure 4.46: Streamlines and the separation on the suction side for Case 5.

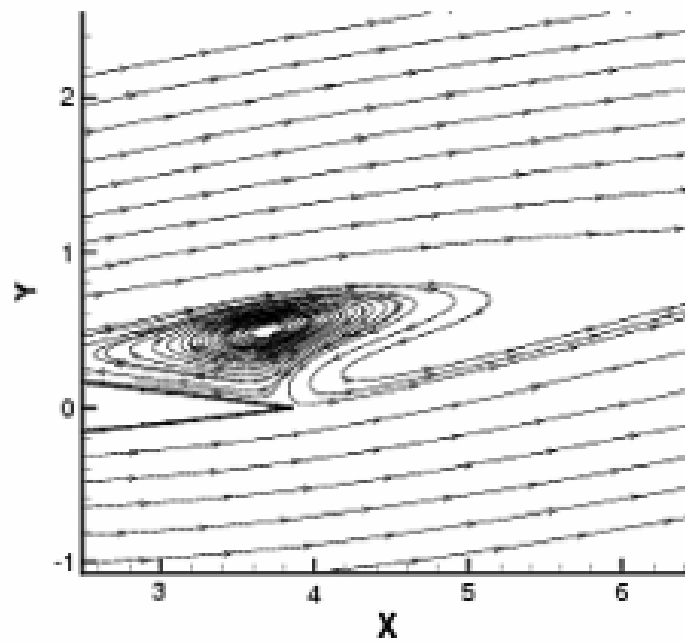
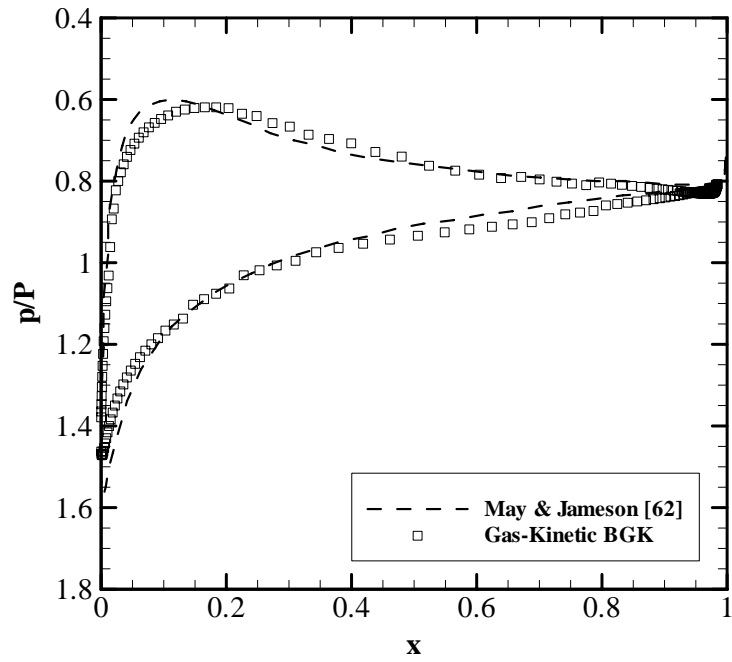
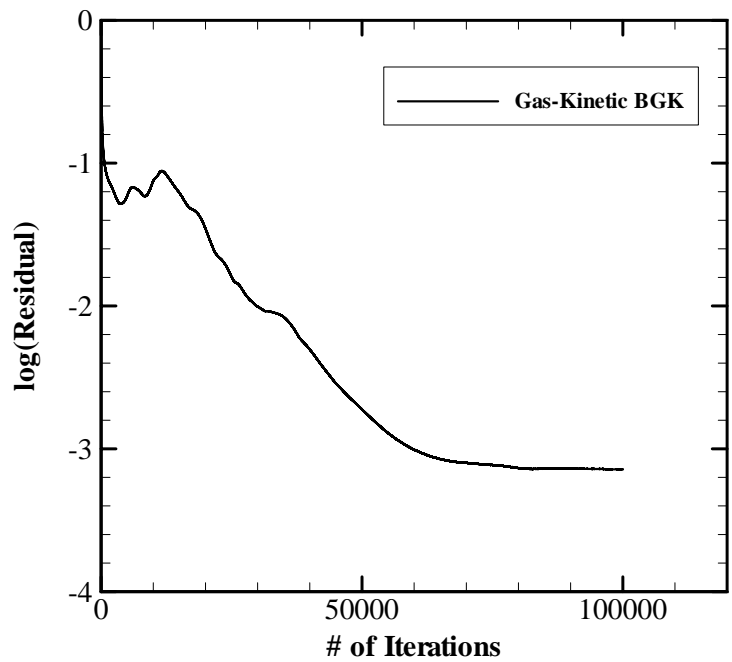


Figure 4.47: Streamlines and the separation on the suction side taken from [66].



**Figure 4.48:** Nondimensional pressure distribution on the airfoil surface for Case 5.



**Figure 4.49:** Convergence history for Case 5.

airfoil is presented in Fig. 4.48 along with the results of May and Jameson [66]. The two results compare quite well. The discrepancies near the leading- and trailing-edge may be attributed to the different grid resolutions used in the two studies. The present grid density near the leading- and trailing-edge regions appears to be much higher than the one in the reference study and it may be assumed that those regions are resolved better in the present study.

Finally, the convergence history is shown in Fig. 4.49. The Gas-Kinetic BGK scheme converges smoothly for this case.

#### **4.2.6 Summary**

The 2-D test cases considered in this section show that the Gas-Kinetic BGK scheme gives accurate results for both inviscid and viscous flows. The unphysical phenomena such as carbuncle, odd-even decoupling, etc. have never been observed while it is found that the Roe scheme needs some special treatment in certain problems. It is also observed that the numerical entropy generation in the Gas-Kinetic BGK scheme is much less than that of Roe scheme. Since the flow solution based on the Kinetic Flux Vector Splitting scheme is found to be dissipative, this scheme is not considered in the remaining test cases. The use of hybrid grids leads to the better resolution of boundary layers in viscous flows while reducing the total number of grid cells. It is worth noting that the high parallel efficiency of the Gas-Kinetic BGK scheme is maintained as the number of processors increases. Thus, the parallel computations significantly improve the computation time of the Gas-Kinetic BGK scheme.

### 4.3 3-D Flows

In this section, 3-D results based on the Gas-Kinetic BGK scheme are presented. Inviscid flows over missile configurations and a wing, and a viscous flow over a flat plate are considered. The solutions are obtained in parallel. The results are compared to those of the classical schemes as well as analytical and the available experimental data.

#### 4.3.1 Case 1: Inviscid Subsonic Flow Over a Missile

As a first validation case, the inviscid subsonic flow over a Sidewinder-type missile is computed at various angles of attack and the aerodynamic loads are compared to the available experimental data [67]. The freestream conditions and the surface mesh for this case are given in Table 4.10 and Fig. 4.50, respectively. The computational mesh consists of 228649 nodes and 1340023 cells.

**Table 4.10:** Freestream conditions for Case 1.

Mach Number	Pressure, $Pa$	Temperature, $K$
0.2	101325	288

Figure 4.51 shows the pressure contours on the missile vertical plane of symmetry at an angle of attack of  $8^\circ$ . The longitudinal aerodynamic coefficients obtained from the Gas-Kinetic BGK scheme along with the experimental data are presented in Figs. 4.52, 4.53 and 4.54. The normal force and pitching moment predictions agree quite well with the experimental values. In the numerical solution, the base pressure correction is made by setting the base area pressures to the freestream pressure as specified in [67]. The axial force coefficient results

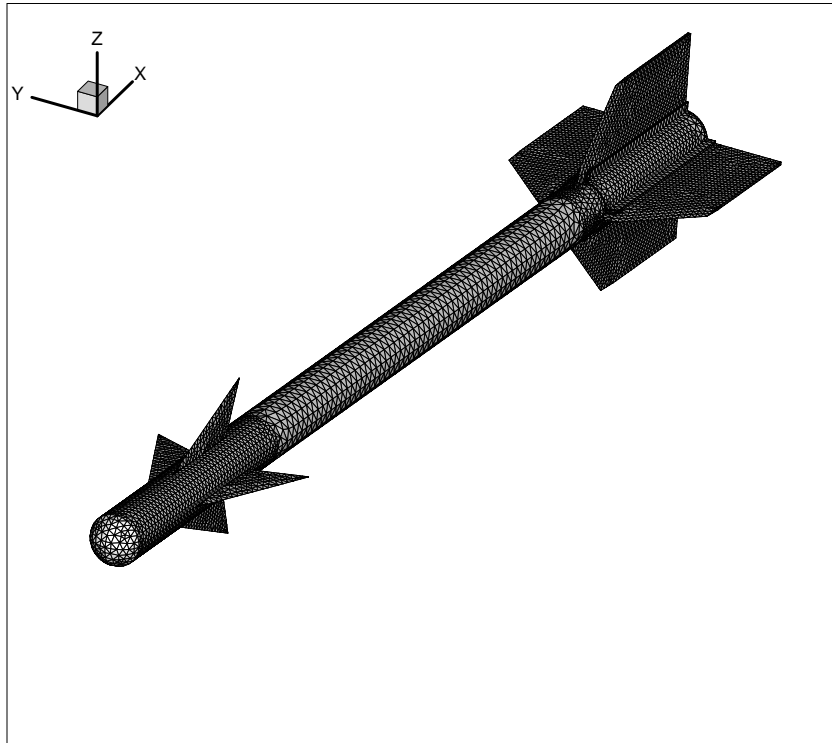


**Figure 4.50:** Surface mesh for Case 1.

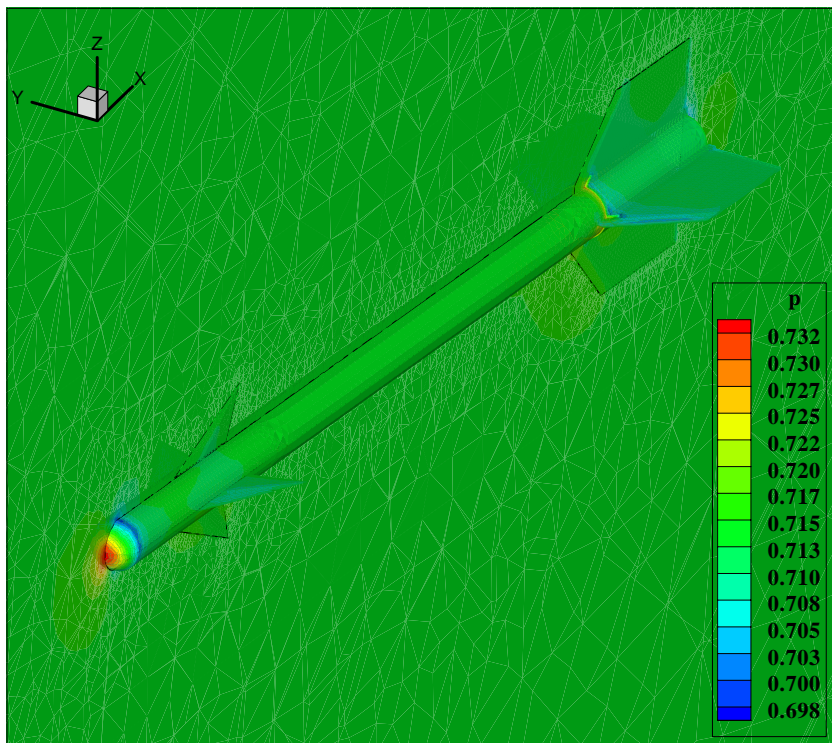


**Figure 4.51:** Pressure contours on the vertical plane of symmetry at  $8^\circ$  angle of attack for Case 1.

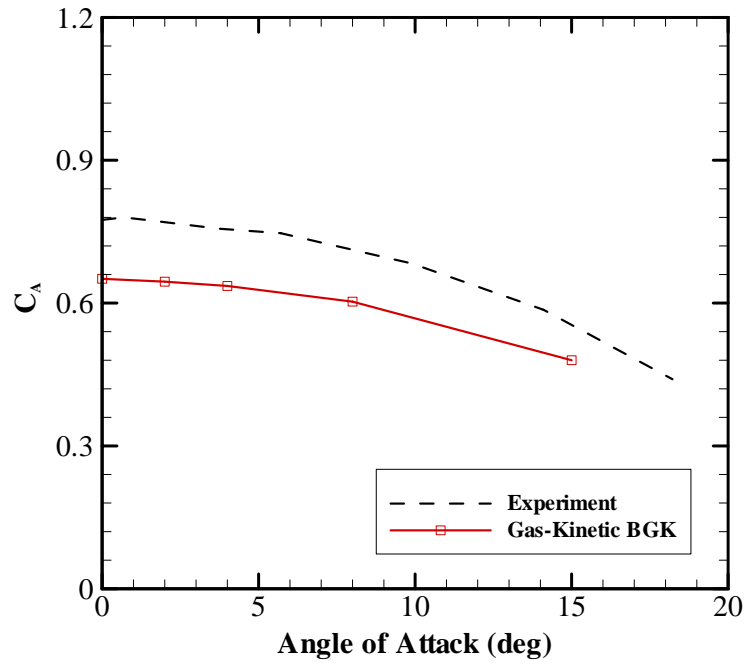


Figure 4.52: Axial force coefficient for Case 1.

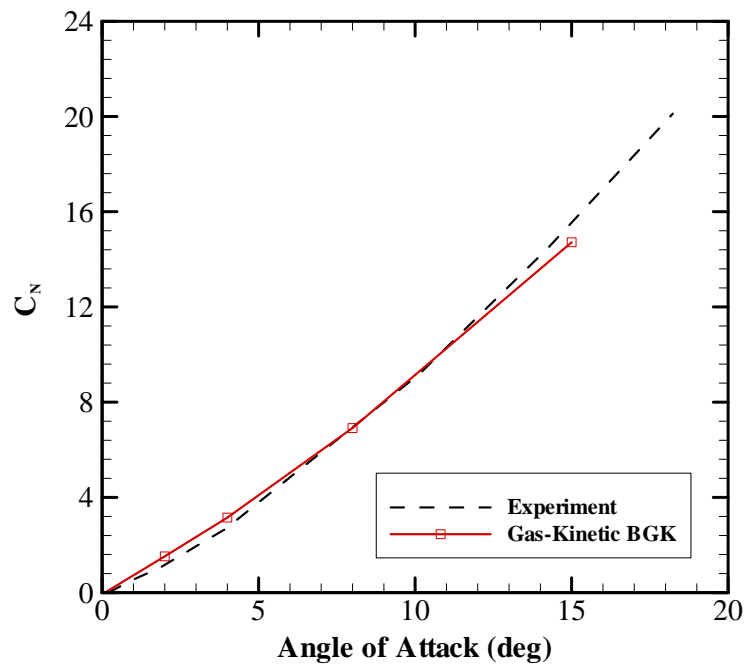
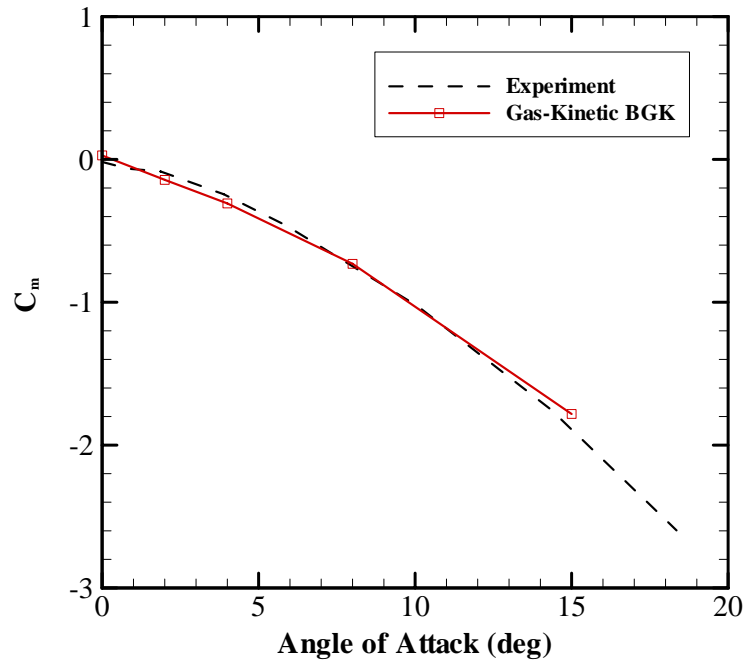


Figure 4.53: Normal force coefficient for Case 1.



**Figure 4.54:** Pitching moment coefficient for Case 1.

are underpredicted and do not match the experimental data. This is attributed to the viscous (turbulence) effects.

### 4.3.2 Case 2: Inviscid Transonic Flow Over a Wing

ONERA M6 transonic wing, which has available experimental data [68], is selected as a second validation case. The freestream conditions and the surface mesh with partitions for this case are given in Table 4.11 and Fig. 4.55, respectively. These conditions actually correspond to a Reynolds number of 11.72

**Table 4.11:** Freestream conditions for Case 2.

Mach Number	Angle of Attack, <i>deg</i>	Angle of Sideslip, <i>deg</i>	Pressure, <i>Pa</i>	Temperature, <i>K</i>
0.8395	3.06	0.0	101325	288



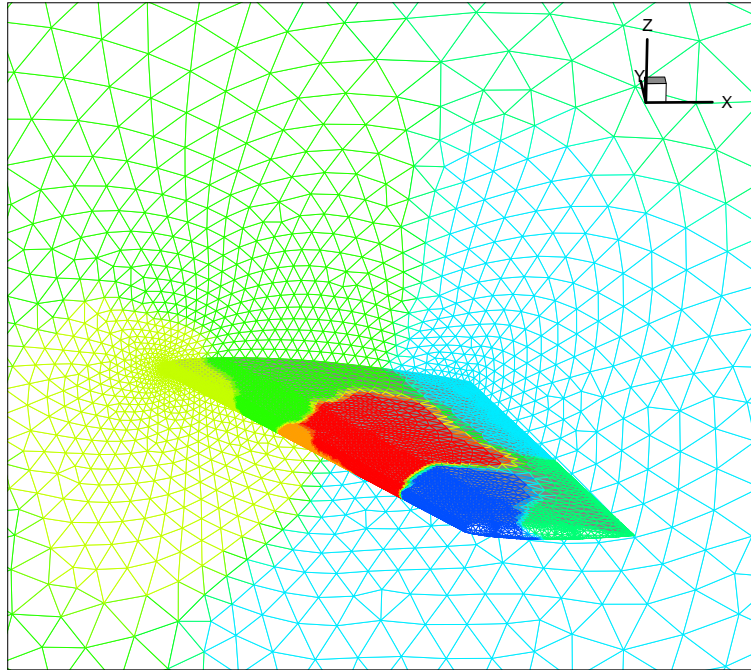


Figure 4.55: Surface mesh with partitions for Case 2.

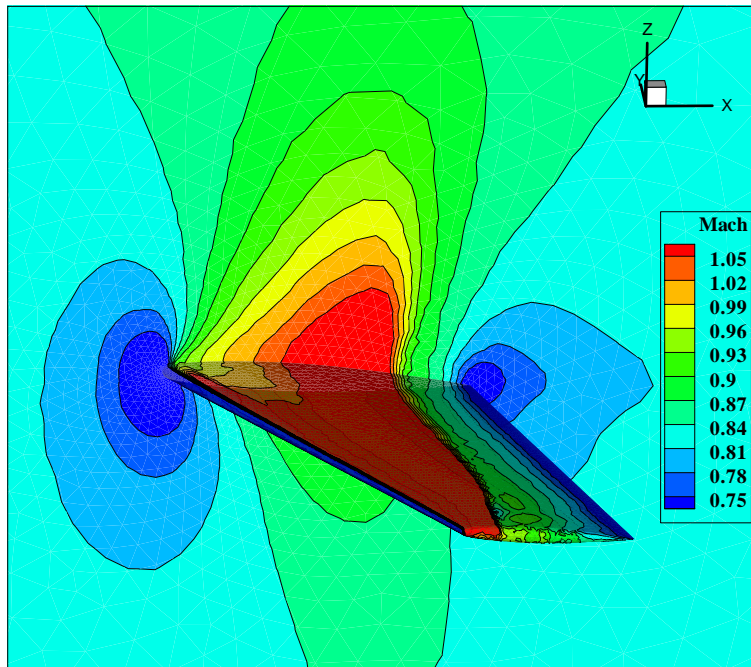


Figure 4.56: Mach number contours for Case 2.

million based on the mean aerodynamic chord. The computational mesh consists of 90696 nodes and 513722 cells.

Figure 4.56 shows the Mach number contours obtained from the Gas-Kinetic BGK scheme at the wing surface and symmetry plane. The comparisons of the surface pressure coefficient at different sections of the wing with the experimental data are given in Figs. 4.57, 4.58, 4.59, 4.60 and 4.61. The results of the Gas-Kinetic BGK and Roe schemes are generally in good agreement with the experimental data. The pressure distribution at the lower wing surface is predicted better by the the Gas-Kinetic BGK scheme than the Roe scheme. The shock waves generated at different sections of the wing are well captured, however, the shock locations are expectedly overpredicted in comparison to the experimental data due to the inviscid flow assumption.

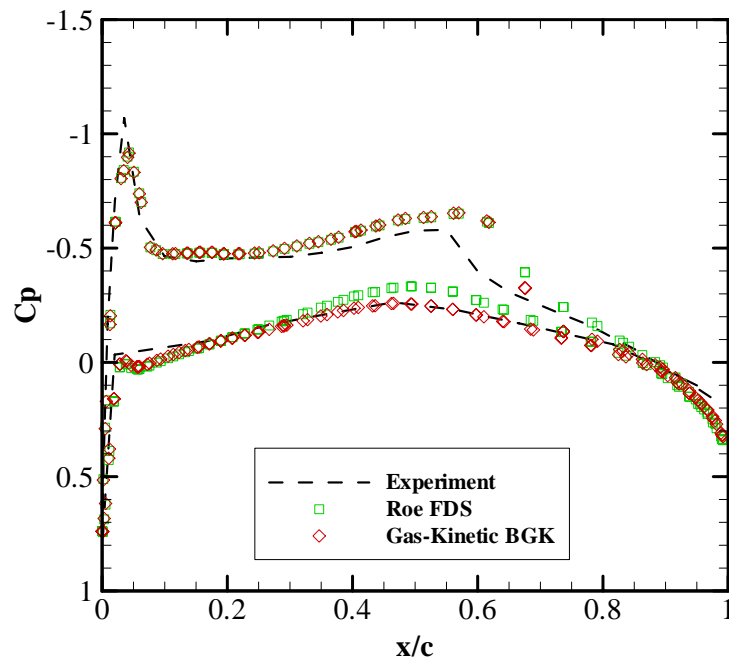


Figure 4.57: Surface pressure coefficient at  $y/b=0.2$  for Case 2.

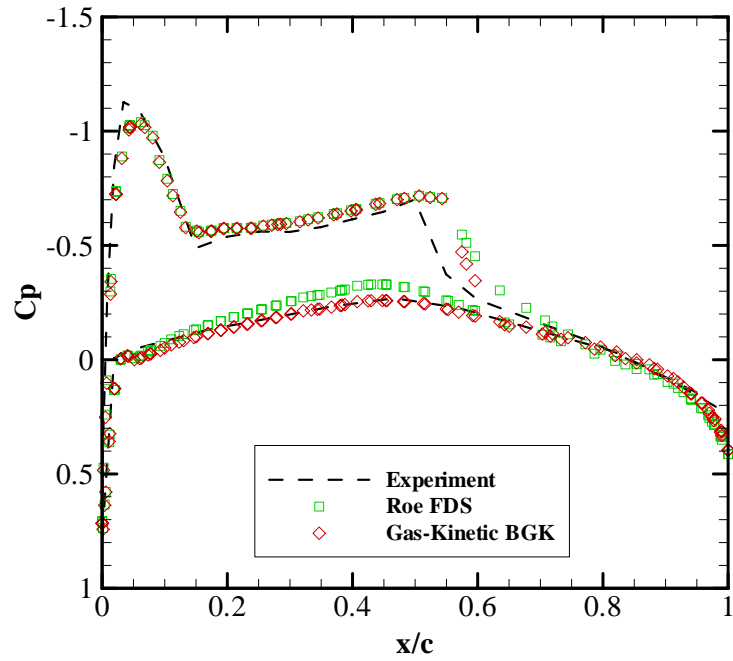


Figure 4.58: Surface pressure coefficient at  $y/b=0.44$  for Case 2.

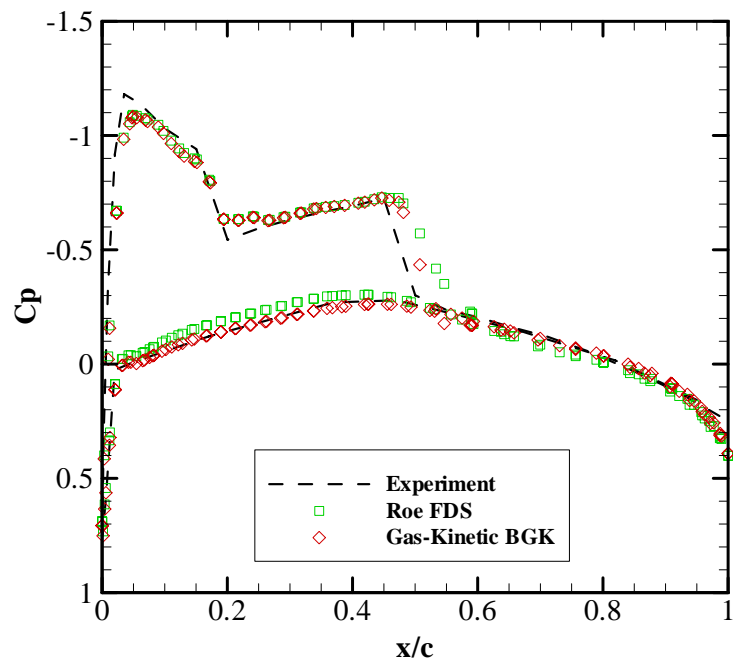


Figure 4.59: Surface pressure coefficient at  $y/b=0.65$  for Case 2.

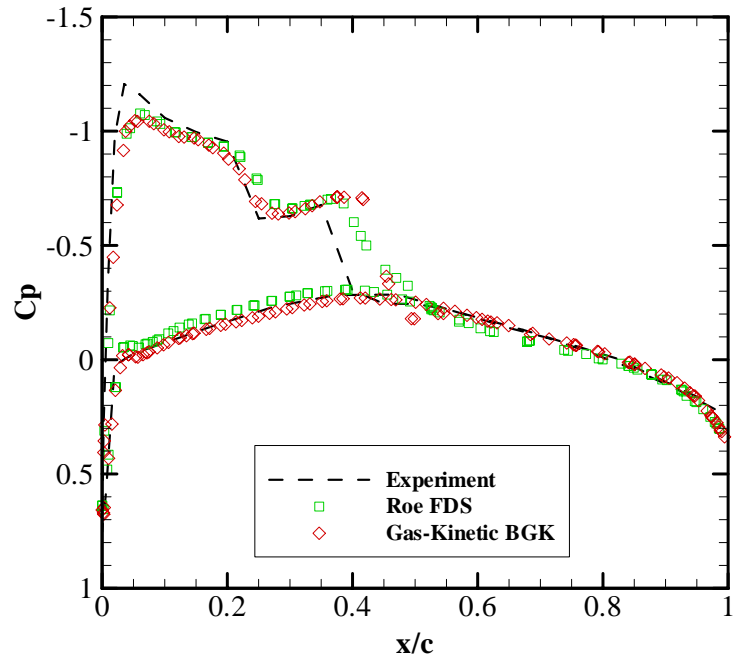


Figure 4.60: Surface pressure coefficient at  $y/b=0.8$  for Case 2.

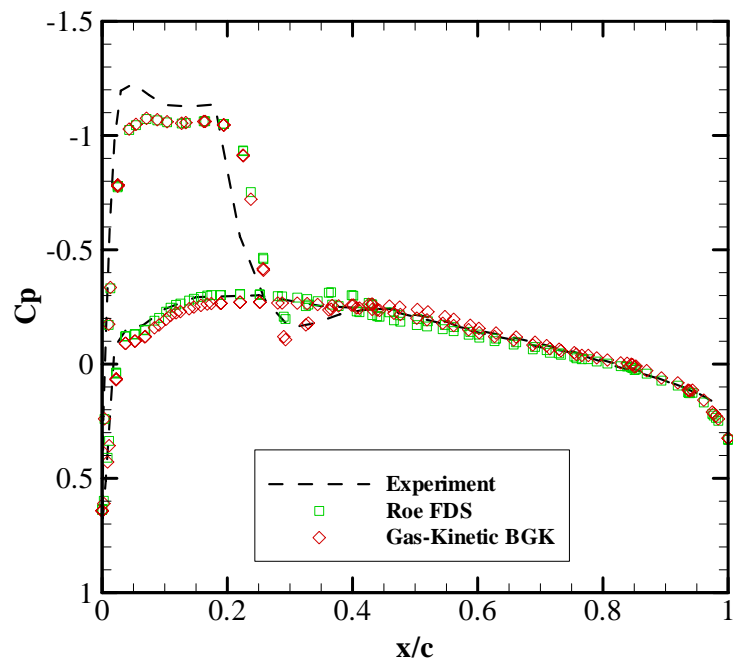
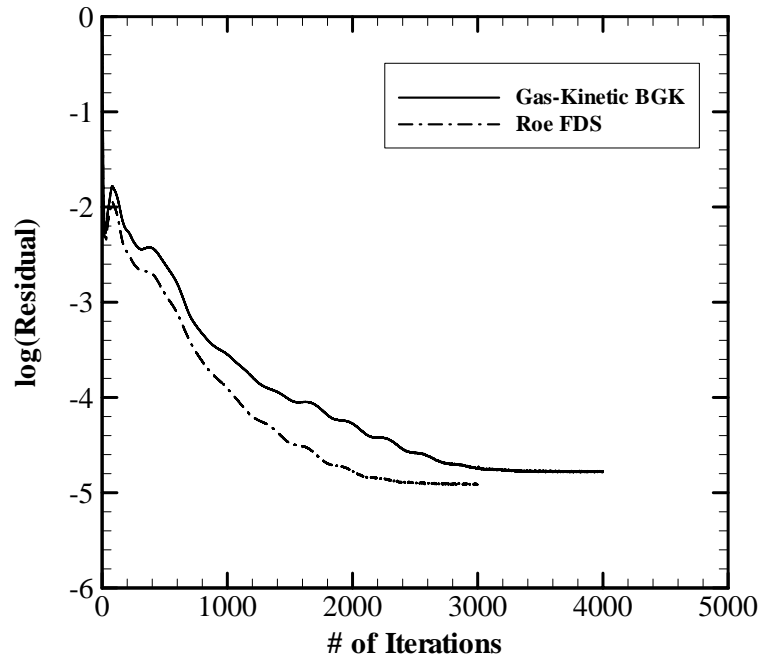


Figure 4.61: Surface pressure coefficient at  $y/b=0.95$  for Case 2.



**Figure 4.62:** Convergence history for Case 2.

Finally, the convergence histories are shown in Fig. 4.62. The Gas-Kinetic BGK and Roe schemes have similar convergence behavior.

### 4.3.3 Case 3: Inviscid Supersonic Flow Over a Missile

Inviscid supersonic flow over a Sparrow-type missile is selected as a third case. The solutions are obtained for various angles of attack and the results are compared to the available experimental data [69]. The freestream conditions and the surface mesh for this case are given in Table 4.12 and Fig. 4.63, respectively. The computational mesh consists of 214630 nodes and 1238305 cells.

**Table 4.12:** Freestream conditions for Case 3.

Mach Number	Pressure, $Pa$	Temperature, $K$
1.5	101325	288

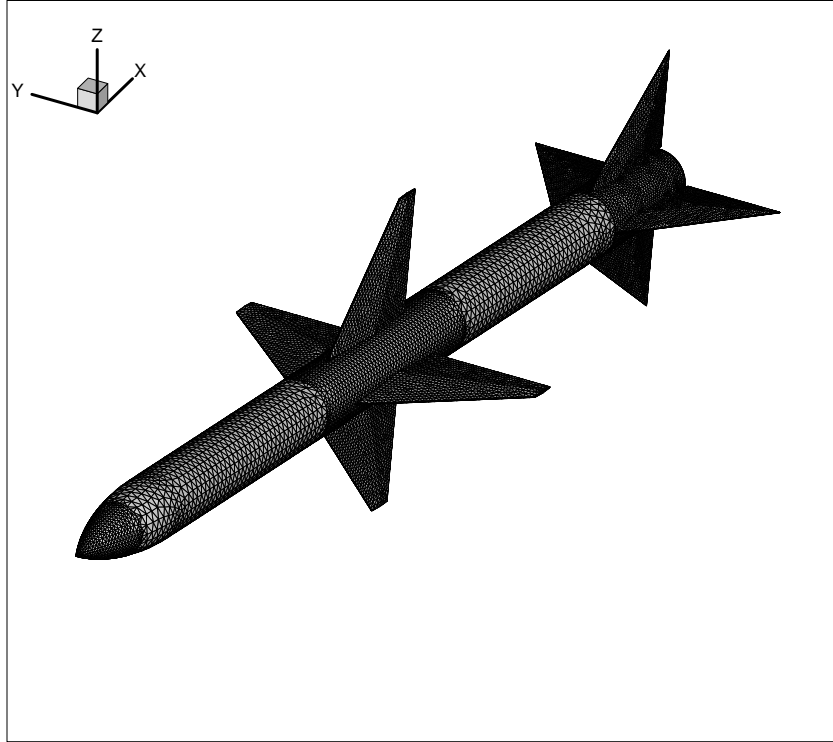


**Figure 4.63:** Surface mesh for Case 3.

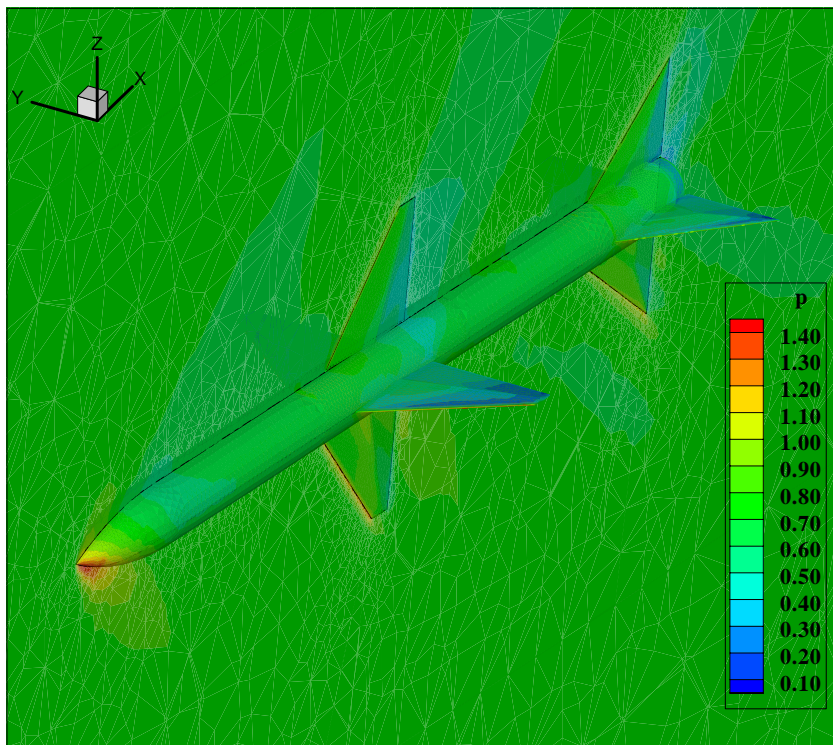


**Figure 4.64:** Pressure contours on the vertical plane of symmetry at  $10^\circ$  angle of attack for Case 3.

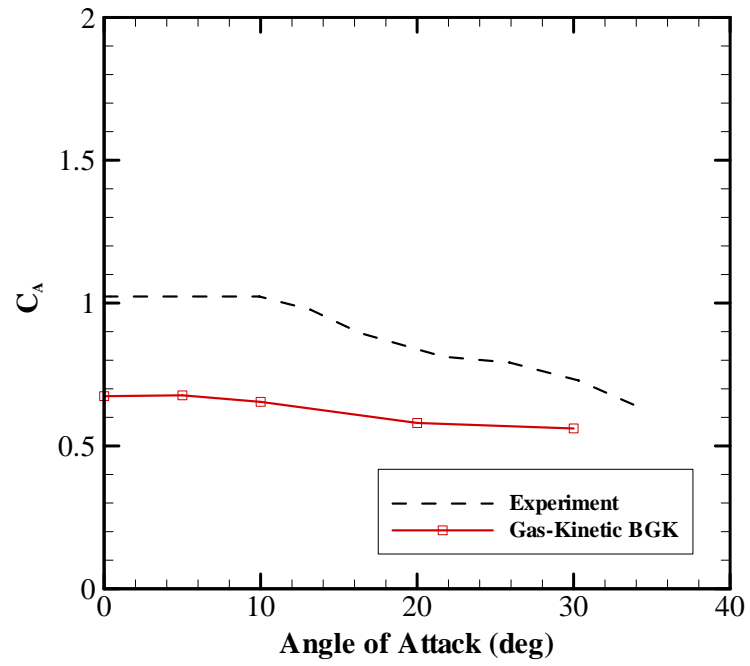


Figure 4.65: Axial force coefficient for Case 3.

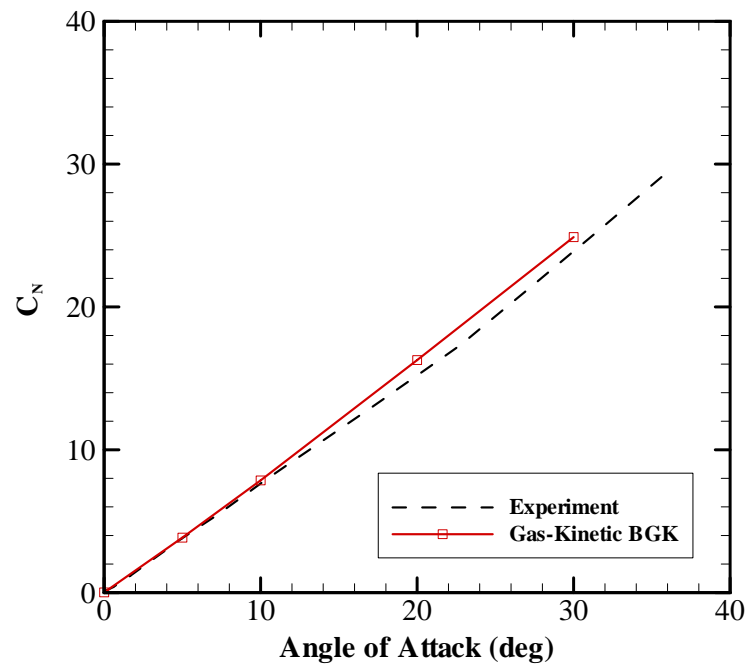
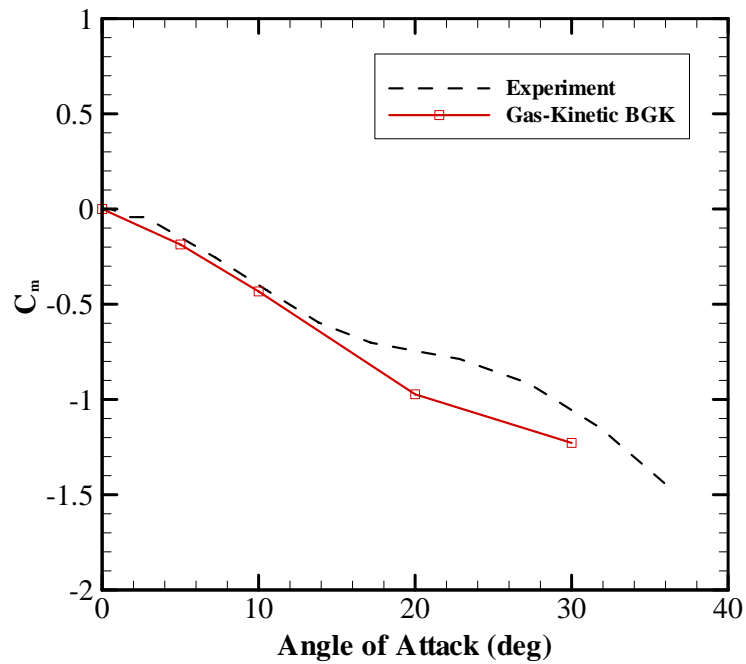


Figure 4.66: Normal force coefficient for Case 3.



**Figure 4.67:** Pitching moment coefficient for Case 3.

Figure 4.64 shows the pressure contours on the missile vertical plane of symmetry at an angle of attack of  $10^\circ$ . The longitudinal aerodynamic coefficients obtained from the Gas-Kinetic BGK scheme along with the experimental data are presented in Figs. 4.65, 4.66 and 4.67. The normal force and pitching moment coefficient results agree very well with the experimental values up to an angle of attack of approximately  $12^\circ$ . At high angles of attack, the vortices generated by the wings of the missile generates a complex flowfield on the tail section and this flowfield causes nonlinearities on the normal force and pitching moment coefficients. Present Euler solution could not resolve this complex flowfield and that is why the results of the Gas-Kinetic BGK scheme at high angles of attack are far from the experimental data. In the numerical solution, the base pressure correction is made by setting the base area pressures to the



freestream pressure as specified in [69]. The axial force coefficient results are underpredicted and do not match the experimental data. This is also attributed to the viscous (turbulence) effects.

#### 4.3.4 Case 4: Laminar Flow Over a Flat Plate

As a fourth case, the flat plate given in § 4.2.4 is solved by extruding it in the third dimension and the results are compared to the analytical Blasius solution. The freestream conditions are given in Table 4.13. Three different com-

**Table 4.13:** Freestream conditions for Case 4.

Mach Number	Angle of Attack, <i>deg</i>	Reynolds Number
0.1	0.0	10000

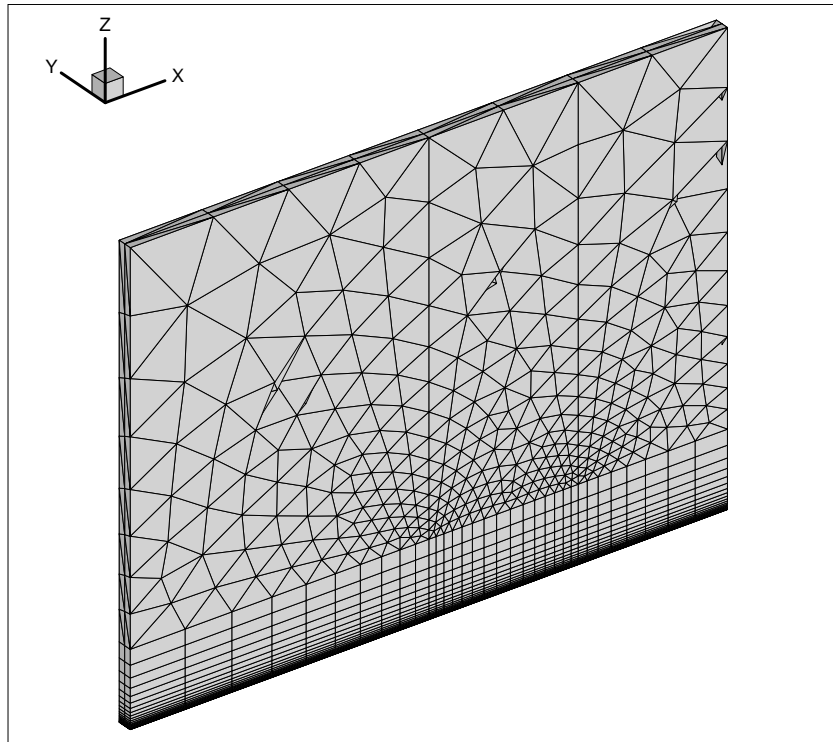


**Figure 4.68:** Coarse mesh for Case 4.

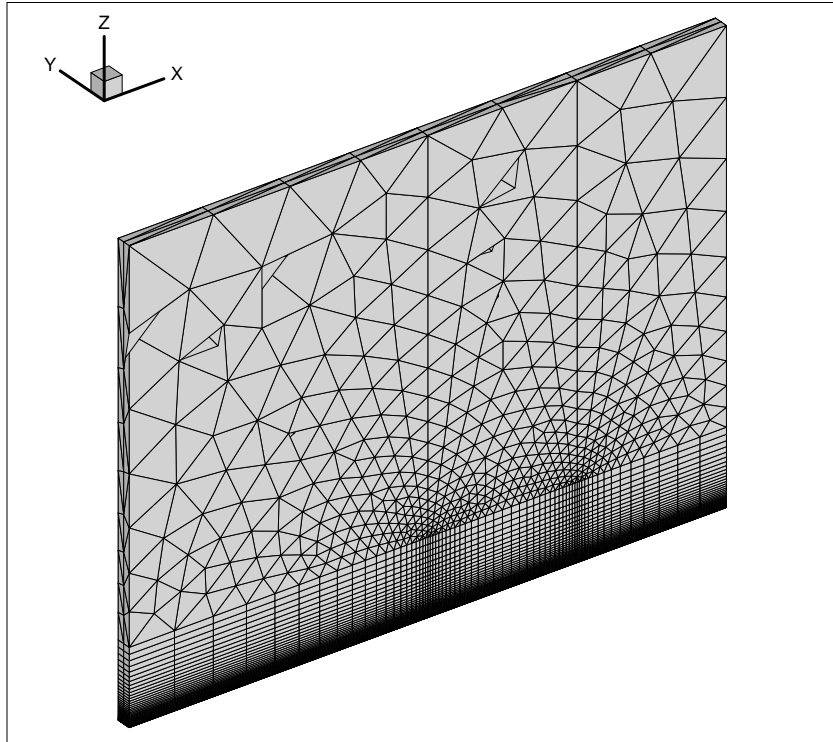


**Figure 4.69:** Medium mesh for Case 4.

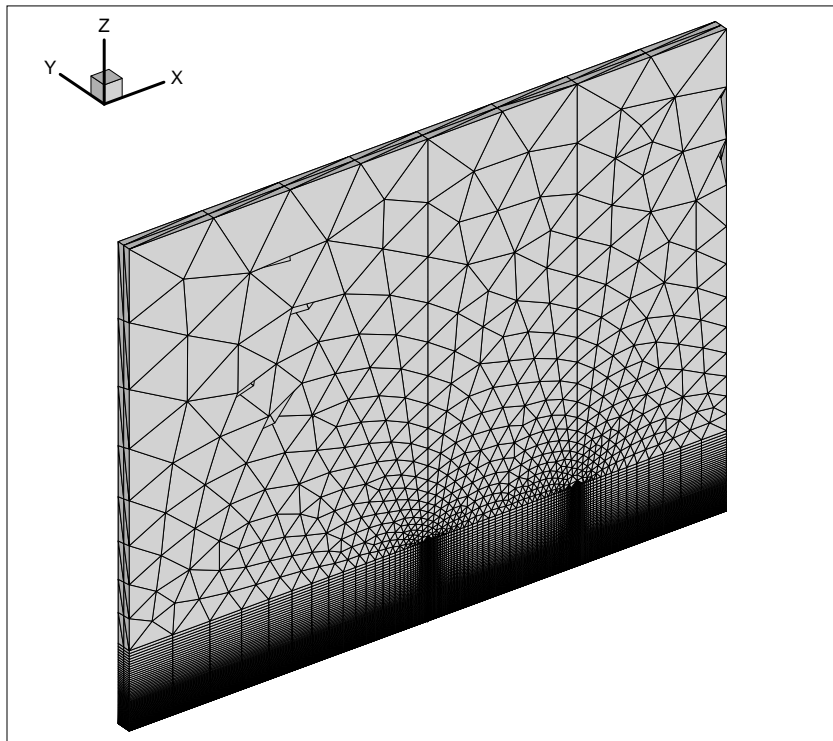


**Figure 4.70:** Fine mesh for Case 4.

putational meshes are used for this case in order to see the mesh dependency, which are presented in Figs. 4.68, 4.69 and 4.70 respectively. The coarse mesh consists of 3545 nodes and 5223 cells, the medium mesh consists of 11403 nodes and 12005 cells and the fine mesh consists of 41407 nodes and 33807 cells. The flat plate is again placed between 0 and 1 and the boundary layer region is meshed with hexahedron cells while pyramid and tetrahedron cells are used at the farfield.

Figures 4.71 and 4.72 show the comparison of  $u$ -velocity and  $v$ -velocity profiles obtained from three different meshes at  $y = 0$  plane and at  $x = 0.44$ . The results on medium and fine mesh are quite similar indicating that the mesh independency is reached while the coarse mesh gives overpredicted results for both velocity profiles. The Mach contours and velocity vectors inside the boundary layer on the flat plate at  $y = 0$  plane for the medium mesh is presented in Fig. 4.73. The comparisons of  $u$ -velocity and  $v$ -velocity profiles at three different  $y$ -planes for two different  $x$ -locations are given in Figs. 4.74, 4.75, 4.76 and 4.77, respectively, for the medium mesh along with the analytical Blasius solutions. The results of the Gas-Kinetic BGK scheme compare quite well with the Blasius solutions at different  $y$ -planes and  $x$ -locations. Moreover, the use of hexahedron cells near the wall region leads to the better resolution of the boundary layer while the use of tetrahedron cells outside greatly reduces the overall number of cells. This verifies the accuracy and robustness of the proposed approach. Finally, the convergence history for the medium mesh is shown in Fig. 4.78.

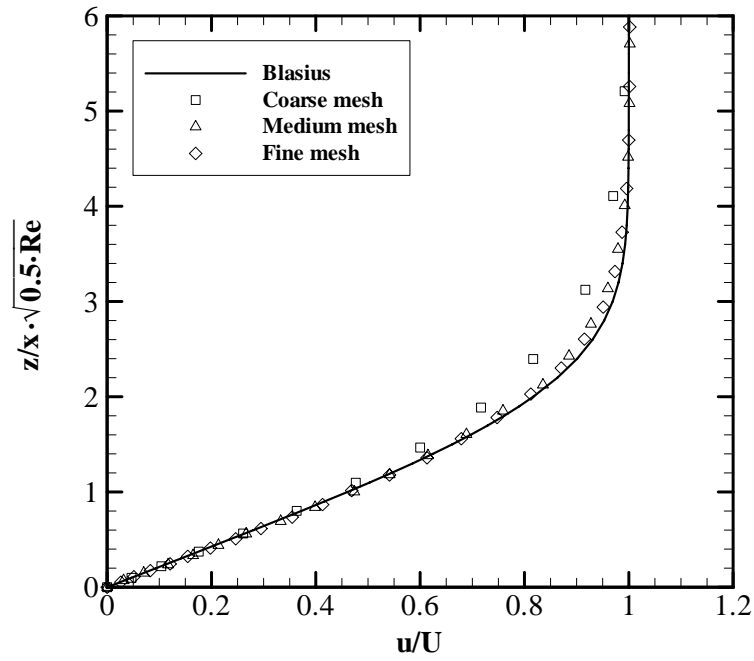


**Figure 4.71:** Comparison of  $u$ -velocity profile in the boundary layer at  $x=0.44$  for different meshes.

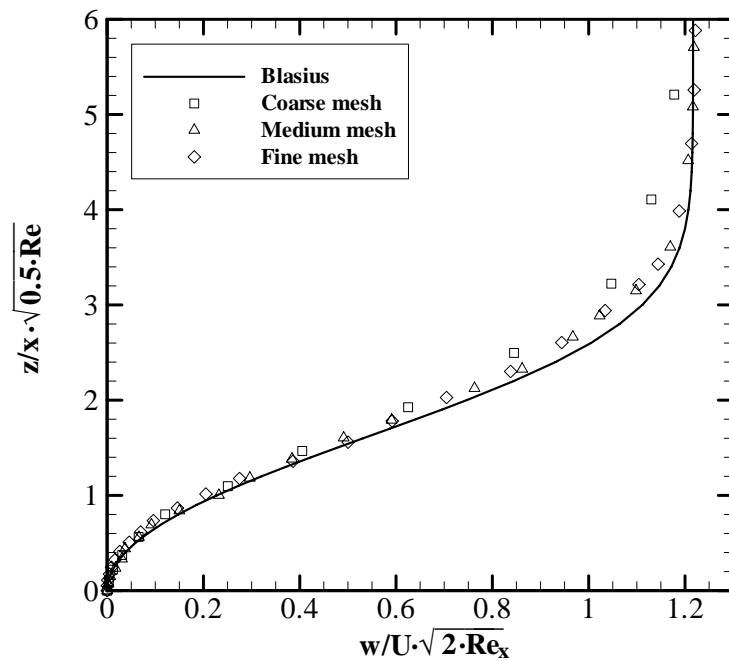


**Figure 4.72:** Comparison of  $v$ -velocity profile in the boundary layer at  $x=0.44$  for different meshes.

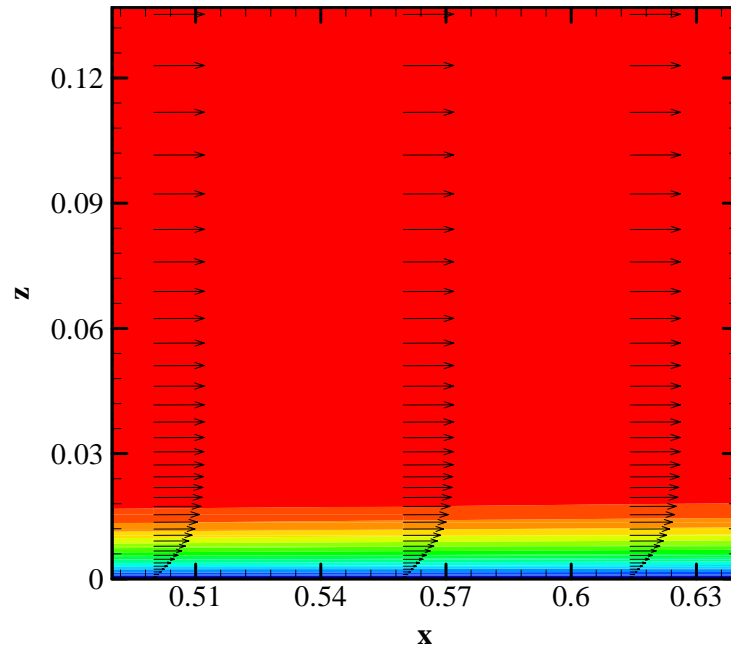


**Figure 4.73:** Mach number contours and velocity vectors at  $y=0$  plane for Case 4 (Medium mesh, zoomed view).

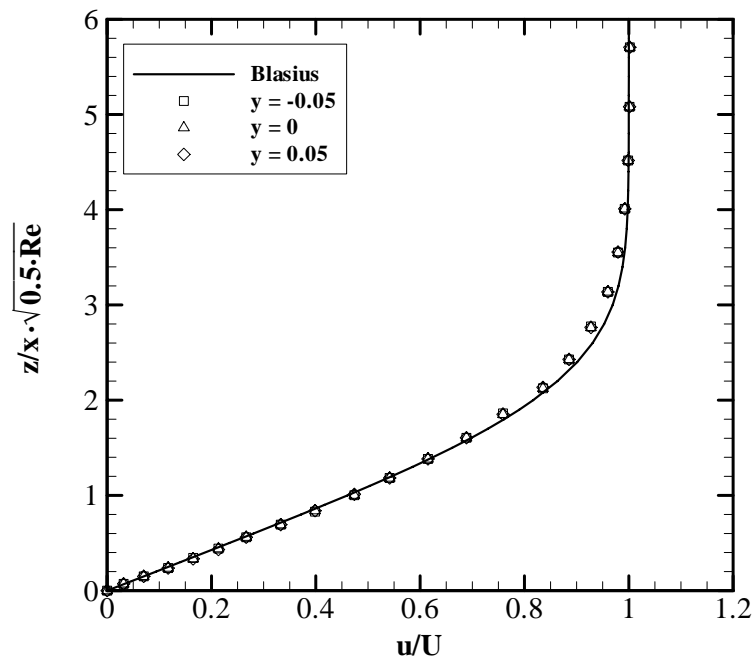


**Figure 4.74:**  $u$ -velocity profile in the boundary layer at  $x=0.44$  for Case 4 (Medium mesh).

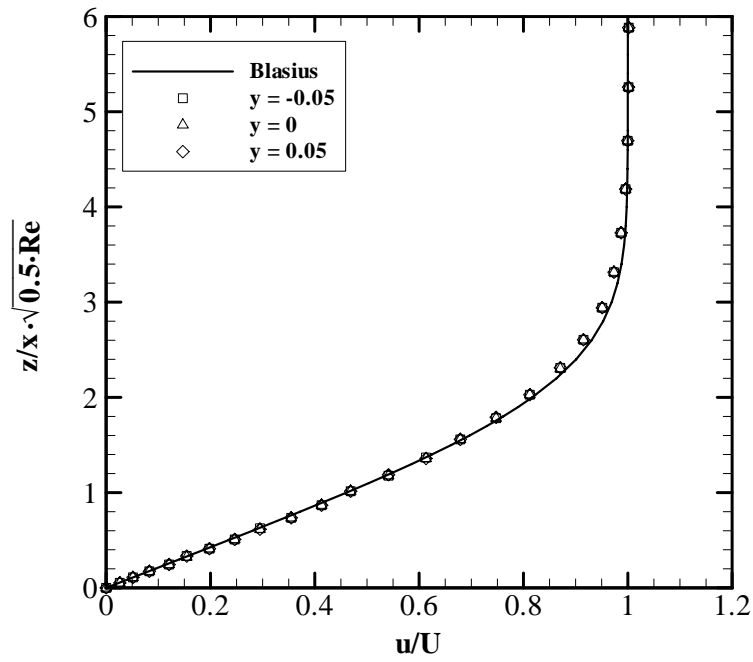


**Figure 4.75:**  $u$ -velocity profile in the boundary layer at  $x=0.66$  for Case 4 (Medium mesh).

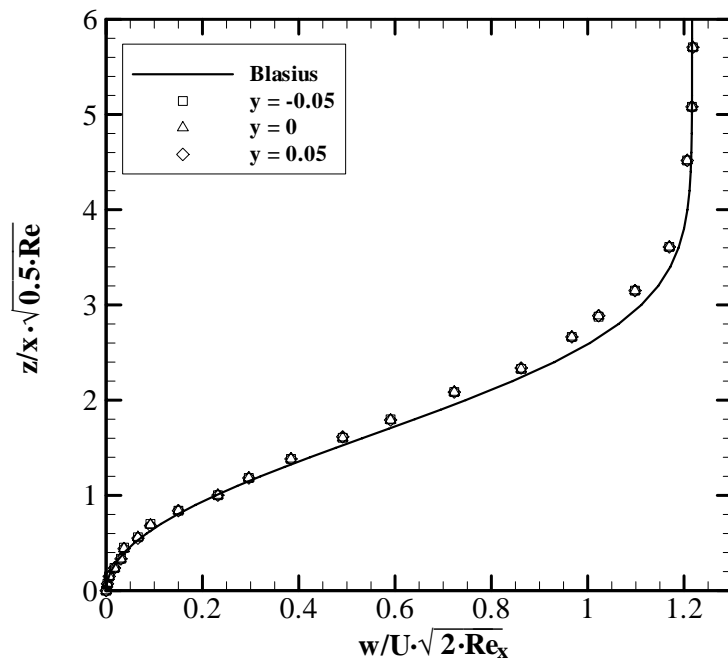


**Figure 4.76:**  $v$ -velocity profile in the boundary layer at  $x=0.44$  for Case 4 (Medium mesh).

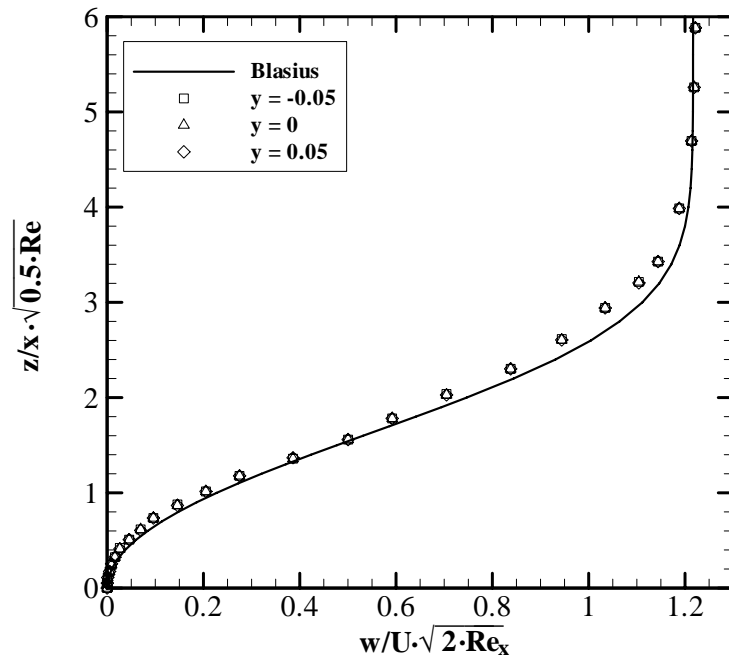


Figure 4.77:  $v$ -velocity profile in the boundary layer at  $x=0.66$  for Case 4 (Medium mesh).

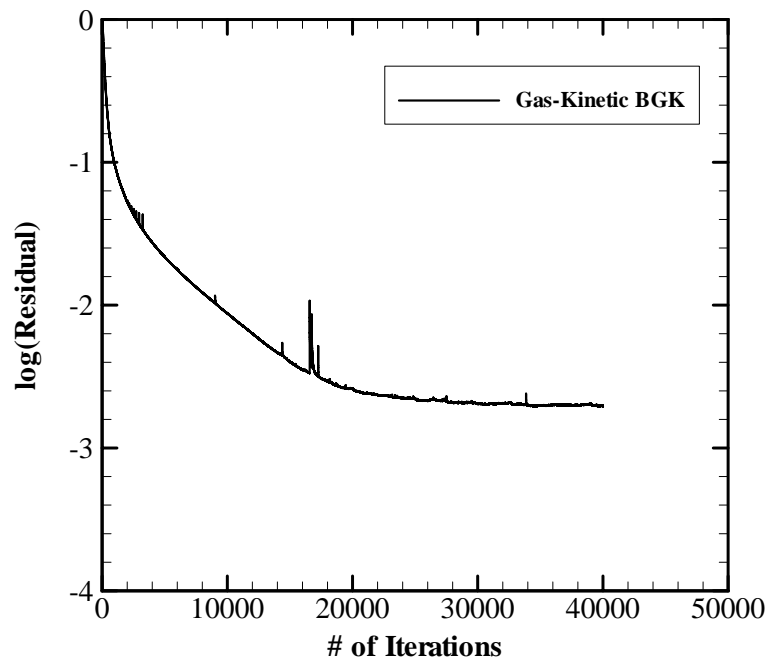


Figure 4.78: Convergence history for Case 4 (Medium mesh).

#### 4.3.5 Summary

The 3-D test cases considered in this section show that the Gas-Kinetic BGK scheme produces highly accurate results for both inviscid and viscous flows. In viscous flows, the use of hexahedron cells near the wall regions and tetrahedron cells at the farfield provides the required resolution of boundary layers while reducing the total number of grid cells. The present results for 3-D flows again show that the Gas-Kinetic BGK method can effectively be used for the simulation of practical aerodynamic problems.



## CHAPTER 5

### CONCLUDING REMARKS

Numerical methods for the analysis of fluid flow can be designed from two fundamental descriptions of the fluid motion: *continuum approach* and *gas-kinetic theory*. In the present study, gas-kinetic theory based methods for inviscid and viscous flow simulations on unstructured/hybrid grids are developed. At the beginning, the finite volume gas-kinetic methods in 1-D are investigated. Intensive theoretical and numerical discussions as well as comparisons with classical methods are made. The Gas-Kinetic BGK method is then extended for the solution of 2-D and 3-D inviscid and viscous flows on unstructured/hybrid grids. The computations are performed in parallel and various inviscid and viscous validation cases are considered. Based on the numerical solutions for both inviscid and viscous flows on unstructured/hybrid grids, the following conclusions can be drawn:

- The theoretical and numerical investigations reveal the basic properties of the Gas-Kinetic BGK method, which can be summarized as (1) a higher order gas evolution model, (2) the satisfaction of entropy and positivity conditions, and (3) multidimensional character. All these properties are not readily available in classical approximate Riemann solvers. Instead, the most popular one, the approximate Riemann solver of Roe, is a one dimensional model which needs an entropy fix and violates the positivity condition in certain flow problems. When compared to the gas-kinetic counterpart (i.e., Kinetic Flux Vector Splitting), the Gas-Kinetic BGK scheme has a more advanced and complex gas evolution model, which is based on particle collisions, and hence the numerical diffusion is controlled in the Gas-Kinetic BGK scheme, which is the main deficiency in the Kinetic Flux Vector Splitting scheme. The weakest point of the Gas-Kinetic BGK scheme is observed to be its computational cost due to the use of extensive exponential functions.
- In gas-kinetic methods, the equation of state can easily be replaced to accommodate various flow regimes as opposed to the approximate Riemann solver of Roe, which requires the reformulation of averaged Jacobian matrix.
- In the Gas-Kinetic BGK method, the convective (inviscid) and diffusive (viscous) fluxes are evaluated at once through the gas distribution function. It should be noted that inviscid and viscous fluxes are computed separately in classical methods.

- The preliminary studies in 1-D indicate that the results obtained from gas-kinetic theory based methods are comparable with those of classical methods. The gas-kinetic methods do not give any unphysical results. The Kinetic Flux Vector Splitting scheme show similar behavior as the classical flux vector splitting schemes. On the other hand, the Gas-Kinetic BGK scheme gives highly accurate results due to its underlying theory based on particle collisions.
- The 2-D flow cases considered show that the Gas-Kinetic BGK scheme produces very accurate results for both inviscid and viscous flows. The unphysical phenomena such as carbuncle, odd-even decoupling, etc. are not observed while it is found that the Roe scheme may need special treatments such as entropy fix in certain problems.
- It is observed that the numerical entropy generation in the Gas-Kinetic BGK scheme is significantly less than that of Roe scheme, which contributes to the accuracy of the Gas-Kinetic BGK method.
- The use of hybrid grids provides an efficient and high resolution of boundary layers in viscous flows while reducing the total number of grid cells.
- The parallel computations exhibit that the high parallel efficiency of the Gas-Kinetic BGK scheme is maintained as the number of processors increases. This is due to the high computing to communication ratio in the Gas-Kinetic BGK schemes. The parallel computations significantly improve the computation time of the Gas-Kinetic BGK scheme which, in

turn, enable the method for the computation of practical aerodynamic flow problems.

Considering the results obtained in the present study, the following suggestions about the Gas-Kinetic BGK method can be made as future work:

- In order to simulate the real flow physics, turbulence effects should be taken into account. The inclusion of turbulence effect to the Gas-Kinetic BGK method may be an challenging study. Another way is to incorporate one- or two-equation turbulent models with the Gas-Kinetic BGK scheme.
- The Gas-Kinetic BGK scheme is also quite suitable for the solution of hypersonic, chemically reacting flows including real gas effects.

## REFERENCES

- [1] Godunov, S. K., *A Difference Scheme For the Numerical Computation of Discontinuous Solutions of Hydrodynamic Equations*, Math. Sbornik 35, p. 271, 1959.
- [2] Roe, P. L., *Approximate Riemann Solvers, Parameter Vectors, and Difference Schemes*, J. Comp. Phys., Vol. 43, p. 357, 1981.
- [3] Osher, S., and Solomon, F., *Upwind Schemes For Hyperbolic Systems of Conservation Laws*, Math. Comp., Vol. 38, p. 339, 1981.
- [4] Harten, A., Lax, P. D., and Van Leer, B., *On Upstream Differencing and Godunov-Type Schemes For Hyperbolic Conservation Laws*, SIAM Rev., Vol. 25, p. 35, 1983.
- [5] Steger, J. L., and Warming, R. F., *Flux Vector Splitting of the Inviscid Gas Dynamics Equation With Applications to Finite Difference Methods*, J. Comp. Phys., Vol. 40, p. 263, 1981.
- [6] Van Leer, B., *Flux-Vector Splitting For the Euler Equations*, ICASE Report No. 82-20, 1982.

- [7] Liou, M. S., and Steffen, C. J., *A New Flux Splitting Scheme*, J. Comp. Phys., Vol. 107, p. 23, 1993.
- [8] Jameson, A., *Positive Schemes and Shock Modelling For Compressible Flow*, Int. J. Num. Met. in Fluids, Vol. 20, p. 743, 1995.
- [9] Tatsumi, S., Martinelli, L., and Jameson, A., *A New High Resolution Scheme For Compressible Viscous Flow With Shocks* AIAA Paper No. 95-0466, 1995.
- [10] Edwards, J. R., *A Low-Diffusion Flux-Splitting Scheme For Navier-Stokes Calculations*, Comp. Fluids, Vol. 26, p. 653, 1997.
- [11] Rossow, C.-C., *A Simple Flux Splitting Scheme For Compressible Flows*, Proc. 11th DGLR-Fach-Symposium, Berlin, Germany, Nov. 10-12, 1998.
- [12] Einfeldt, B., Munz, C. D., Roe, P. L., and Sjögren, B., *On Godunov-Type Methods Near Low Densities*, J. Comp. Phys., Vol. 92, p. 273, 1991.
- [13] Quirk, J. J., *A Contribution to the Great Riemann Solver Debate*, Int. J. Num. Met. in Fluids, Vol. 18, p. 555, 1994.
- [14] Gressier, J., and Moschetta, J.-M., *On the Pathological Behavior of Upwind Schemes*, AIAA Paper No. 98-0110, 1998.
- [15] Pandolfi, M., and D'Ambrosio, D., *Upwind Methods and Carbuncle Phenomenon*, In Computational Fluid Dynamics 98, Vol. 1, p. 126, 4th ECCOMAS, John Wiley & Sons, 1998.
- [16] Robinet, J.-C., Gressier, J., Casalis, G., and Moschetta, J.-M., *The Carbuncle Phenomenon: An Intrinsic Inviscid Instability?*, 22nd ISSW, 1999.

- [17] Gressier, J., and Moschetta, J.-M., *Robustness Versus Accuracy in Shock-Wave Computations*, Int. J. Num. Met. in Fluids, Vol. 33, p. 313, 2000.
- [18] Chen, S.Y., and Doolen, G.D., *Lattice Boltzmann Method For Fluid Flows*, Annu. Rev. Fluid Mech., Vol. 30, p. 329, 1998.
- [19] Succi, S., *The Lattice Boltzmann Equation For Fluid Dynamics and Beyond*, Clarendon Press, Oxford, 2001.
- [20] Wolf-Gladrow, D. A., *Lattice-Gas Cellular Automata and Lattice Boltzmann Models*, Springer-Verlag, Berlin, 2000.
- [21] Guo, Z., Shi, B., and Wang N., *Lattice BGK Model For Incompressible Navier-Stokes Equation*, J. Comp. Phys., Vol. 165, p. 288, 2000.
- [22] Filippova, O., Succi, S., Mazzocco, F., Arrighetti, C., Bella G., and Hanel D., *Multiscale Lattice Boltzmann Schemes With Turbulence Modeling*, J. Comp. Phys., Vol. 170, p. 812, 2001.
- [23] Luo, L.-S., *Theory of the Lattice Boltzmann Method: Lattice Boltzmann Models For Non-Ideal Gases*, Phys. Rev. E, Vol. 62-4, p. 4982, 2000.
- [24] Palmer, B., and Rector, D. R., *Lattice Boltzmann Algorithm For Simulating Thermal Flow in Compressible Fluids*, J. Comp. Phys., Vol. 161, p. 1, 2000.
- [25] Mason, R. J., *A Multi-Speed Compressible Lattice Boltzmann Model*, J. Stat. Phys., Vol. 107, p. 385, 2002.
- [26] Sun, C., *Adaptive Lattice Boltzmann Model For Compressible Flows: Viscous and Conductive Properties*, Phys. Rev. E, Vol. 61-3, p. 2645, 2000.

- [27] Succi, S., *Lattice Boltzmann Equation: Failure or Success*, Phys. A, Vol. 240, p. 221, 1997.
- [28] Sanders, R. H., and Prendergast, K. H., *The Possible Relation of the Three-Kiloparsec Arm to Explosions in the Galactic Nucleus*, Astro. J., Vol. 188, 1974.
- [29] Reitz, R. D., *One-Dimensional Compressible Gas Dynamics Calculations Using the Boltzmann Equation*, J. Comp. Phys., Vol. 42, p. 108, 1981.
- [30] Pullin, D. I., *Direct Simulation Methods For Compressible Inviscid Ideal Gas Flow*, J. Comp. Phys., Vol. 34, p. 231, 1980.
- [31] Mandal, J. C., and Deshpande, S. M., *Kinetic Flux Vector Splitting For the Euler Equations*, Comp. Fluids, Vol. 23-2, p. 447, 1994.
- [32] Perthame, B., *Second-Order Boltzmann Schemes For Compressible Euler Equations in One and Two Space Dimensions*, SIAM J. Num. Analy., Vol. 29, p. 1, 1992.
- [33] Prendergast, K. H., and Xu, K., *Numerical Hydrodynamics From Gas-Kinetic Theory*, J. Comp. Phys., Vol. 109, p. 53, 1993.
- [34] Bhatnagar, P. L., Gross, E. P., and Krook, M., *A Model For Collision Processes in Gases I. Small Amplitude Processes in Charged and Neutral One-Component Systems*, Phys. Rev., Vol. 94-3, p. 511, 1954.
- [35] Xu, K., Martinelli, L., and Jameson, A., *Gas-Kinetic Finite Volume Methods, Flux Vector Splitting and Artificial Diffusion* J. Comp. Phys., Vol. 120, p. 48, 1995.



- [36] Xu, K., and Jameson, A., *Gas-Kinetic Relaxation (BGK-Type) Schemes For the Compressible Euler Equations*, AIAA Paper No. 95-1736, 1995.
- [37] Xu, K., Kim, C., Martinelli, L., and Jameson, A., *BGK-Based Schemes For the Simulation of Compressible Flow*, Int. J. CFD., Vol. 7, p. 213, 1996.
- [38] Xu, K., and Hu, J., *Projection Dynamics in Godunov-Type Schemes*, J. Comp. Phys., Vol. 142, p. 412, 1998.
- [39] Xu, K., *BGK-Based Scheme For Multicomponent Flow Calculations*, J. Comp. Phys., Vol. 134, p. 122, 1997.
- [40] Xu, K., *A Gas-Kinetic BGK Scheme For the Navier-Stokes Equations and Its Connection With Artificial Dissipation and Godunov Method*, J. Comp. Phys., Vol. 171, p. 289, 2001.
- [41] Xu, K., *A Gas-Kinetic Scheme For the Euler Equations With Heat Transfer*, SIAM J. Sci. Comp., Vol. 20-4, p. 1317, 1997.
- [42] Tang, H.-Z., and Xu, K., *A High-Order Gas-Kinetic Method For Multidimensional Ideal Magnetohydrodynamics*, J. Comp. Phys., Vol. 165, p. 69, 2000.
- [43] Lian, Y.-S., and Xu, K., *A Gas-Kinetic Scheme For Reactive Flows*, ICASE Report No. 98-55, 1998.
- [44] Lian, Y.-S., and Xu, K., *A Gas-Kinetic Scheme For Multimaterial Flows and Its Application in Chemical Reactions*, J. Comp. Phys., Vol. 163, p. 349, 2000.
- [45] Xu, K., *A Kinetic Method For Hyperbolic-Elliptic Equations and Its Application in Two-Phase Flow*, J. Comp. Phys., Vol. 166, p. 383, 2001.

- [46] Kim, C., Xu, K., Martinelli, L., and Jameson, A., *Analysis and Implementation of the Gas-Kinetic BGK Scheme For Computational Gas Dynamics*, Int. J. Num. Met. in Fluids, Vol. 25, p. 21, 1997.
- [47] Vincenti, W. G., and Kruger Jr., C. H., *Introduction to Physical Gas Dynamics*, John Wiley & Sons, New York, 1967.
- [48] Cercignani, C., *The Boltzmann Equation and Its Applications*, Springer-Verlag, New York, 1988.
- [49] Kogan, M. N., *Rarefied Gas Dynamics*, Plenum Press, New York, 1969.
- [50] Chapman, S., and Cowling, T. G., *The Mathematical Theory of Non-Uniform Gases*, The Cambridge University Press, London, 1953.
- [51] Abgrall, R., and Karni, S., *Computations of Compressible Multifluids*, J. Comp. Phys., Vol. 169, p. 594, 2001.
- [52] Van Leer, B., *Toward the Ultimate Conservative Difference Scheme V. A Second-Order Sequel to Godunov's Method*, J. Comp. Phys., Vol. 32, p. 101, 1979.
- [53] Xu, K., *Gas-Kinetic Schemes For Unsteady Compressible Flow Simulations*, VKI Lecture Series 98-03, 1998.
- [54] Xu, G. H., *Hydrodynamic and N body Schemes on an Unstructured Adaptive Mesh With Application to Cosmological Simulations*, Monthly Notices of Royal Astronomical Society, Vol. 288, p. 903, 1997.
- [55] Tang, T., and Xu, K., *Gas Kinetic Schemes For the Compressible Euler Equations I: Positivity Preserving Analysis*, Preprint, 1997.

- [56] Harten, A., Engquist, B., and Chakravarthy, S., *Uniformly Higher-Order Accurate Essentially Non-Oscillatory Schemes III*, J. Comp. Phys., Vol. 71, p. 231, 1987.
- [57] Jameson, A., Schmidt, W., and Turkel, E., *Numerical Solutions of the Euler Equations by Finite Volume Methods Using Runge-Kutta Time-Stepping Schemes*, AIAA Paper No. 81-1259, 1981.
- [58] Jameson, A., and Baker, T. J., *Solution of Euler Equations For Complex Configurations*, AIAA Paper No. 83-1929, 1983.
- [59] Anderson, W. K., Thomas, J. L., and Whitfield, D. L., *Three-Dimensional Multigrid Algorithms For the Flux-Split Euler Equations*, NASA TP 2829, 1988.
- [60] Sod, G. A., *A Survey of Several Finite Difference Methods For Systems of Non-Linear Hyperbolic Conservation Laws*, J. Comp. Phys., Vol. 27, p. 1, 1978.
- [61] Arora, M., and Roe, P. L., *On Postshock Oscillations Due to Shock Capturing Schemes in Unsteady Flows*, J. Comp. Phys., Vol. 130, p. 25, 1997.
- [62] Woodward, P. R., and Colella, P., *The Numerical Simulation of Two-Dimensional Fluid Flow With Strong Shocks*, J. Comp. Phys., Vol. 54, p. 115, 1984.
- [63] Cook, P. H., McDonald, M. A., and Firmin, M. C. P., *Aerofoil RAE2822 - Pressure Distributions, and Boundary Layer and Wake Measurements*, AGARD AR 138, 1979.

- [64] Chit, O. J., Omar, A. A., Asrar, W., and Hamdan, M. M., *Implicit Gas-Kinetic Bhatnagar-Gross-Krook Scheme For Compressible Flows*, AIAA J., Vol. 42-7, p. 1293, 2004.
- [65] INRIA, Gamm Workshop, December 46, 1985, Nice, France, *Numerical Simulation of Compressible Navier Stokes Equations-External 2D Flows Around a NACA0012 Airfoil*, Centre de Rocqufort, de Rennes et de Sophia-Antipolis, 1986.
- [66] May, G., Srinivasan, B., and Jameson, A., *An Improved Gas-Kinetic BGK Finite-Volume Method For Three-Dimensional Transonic Flow*, J. Comp. Phys., Vol. 220, p. 856, 2007.
- [67] Graves, E. B., *Stability and Control Characteristics at Mach Numbers From 0.20 to 4.63 of a Cruciform Air-to-Air Missile With Triangular Canard Controls and a Trapezoidal Wing*, NASA TM X-3070, 1974.
- [68] Schmitt, V., and Charpin, F., *Pressure Distributions on the ONERA-M6-Wing at Transonic Mach Numbers*, AGARD AR 138, 1979.
- [69] Monta W. J., *Supersonic Aerodynamic Characteristics of a Sparrow III Type Missile Model With Wing Controls and Comparison With Existing Tail-Control Results*, NASA TP 1078, 1977.

## APPENDIX A

# MOMENTS OF THE GAS DISTRIBUTION FUNCTION

The Kinetic Flux Vector Splitting and Gas-Kinetic BGK schemes contain bounded or unbounded integrals which are the moments of the Maxwellian distribution function in half or full space. In the following, the recursive relations to calculate these integrals are given.

For a 1-D Maxwellian distribution function

$$g = \rho \left(\frac{\lambda}{\pi}\right)^{\frac{K+1}{2}} \exp \{-\lambda [(u - U)^2 + \xi^2]\},$$

by introducing the notation for the integral of moments of  $g$

$$\langle \dots \rangle = \frac{1}{\rho} \int_{-\infty}^{+\infty} \int_{-\infty}^{+\infty} (\dots) g \, du \, d\xi$$

the general formula is

$$\langle u^n \xi^m \rangle = \langle u^n \rangle \langle \xi^m \rangle$$

where  $n$  is an integer,  $m$  is an even integer. The values of  $\langle \xi^m \rangle$  are

$$\langle \xi^2 \rangle = \frac{K}{2\lambda},$$

$$\langle \xi^4 \rangle = \frac{3K + K(K-1)}{4\lambda^2}.$$

The values of  $\langle u^n \rangle$  depend on the integration limits. In full space, the recursive relations are

$$\langle u^0 \rangle = 1$$

$$\langle u^1 \rangle = U$$

$$\vdots$$

$$\langle u^n \rangle = U \langle u^{n-1} \rangle + \frac{n-1}{2\lambda} \langle u^{n-2} \rangle$$

whereas in half space, with the notations,

$$\langle \dots \rangle_{u>0} = \frac{1}{\rho} \int_{-\infty}^{+\infty} \int_0^{+\infty} (\dots) g \, du \, d\xi$$

$$\langle \dots \rangle_{u<0} = \frac{1}{\rho} \int_{-\infty}^{+\infty} \int_{-\infty}^0 (\dots) g \, du \, d\xi$$

the recursive relations involve complementary error function:

$$\langle u^0 \rangle_{u>0} = \frac{1}{2} \operatorname{erfc}(-\sqrt{\lambda}U)$$

$$\langle u^1 \rangle_{u>0} = U \langle u^0 \rangle_{u>0} + \frac{1}{2} \frac{\exp(-\lambda U^2)}{\sqrt{\pi\lambda}}$$

$$\vdots$$

$$\langle u^n \rangle_{u>0} = U \langle u^{n-1} \rangle_{u>0} + \frac{n-1}{2\lambda} \langle u^{n-2} \rangle_{u>0}$$

and

$$\langle u^0 \rangle_{u<0} = \frac{1}{2} \operatorname{erfc}(\sqrt{\lambda}U)$$

$$\begin{aligned}
\langle u^1 \rangle_{u<0} &= U \langle u^0 \rangle_{u<0} - \frac{1}{2} \frac{\exp(-\lambda U^2)}{\sqrt{\pi \lambda}} \\
&\vdots \\
\langle u^n \rangle_{u<0} &= U \langle u^{n-1} \rangle_{u<0} + \frac{n-1}{2\lambda} \langle u^{n-2} \rangle_{u<0}
\end{aligned}$$

In 2-D and 3-D, the Maxwellian distribution function can be decomposed into the form of the 1-D and the above integration formula can be used. For example, in 2-D,

$$\langle \dots \rangle = \frac{1}{\rho} \int_{-\infty}^{+\infty} \int_{-\infty}^{+\infty} \int_{-\infty}^{+\infty} (\dots) g \, du \, dv \, d\xi$$

and

$$\langle u^n v^m \xi^p \rangle = \langle u^n \rangle \langle v^m \rangle \langle \xi^p \rangle .$$

On the other hand, in 3-D,

$$\langle \dots \rangle = \frac{1}{\rho} \int_{-\infty}^{+\infty} \int_{-\infty}^{+\infty} \int_{-\infty}^{+\infty} \int_{-\infty}^{+\infty} (\dots) g \, du \, dv \, dw \, d\xi$$

and

$$\langle u^n v^m w^p \xi^q \rangle = \langle u^n \rangle \langle v^m \rangle \langle w^p \rangle \langle \xi^q \rangle .$$

Similarly, the recursive relations for  $\langle v^m \rangle$  and  $\langle w^p \rangle$  can be obtained by replacing  $U$ 's with  $V$ 's and  $W$ 's, respectively, in the above formulas.

# VITA

## PERSONAL INFORMATION

**Name, Surname :** Murat ILGAZ

**Nationality :** Turkish

**Date & Place of Birth :** February 28, 1975, Kayseri

**Marital Status :** Married

**E-mail :** murat.ilgaz@sage.tubitak.gov.tr

## EDUCATION

<b>Degree</b>	<b>Institution</b>	<b>Year of Graduation</b>
M.Sc.	METU Aeronautical Engineering	2002
B.Sc.	METU Aeronautical Engineering	1999
High School	Kayseri Science High School	1993

## WORK EXPERIENCE

<b>Year</b>	<b>Place</b>	<b>Enrollment</b>
2003-Present	TÜBİTAK-SAGE	Senior Research Engineer
2002-2003	TÜBİTAK-SAGE	Research Engineer
1999-2002	METU Aeronautical Engineering	Research Assistant



## SELECTED PUBLICATIONS

- Ilgaz M., Tuncer İ. H., *A Parallel Gas-Kinetic BGK Scheme for 3-D Viscous Flows on Hybrid Grids* (in preparation, to be submitted to Journal of Computational Physics).
- Ilgaz M., Tuncer İ. H., *A Parallel Gas-Kinetic BGK Method for 3-D Inviscid Flows on Unstructured Grids* (in preparation, to be submitted to AIAA Journal).
- Ilgaz M., Tuncer İ. H., *Parallel Implementation of Gas-Kinetic BGK Method for 2-D Laminar Flows on Unstructured Hybrid Grids* (submitted to AIAA Journal).
- Ilgaz M., Tuncer İ. H., *A Gas-Kinetic BGK Scheme for Parallel Solution of 3-D Viscous Flows on Unstructured Hybrid Grids*, 18th AIAA Computational Fluid Dynamics Conference, 25-28 June 2007, Miami (accepted).
- Ilgaz M., Tuncer İ. H., *Gaz-Kinetik BGK Metodu ile 3-Boyutlu Akışların Düzensiz Çözüm Ağları Üzerinde Paralel Olarak Hesaplanması*, 1. Ulusal Havacılık ve Uzay Konferansı, 21-23 Eylül 2006, Ankara, Türkiye.
- Ilgaz M., Tuncer İ. H., *Parallel Implementation of Gas-Kinetic BGK Scheme on Unstructured Hybrid Grids*, 36th AIAA Fluid Dynamics Conference and Exhibit, 5-8 June 2006, San Francisco.
- Ilgaz M., Tuncer İ. H., *On Gas-Kinetic Schemes for 1-D Multi-Species Flows*, 3rd Ankara International Aerospace Conference, 22-25 August 2005, Ankara,

Turkey.

- Ilgaz M., Tuncer İ. H., *Parallel Implementation of Gas-Kinetic Schemes on 2-D Unstructured Grids*, 3rd Ankara International Aerospace Conference, 22-25 August 2005, Ankara, Turkey.
- Ilgaz M., Ak M. A., Tuncer İ. H., *Sayısal Akışkanlar Mekaniğinde Yeni Bir Yaklaşım: Gaz-Kinetik Metotlar*, 5. Kayseri Havacılık Sempozyumu, 13-14 Mayıs 2004, Kayseri, Türkiye.